

# Geomorphic Character and Dynamics of the Rees-Dart Fluvial Systems

---



MAY 2025

Prepared for the Otago Regional Council



**James Brasington**  
**WATERWAYS CENTRE | UNIVERSITY OF CANTERBURY**

## REVISION HISTORY

AUTHOR:	Professor James Brasington, Director, Waterways Centre
SIGNATURE:	
DATE:	03 May 2025
REVISION:	01
AUTHORISED BY:	Tim Van Woerden, Senior Natural Hazards Analyst
SIGNATURE:	
ORGANIZATION:	Otago Regional Council
DATE:	08 May 2025

# CONTENTS

	PAGE
<b>EXECUTIVE SUMMARY</b>	<b>8</b>
<b>0. SCOPE</b>	<b>9</b>
<b>1. CATCHMENT CONTEXT</b>	<b>10</b>
1.1 REGIONAL SETTING	10
1.2 THE DART RIVER	12
1.2.1 HYDROLOGY	12
1.2.2 RIVER CORRIDOR	13
1.3 THE REES RIVER	16
1.3.1 HYDROLOGY	16
1.3.2 RIVER CORRIDOR	17
1.4 THE DELTA AND LAKE WAKATIPU	21
1.4.1 SEDIMENTATION AND DELTA PROGRADATION	22
<b>2. CHANNEL MORPHOLOGY AND DYNAMICS</b>	<b>25</b>
2.1 GEOMORPHIC STRUCTURE OF THE LOWER REES-DART BRAIDPLAIN	25
2.2 BED-LEVEL ADJUSTMENT ON THE REES RIVER	27
2.2.1 RELIABILITY OF CROSS-SECTION SURVEYS	27
2.3 DEM DIFFERENCING	28
2.3.1 MANAGING DEM UNCERTAINTY	28
2.4 SURVEY DATA AND UNCERTAINTY MODELLING	30
2.4.1 DEM REGISTRATION AND QUANTIFYING UNCERTAINTY	32
2.5 CHANNEL ADJUSTMENT ON THE REES RIVER 2011–2022	36
2.5.1 REACH-AVERAGE CHANNEL CHANGE	38
2.5.2 LONGITUDINAL CHANNEL CHANGE	41
2.5.3 A CONCEPTUAL MODEL OF MORPHODYNAMIC ADJUSTMENT	52
<b>3. EVOLUTION OF THE DART RIVER CORRIDOR</b>	<b>55</b>
3.1 ARCHIVAL REMOTE SENSING	55
3.2 AUTOMATED MAPPING OF RIVER CORRIDOR COVER WITH GEE	56
3.3 STRUCTURE AND EVOLUTION OF THE DART RIVER CORRIDOR	60
3.4 DEEPENING THE HISTORICAL PERSPECTIVE	68
3.5 THE SLIP STREAM LANDSLIDE	70
3.5.1 FORMATION AND DRAINAGE OF THE RIVERINE LAKE	71
3.5.2 LANDSLIDE VOLUME AND FLUVIAL SEDIMENT SUPPLY	72
<b>4. FLUVIAL PROCESSES AND HAZARDS</b>	<b>78</b>
4.1 GUIDING GEOMORPHIC PRINCIPLES	78
4.2 FLUVIAL HAZARDS	79
4.2.1 LOSS OF CHANNEL CAPACITY	80
4.2.2 LATERAL CHANNEL MIGRATION & INFRASTRUCTURE EXPOSURE	81
4.2.3 CHANNEL AVULSION AND BREAKOUT FLOODING	82
<b>5. CONCLUSIONS</b>	<b>83</b>
<b>6. REFERENCES</b>	<b>84</b>

## List of Figures

<b>FIGURE 1.</b>	The Dart and Rees River catchments. Both rivers drain south, forming an extensive, 2.5 km wide delta with Lake Wakatipu. The townships of Glenorchy and Kinloch lie on the eastern and western shores of the delta respectively.	11
<b>FIGURE 2.</b>	Seasonal variation in mean flow for the Dart River at the Hillocks, 1997-2000. Whiskers show upper and lower quartiles. Data sourced from Otago Regional Council.	12
<b>FIGURE 3.</b>	The Dart River corridor along its 61 km run to Lake Wakatipu. The long profile extracted from the mean valley floor elevation is shown on the inset, with gradients falling from between 2-5% headwaters to 0.3% in the delta.	15
<b>FIGURE 4.</b>	The Rees River corridor along its 41 km run to Lake Wakatipu. The long profile extracted from the mean valley floor elevation is shown on the inset, with gradients falling from between 0.05-0.1 in the headwaters to 0.003 in the delta.	18
<b>FIGURE 5.</b>	Oblique aerial image revealing historic distributary patterns in the Lower Rees River. A) Photo #5113 Tooth Peaks and Glenorchy, Lake Wakatipu from the Muir and Moodie (Burton Brothers), c. 1900; B) Whites Aviation Ltd: Photograph Ref: WA-08842-F. Alexander Turnbull Library, Wellington, New Zealand, 1947.	20
<b>FIGURE 6.</b>	Box-and-whisker plots showing longitudinal trends in surface grain-size. Median, D50, is represented by the dot, while the whiskers extend to D16 and D84 respectively. Samples were taken from randomly selected locations on bar heads. At each site, 100 clasts were sampled using a 1 m <sup>2</sup> frame.	21
<b>FIGURE 7.</b>	Stratigraphic logs interpreted from Lalor and Purvis (1970) and reproduced by Williams (2014). Approximate locations for the four holes are: Hole 1 (1,239,820E 5,036,330N); Hole 2 (1,238,515E 5,034,830N); Hole 3 (1,236,630E 5,031,075N); Hole 4 (1,235,400E 5,024,680N);	23
<b>FIGURE 8.</b>	Depth of sediment accumulated on the Rees-Dart delta over the period 1966-2007, after Wild (2013).	24
<b>FIGURE 9.</b>	Relative Elevation Model (REM) of the lower 10 km of the Rees-Dart Rivers. Cross-sections XS1 and XS2 reveal the elevation profile of the wider valley floor below Mt Alfred, highlighting the currently superelevated active channel of the Rees River and the marginal topographic depressions (note the different horizontal scales).	26
<b>FIGURE 10.</b>	Timeseries of 1 m DEMs. The 2011 survey covers only the lower 3-4 km of the delta, while 2019 and 2022 extend over the wider valley floor. The 2021 survey is limited to the active corridor of the Rees.	31
<b>FIGURE 11.</b>	Distribution of reference areas used for the co-registration assessment. A total of 26 sites were manually identified using aerial imagery and hillshade models to assess their stability. These are distributed across a range of land cover types, including hard points on roads and across a range of more vegetated land covers of varying density (pasture < scrub < trees). The extent of each survey is shown by the bounding polygons revealing the range of sites available to assess the registration quality between years.	33
<b>FIGURE 12.</b>	Elevation differences in stable reference areas aggregated by pairwise year comparisons and by land cover classes. The box and whisker plots show the median (central bar) and interquartile range (box) while the grand mean and pooled standard deviations are presented as labels. All differences in metres.	34



<b>FIGURE 13.</b> An illustrative DEM of Difference thresholded at the 84% CI for the Rees River (between river kms 3.75 and 8.25) for the period 2019 - 2022.	37
<b>FIGURE 14.</b> Hourly maximum river discharge on the Dart River at the Hillocks between October 2011 and November 2022. The DEM difference change epochs over this period are visualized by the coloured bars above the flow series.	39
<b>FIGURE 15.</b> AOI and the 500 m scheme of discrete cells used to summarize longitudinal channel changes on the Rees River. Distances plotted represent the cell centroid, measured from the delta front. The extent of the 2011, 2019, 2021 and 2022 surveys is shown for reference.	41
<b>FIGURE 16.</b> Longitudinal patterns of volumetric channel change segmented using the 500 m scheme of cells. All changes and associated error bars are based on a level of detection defined by the 84% CI. Key zones of sediment storage during the flood-dominated 2019-2021 epoch are highlighted, which together represent >80% net storage.	43
<b>FIGURE 17.</b> Longitudinal patterns of mean bed level change based on the continuous array of 500 m cells. The grey envelope represents the uncertainty associated with thresholding at the 84% confidence interval.	44
<b>FIGURE 18.</b> Longitudinal maps of the pattern of mean bed level change as defined by the 500 m streamwise cells. Positive (aggradation) is mapped in shades of blue, while negative changes (degradation) are coded in shades of red. All changes are thresholded at the 84% CI. The labels represent the estimated change bed level (m) for each cell.	45
<b>FIGURE 19.</b> 500 m sections extracted from the 2011 and 2019 DEMs in the lower 4 km of the Rees reveal the longitudinal pattern of aggradation (see also Figure 18). The inset map shows the location of sections. The limited freeboard on the true left at river 1.5, 2.5 and 4 kms is highlighted and these represent important potential breach points and appear to link to pre-existing floodplain drainage as shown on the inset aerial image.	46
<b>FIGURE 20.</b> Morphological adjustment at the narrows between river km 13-13.5. The DEMs in 2019 and 2021 reveal lateral expansion of the upstream central bar that drives widening of the active section on the true right, while choking the true left anabranch. The intensity of the downstream confluence is reduced and the true right bar complex grows and the main thalweg aggrades. The DoD shows the cumulative impact of these changes.	48
<b>FIGURE 21.</b> DEM of Difference for 2019 – 2021 for river km 8-10, revealing gravel extraction areas and high rates of sedimentation on the true right of the river and close to the Glenorchy-Paradise Bridge. All changes computed using an 84% CI threshold.	49
<b>FIGURE 22.</b> DEM of Difference 2019-2022 for river km 3 – 6. Volumes of deposition through this reach remain high but the volume of erosion falls systematically downstream. The net consequence is an increase in mean bed throughout but, in particular, at the downstream end of the reach where the bed level rises by 0.22 m.	51
<b>FIGURE 23.</b> Integrated trend in mean bed level for the period 2011-2022 limited to the area where surveys intersect.	53
<b>FIGURE 24.</b> A conceptual model of the relationship between sediment supply, sediment transport conditions and bed adjustment. Sediment supply from upstream catchment is unlimited, so that during high flow events large volumes of material	52

are delivered to the piedmont braidplain. The hydraulic conditions are incompetent to transport this high load and the river aggrades. In between floods, lower sediment supply from upstream enables the river to rework material the deposited and the river degrades. The long-term tendency of bed level is ultimately controlled by the interarrival time between large events.

<b>FIGURE 25.</b> Schematic illustration of the workflow for probabilistic mapping of river corridor land cover. Analysis Ready Data from GEE are filtered and sorted and classified using a multi-index approach. Image stacks for multiple time windows are then analyzed statistically, and the probability of pixel membership of land cover classes determined.	59
<b>FIGURE 26.</b> Number and temporal distribution of images covering the Dart River catchment accessed through Google Earth Engine. This list only includes images with less than 10% cloud cover and no significant image artefact flags.	60
<b>FIGURE 27.</b> Probability maps revealing the distribution of ‘water’ pixels from 1995-2024. The small inset images show probabilities based on 5-year timeslices, while the large image shows the likelihood mapped for the full 29 year period. This pattern captures the inherent dynamism of the active anabranches of the period, giving rise the blurred patterns evident in the 29 year composite, particularly within the lower 10 km of the Dart River.	61
<b>FIGURE 28.</b> Probability maps revealing the distribution of pixels belonging the active channel or alluvial class – comprising the wet channels and exposed sediment. Again, the small inset figures show 5 year timeslices, while the large map captures the distribution of the full 29 year record. Areas of the valley floor that are consistently active (wet or exposed sediment) appear as red, while stable areas appear green. Active margins of the braidplain are characterized the low porobability yellow areas.	62
<b>FIGURE 29.</b> Probability map for the water class for the lower Dart and Rees Rivers. Probabilities are scaled in 0.1 intervals. Dart blues reveal stable areas of the anabranh network.	63
<b>FIGURE 30.</b> Probability map for the alluvial or active channel class for the lower Dart and Rees Rivers. Probabilities are scaled in 0.1 intervals. Stable areas of the valley appear in green, while the core active channel is red. Areas associated with migration of the active channel over the last 30 years is shown in shades of yellow.	64
<b>FIGURE 31.</b> Westward migration of the Dart River corridor from 2005-2025 mapped in 5-year intervals. Areas of erosion on the right bank are shown in shades of red and are matched by recovery and stabilization of the channel bed, shown in shades of blue on the true left. Areas of change are computed for the 500 m cells shown (labels are chainage from the delta) and plotted as average linear changes in Figure 32.	66
<b>FIGURE 32.</b> Average longitudinal rates of bank erosion and channel recovery calculated for 5-year intervals. Data are integrated over 500 m intervals. Highest rates of bank erosion occur between 4 -7 km upstream and are widely above 200 m over this 20 year period. Total rates of recovery slightly outpace erosion, suggesting a marginal decrease in the active width over the full period.	67
<b>FIGURE 33.</b> Long-term pattern of planform adjustment on the lower Dart River, compiled from the analysis of Landsat scenes from 1973 to 2019. The data reveal a widespread pattern of widening between 1973 – 1990, followed by progressive contraction of the river, most marked in the lower 10 km.	69
<b>FIGURE 34.</b> Soundings and interpolated bathymetry of the lake formed by impoundment of the Dart River.	72

<b>FIGURE 35.</b> Elevation change model derived from 2012 and 2015 WorldView DSMs, bracketing the 2014 landslide at Slip Stream. This a large transfer of mass at the top of the landslide (20 m of vertical deformation) to a deep gully above the fan, where flows have scoured to a depth of over 70 m, further destabilising the flanks of the gully. Deposition is focused on the upstream (northern) half of the fan, where sedimentation depths may exceed 15 m.	74
<b>FIGURE 36.</b> Volumetric budget for components of the landslide, derived from DEM differencing between the 2012 and 2015 elevation models.	75
<b>FIGURE 37.</b> Extensive turbidity plume in Lake Wakatipu during mid-January 2014, approximately two-weeks after the peak of activity at Slip Stream.	76
<b>FIGURE 38.</b> Geomorphologically driven river hazard pathways at the top of Lake Wakatipu.	79
<b>FIGURE 39.</b> Comparison of DEM difference models from between 2019-2022 and the earliest comprehensive regional orthophotography from 1966 reveals significant laterally mobility on both the lower Dart and Rees Rivers.	81

## List of Tables

<b>TABLE 1.</b> Estimated peak flow on the Dart River for annual recurrence intervals ranging between 5-500 years, after Mohssen (2021).	13
<b>TABLE 2.</b> Estimated peak flow on the Rees River for ARI ranging between 20-100 years, after Mohssen (2021).	17
<b>TABLE 3.</b> Lake Wakatipu levels for a range of ARIs between 5 and 200 years, after Mohssen (2021).	22
<b>TABLE 4.</b> Acquisition specifications and quality metrics for the Rees/Dart Lidar surveys.	30
<b>TABLE 5.</b> Areal, volumetric and average vertical changes for the lower Rees River computed for DEM differences 2011-2019; 2019-2021; and 2021-2022, integrated over the active channel. Changes are shown both before (raw) and after thresholding at the 84% confidence interval. This analysis assumes a spatially uniform DEM uncertainty of 0.06 m for all surface models.	38
<b>TABLE 6.</b> Rates of volumetric and vertical average change for each of the change epochs, calculated per day.	40
<b>TABLE 7.</b> Archival Landsat scenes used to compile a historical analysis of channel planform dynamics from 1973 – 2019. MSS = Multispectral Scanner System; TM = Thematic Mapper; ETM+ = Enhanced Thematic Mapper+; OLI = Operational Land Imager.	68

## EXECUTIVE SUMMARY

This report presents a detailed investigation into the geomorphic dynamics of the Rees and Dart Rivers, focusing on the physical processes that underpin flood and erosion hazards at the head of Lake Wakatipu. Using high-resolution topographic differencing, historical aerial and satellite imagery, and geomorphic analysis, the study documents how sediment supply, transport capacity, and channel form interact to shape the behaviour of these dynamic braided river systems.

The analysis rests on three interrelated findings:

1. **Catchment sediment supply is high** due to the combined effects of active tectonics, glacial oversteepening, and weak lithologies, which together create a landscape prone to landsliding. Sediment sources in this unstable terrain are well-connected to the fluvial system, particularly during severe storms.
2. **During large floods, sediment inputs regularly exceed the river's transport capacity**, leading to widespread deposition, especially in the lower reaches.
3. **Persistent aggradation drives high rates of lateral migration** and contributes to long-term **channel instability**.

The report quantifies recent aggradation in the Rees River, with mean bed level increases exceeding +0.2 m over the past decade. In the Dart, over 600 m of lateral channel migration has occurred since the 1970s. These findings reveal a geomorphic system that is highly sensitive to episodic disturbance, with complex, time-dependent responses to sediment inputs, boundary constraints, and hydrological variability.

From this analysis, three key hazard pathways are identified:

- **Loss of channel capacity**, leading to higher flood stages and reduced infrastructure performance.
- **Lateral channel migration**, posing ongoing risk to roads and flood protection structures.
- **Channel avulsion**, where super-elevated channels abruptly shift, redirecting floodwaters and bypassing defences.

These hazards are not anomalies but expected outcomes of the prevailing geomorphic setting. Effective long-term management must therefore be grounded in an understanding of the river as a dynamic, sediment-rich system. This report provides the baseline evidence and conceptual framework to support future risk assessment and adaptive management strategies.

## 0. SCOPE

The Waterways Centre was contracted by the Otago Regional Council to undertake research that aims to deepen understanding of the geomorphological processes that control the structure, form and dynamics of the Rees-Dart River corridors. This programme of research examines fluvial processes at multiple time and space scales and integrates three themes:

- Braiding processes and sediment transport
- River corridor evolution and channel migration
- Fluvial hazards

The first theme centres on the analysis of multiple airborne lidar datasets acquired since 2011 and aims to quantify channel morphology and its pattern of change over the past decade. Digital Elevation Model differencing methods (Brasington et al. 2003; Vericat et al., 2017) are used to derive changes in bed level and reveal longitudinal patterns of sediment storage and transfer. This analysis focuses on the morphological adjustment of the Rees River for which four repeat lidar surveys are available.

The second theme focuses on the analysis of archival satellite imagery to shed light on the longer-term, larger scale patterns of channel changes along the active valley floor over the last 50 years. This approach provides insights into channel belt migration and variations in active width over decadal timescales. The analysis focuses on the river corridor dynamics of the Dart River, the large spatial scale of which, makes this a suitable candidate to interrogate using the lower resolution perspective of optical satellite imagery.

Finally, the review concludes with an examination of the hazards associated with fluvial processes and the threats they pose a threat to the local communities.

# 1. CATCHMENT CONTEXT

## 1.1 REGIONAL SETTING

The catchments of the Dart and Rees Rivers extend over a combined area of over 1050 km<sup>2</sup>, lying between the Humbolt Mountains to the west, the Richardson Mountains to the east, with the Dart watershed extending north to the Barrier Range of the Main Divide (Figure 1). The internal watershed between the two catchments affords the Rees a sheltered position to the south of the Main Divide. Elevations along their combined watershed frequently attain altitudes of over 2000 m, while the divide between the Rees and Dart is framed by the 2,830 m summit of Mt Earnslaw.

The headwaters of both catchments lie in the steep, tectonically active Southern Alps, a 2000-3000 m range that intercepts the dominant westerly atmospheric circulation. This region is underlain by the Mesozoic Haast Schist basement. Locally this unit is characterized by a metamorphic gradient, with the lower grade schists of the Caples Terrain in the west, to the high-grade, well foliated schists of the Forbes and Rakaia Terranes in the north and east (Turnbull, 2000). The intense seismicity, high precipitation and erodible lithologies combine to create high regional rates of erosion.

While the upper Dart hosts the remnants of the Wakatipu Glacier, landsliding is now the dominant form of erosion (McColl and Davies, 2011). Quaternary glaciations have, however, shaped the landscape of the region, leaving a legacy over-widened valleys punctuated by local pinch-points associated with bedrock outcrops, moraine and landslide deposits and of course, the moraine-dammed Lake Wakatipu. The presence of multiple palaeo-shorelines and raised deltas, the highest of which (at 360 m) is >50 m above the current level of Lake Wakatipu (c. 309 m) suggests that the lake once extended upstream as far as the Hillocks and Camp Hill, perhaps as recently as 10-12 ka (Cook et al., 2014; Sutherland et al., 2019).

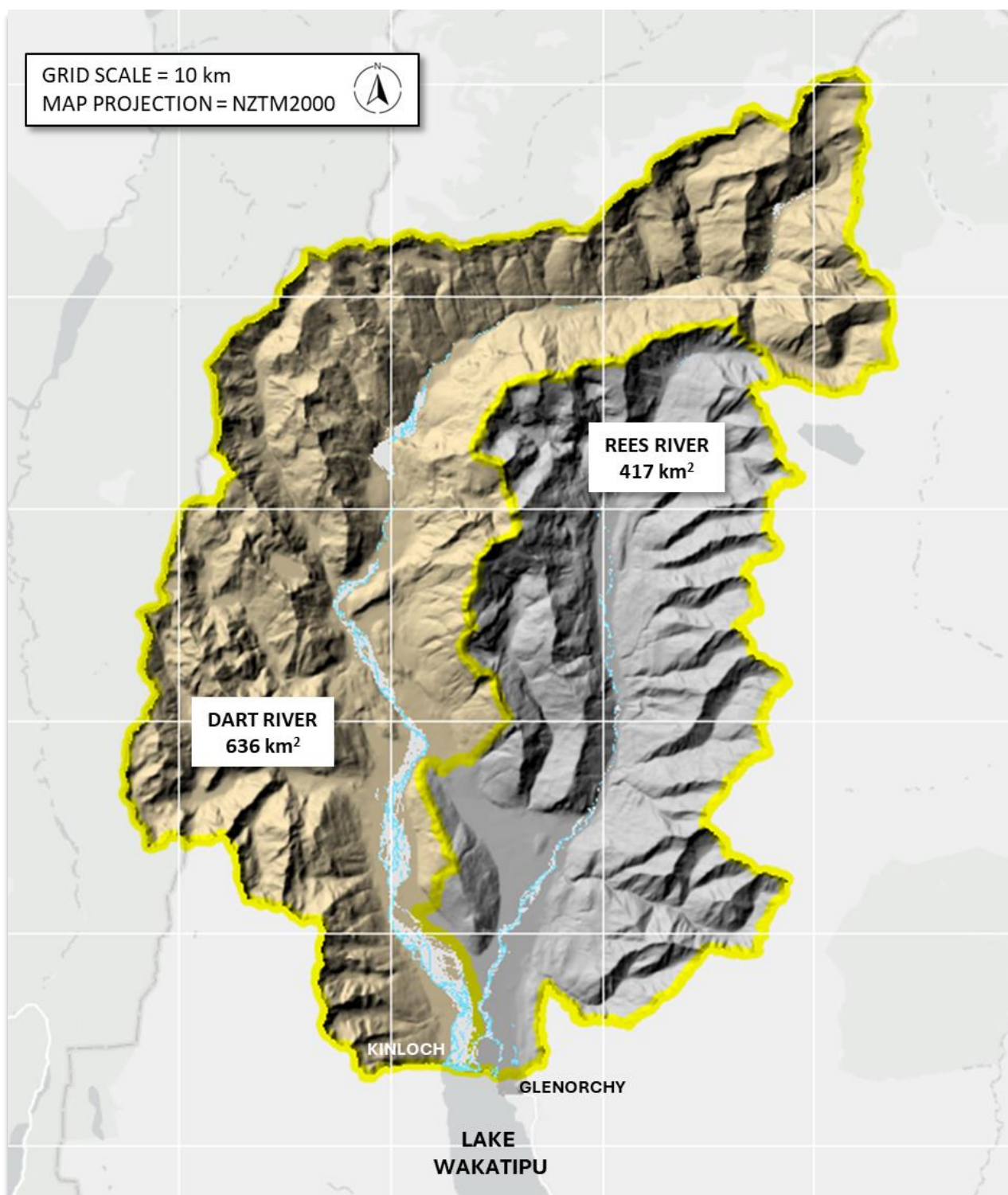


**FIGURE 1.** The Dart and Rees River catchments. Both rivers drain south, forming an extensive, 2.5 km wide delta with Lake Wakatipu. The townships of Glenorchy and Kinloch lie on the eastern and western shores of the delta respectively.



## 1.2. THE DART RIVER

The Dart River is the principal drainage into Lake Wakatipu, with its 636 km<sup>2</sup> catchment extending to the Main Divide. The headwaters of the Dart remain glacierized, though the current Dart Glacier, measuring less than 6 km in length, is a shadow of its maximum 130 km length in the Late Quaternary and has only a minor influence on catchment hydrology. Dowling et al. (2021) developed a Holocene record for the Dart Glacier that links historical observations of retreat with a <sup>10</sup>Be chronology and report observations that reveal glacier retreat of over 3 km in the last c. 100 years (1915-2018).

### 1.2.1 HYDROLOGY

Rainfall records for the Dart Catchment are limited to low altitude sites, with the only permanent continuously recording stations at the Hillocks (1,230,044E 5,031,5003N) and Paradise (1,231,140E 5,040,817N), see also Figure 3 below. Annual rainfall at the Hillocks (between 1998-2023) is 1693 mm/year (SD = 230 mm). Rainfall at Paradise, less than 10 km upstream, increases significantly to an annual average total of 2057 mm (SD = 290 mm) between 2004-2023. There are no gauges in the upper catchment, and it is likely that spillover in the headwaters results in substantially greater rainfall totals and that a large proportion of this falls as snow between April and October.

The Otago Regional Council maintain a rated river level recorder at the Hillocks that has been operational since June 1996. Data from this site reveal a mean flow of 80 m<sup>3</sup>s<sup>-1</sup> and a 7-day mean annual low flow (MALF) of 17 m<sup>3</sup> s<sup>-1</sup>. The river has a seasonal flow regime, with low flows occurring between June-August, when much of the catchment precipitation falls as snow, while flows peak in spring and summer between November to February (Figure 2).

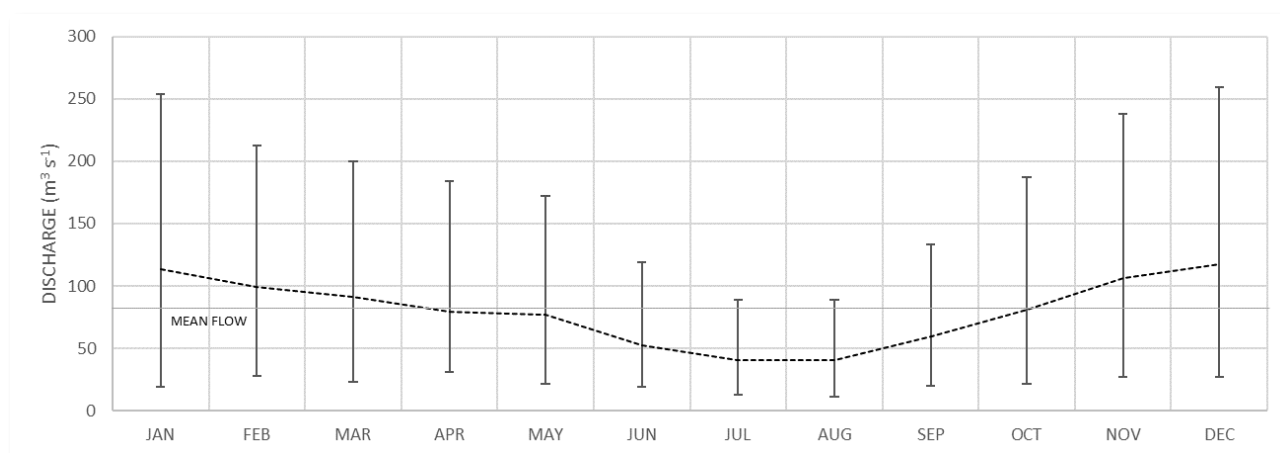


**FIGURE 2.** Seasonal variation in mean flow for the Dart River at the Hillocks, 1997-2000. Whiskers show upper and lower quartiles. Data sourced from Otago Regional Council.

The storm hydrograph recorded at the Hillocks exhibits a flashy response with a time-to-peak of typically less than 12 hours, followed by a rapid recession and return to low flow conditions. The flood of record (up to October 2024) occurred on the 3<sup>rd</sup> February 2020 and was estimated to peak at 1820 m<sup>3</sup> s<sup>-1</sup>.

Flood frequency was assessed recently by Mohssen (2021). In this analysis, flood hazard information for the Dart River (and Rees River, see 1.2.2) was compiled using both annual maximum and partial duration series. Mohssen (ibid.) found optimal fits to the observed record using a Generalized Pareto distribution fitted to the partial duration series and this was used to estimate the annual recurrence intervals for floods ranging from 5-500 years for the Dart River as shown in Table 1.

ANNUAL RECURRENCE INTERVAL (YEARS)	DISCHARGE ( $\text{m}^3 \text{s}^{-1}$ )
5	1390
10	1623
25	1928
50	2168
100	2420
500	3067

**TABLE 1.** Estimated peak flow on the Dart River for annual recurrence intervals ranging between 5-500 years, after Mohssen (2021).

#### 1.2.2. RIVER CORRIDOR

Downstream of the present-day terminus of the Dart Glacier, the Dart River runs for 61 km before its confluence with Lake Wakatipu. The extent of the valley floor was geomorphologically defined from the national LINZ 8 m Digital Elevation Model (DEM) using the approach of Alber and Peigay (2010). This uses elevations extracted from a river centreline and a set of longitudinal cross-sections (defined at 500 m intervals) to locally-detrended the regional DEM. The valley floor is then segmented from the surrounding hillslopes based a user-defined height threshold. The resulting valley floor is presented in Figure 3 and the valley floor elevations used to derive the long profile of the river corridor (see inset).

From the headwaters between river km 60-40, the river sits within a narrow, confined slot between 50-250 m wide. Holocene incision into the broader valley floor has created a steep, single thread channel with gradients varying between 2-5%. Periodic valley widenings, often associated with tributary fans, create focal points of aggradation that separate highly efficient transport reaches and generate notable breaks in slope (at river km 41 and 44 in particular).

Downstream of river km 40, the valley opens out into extensive river flats (Daleys and Dredge Flats) between 750-1000 m wide. These flats are linked to aggradation associated Slip Stream landslide at c. river km 32 (1,229,042E 5,052,424N). Slope failures at Slip Stream have been observed to impound the Dart as recently as January 2014. Over time, debris from Slip Stream has constructed a major 1 x 2 km fan that rises 150 m from the valley floor to its apex. Thomas and Cox (2009, see also Cox and McSaveney, 2014) analyzed the

structure and history of this landslide. They suggest that it is likely to have been activated during glacier retreat and estimate that it has delivered over 100 million m<sup>3</sup> of sediment to the valley floor.

The most recent significant activity at the slip occurred during January 2014. Following heavy rainfall, debris flows crossed the basal fan and temporarily dammed the Dart River. Further debris flows over the following two weeks continued to add to the fan and impounded a lake that grew from 0.47 km<sup>2</sup> to 1.48 km<sup>2</sup>. The initial dam breached quickly on the 4<sup>th</sup> January but there was no significant threat of a catastrophic outburst flood. Cox and McSaveney (ibid.) estimated that the debris flows added c. 1-2 M m<sup>3</sup> of sediment to the fan. More recent analysis reported within in Section 3.1, used high resolution DEM differencing techniques to estimate a sediment budget for this event, decomposing total erosion, sedimentation on the fan and delivery to the river. As reported below, this analysis found that the volume of material eroded from the Slip Stream complex exceeded 17.5 M m<sup>3</sup>, of which 6.8 M m<sup>3</sup> was deposited on the fan, implying a contribution of 10.7 M m<sup>3</sup> that has been reworked by the river.

Below Slip Stream, the Dart is once again confined until river km 28, where it opens out into the first of a series of major braided reaches, c. 2 km upstream of Chinamans Bluff. Between river km 28 to 10, this broad, braided planform varies in width between 500 – 1400 m, with local constrictions at Paradise (1,230,580E 5,040,431N) and the Hillocks (1,230,198E 5,031,577N). The gradient here falls to 0.001-0.002. For the distal 10 km of the river from the Hillocks to the Delta front, the Dart is extensively braided and below Mt Alfred, is separated from the Rees only by a narrow isthmus. The gradient of the river through the lower 10 km to the delta is slightly steeper at 0.003-0.004. Here, the Rees and Dart converge to create a delta front nearly 3 km in length that is actively prograding (see discussion below in 1.4). Over the past 50 years, the active corridor of the Lower Dart River has migrated westwards and minor engineering works (riprap, willow plantings and earthen stopbanks) have been used to arrest this trajectory with little success.

There are few published studies of bed substrate size for the Dart River. Wild (2013) reports size characteristics for two sites. The first of these is close to the Hillocks and the second from the delta front close to Kinloch. Shallow pits were used to create combined samples of surface and subsurface material, and the median grainsize was found to be 0.013 m (upstream) and 0.002 m downstream.

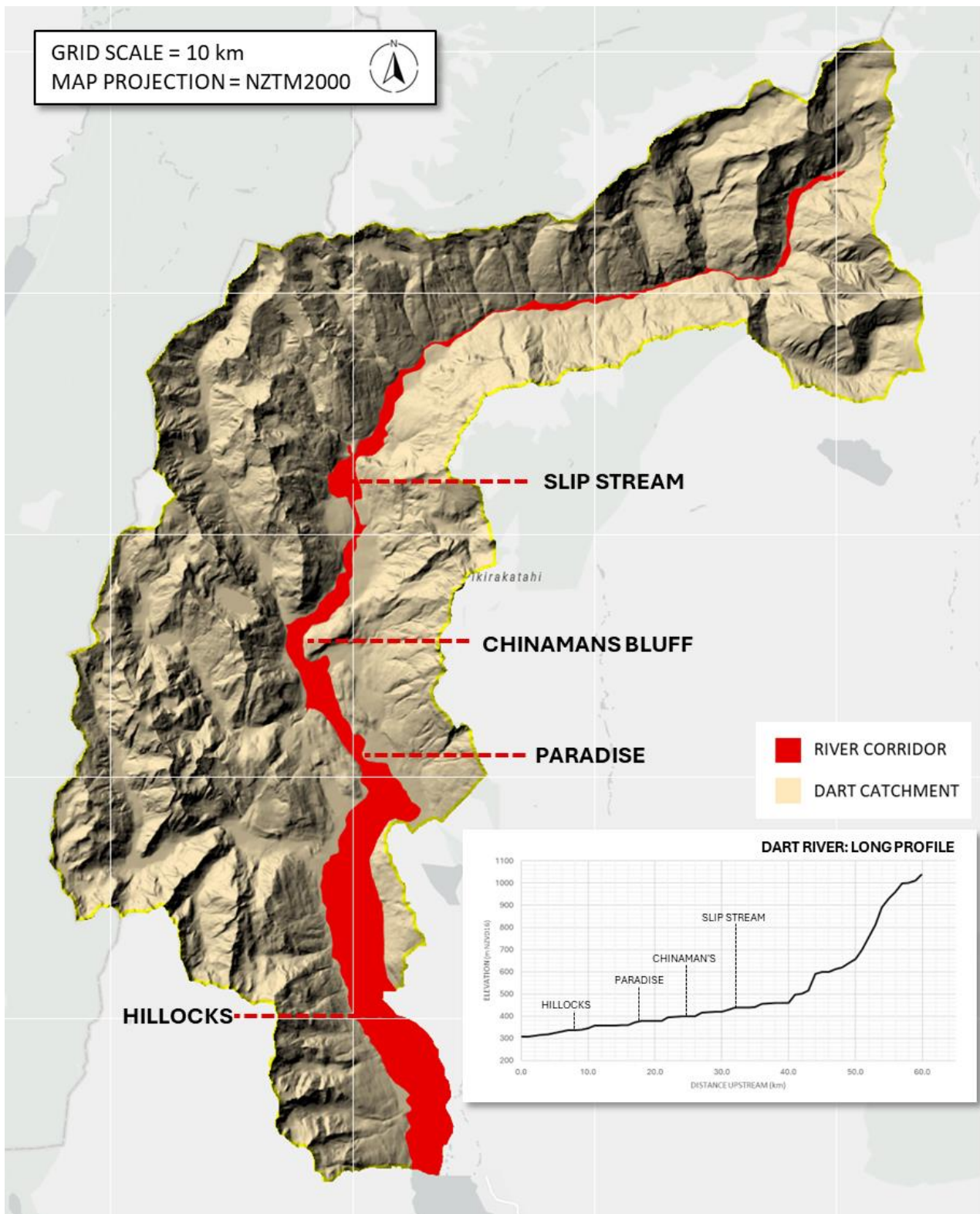


**FIGURE 3.** The Dart River corridor along its 61 km run to Lake Wakatipu. The long profile extracted from the mean valley floor elevation is shown on the inset, with gradients falling from between 2-5% headwaters to 0.3% in the delta.

## 1.3 THE REES RIVER

The Rees River shares many of the hydrological and geomorphological characteristics of the Dart River but is smaller in size (417 km<sup>2</sup>) and sheltered from the Main Divide. The Rees rises at a watershed shared with Snowy Creek (a tributary of the Dart) and whose upper slopes are covered by the Tyndall Glacier. The saddle between the Rees and Snowy Creek is only 1471 m. It is likely that this tributary of the Dart captured what was formerly the headwater of the Rees.

### 1.3.1 HYDROLOGY

Rainfall records for the Rees catchment are also limited to low elevation sites. Data from the Rees Valley Station (1998-2012; ORC, 2013) reveal a mean annual rainfall of 1462 mm for this low altitude gauge. Outside the catchment, the annual rainfall at Peats Hut (1,261,650E 5,027,150N) in the Shotover River catchment records an annual total of 913 mm, illustrating the strong eastward decline in rainfall with distance from the divide.

Unlike the Dart River, the Rees has only a comparatively short record of flow data. What does exist relates to a rated bedrock-controlled section at Invincible (1,239,920E 5,037,000N). This site was first maintained between 2009-2011 as part of a UK research project and was installed and maintained by NIWA (see Brasington, 2010; Williams, 2014 for details). During this period, the maximum recorded flow at the gauge was 475 m<sup>3</sup>s<sup>-1</sup> on the 6 February 2011. The gauge was recommissioned 10 years later in December 2021 and is now maintained by the Otago Regional Council. Since its reinstatement, the median flow is 10.3 m<sup>3</sup>s<sup>-1</sup> while the maximum flow measured is 241 m<sup>3</sup>s<sup>-1</sup>. In common with the Dart, the Rees exhibits seasonal variability in flow, with low discharges common during the winter months, and high flows in the spring, summer and autumn.

Both Williams (2014) and Mohssen (2021) have attempted to extend the observed record through correlation with the longer flow series from the Dart at the Hillocks. Both analyses reveal moderately strong correlation with a lag-time of 1 hour (Rees peaking before the Dart). Mohssen (ibid.) built on this analysis to develop a HEC-HMS rainfall-runoff model to estimate the 100-year average recurrence interval flow on the Rees at the Glenorchy-Paradise Road Bridge. Using regionalized, weighted rainfall statistics from the High Intensity Rainfall Design System (NIWA, 2018) and incorporating data from a range of regional rainfall stations (the Hillocks, Paradise and Cascade Hut) the 100-year ARI flood peak was estimated to be 941 m<sup>3</sup>s<sup>-1</sup>. Table 2 shows estimated peak flows for recurrence intervals between 25-100 years, using a downscaling factor to transform the 25 and 50 year ARI peaks from comparable data for the Dart at the Hillocks (Table 1).

ANNUAL RECURRENCE INTERVAL (YEARS)	DISCHARGE (m <sup>3</sup> s <sup>-1</sup> )
25	750
50	843
100	941

**TABLE 2.** Estimated peak flow on the Rees River for ARI ranging between 20-100 years, after Mohssen (2021).

### 1.3.2. RIVER CORRIDOR

The river corridor of the Rees was extracted following the method of Alber and Peigay (2010) and using the LINZ 8 m Digital Elevation Model. The result is shown in Figure 4, along with derived long profile on the inset.

The morphology of the river corridor shares many similarities with that of the Dart. The headwater reaches (between river km 41-31) are steep, confined and dominated by high gradient tributary inputs supplying large volumes of sediment, often in the form of debris flows. Below this, between river km 31-21 the valley floor widens to c. 1 km and the gradient falls to 0.001. Here the river exhibits a wandering planform, with an active width of between 100-300 m. These extensive flats bear a strong similarity to Dredge Flat above Slip Stream and again, the lower limits of this reach are demarcated by an active landslide complex, Muddy Creek (at river km 21). There is no historic record of Muddy Creek impounding the Rees, but sediment delivered from this sub-catchment has also constructed a steep, valley spanning debris fan, that is currently truncated by the Rees. A recent assessment of liquefaction risk across the Otago Region (Barrell, 2019) also highlights the likelihood that the Rees has previously been impounded by this debris fan.

Erosion of the toe-slope has created a bluff of between 5-30 m in height, declining either side of the apex of the fan. Flights of terraces are evident in the upstream flats and within the debris fan built by Muddy Creek. This suggests a recent history of downcutting, potentially associated with declining sediment delivery from the Muddy Creek complex, or distal base level change associated with the Holocene recession of Lake Wakatipu. Nonetheless, within the active delivery channel, there is evidence of contemporary debris flow activity and extensive sedimentation on the downstream flank of the fan. In common with Slip Stream, this sub-catchment is likely to represent the dominant source of sediment for the distal reaches of the river.

Below Muddy Creek, the Rees is confined in a steeper (0.01-0.02 gradient), cobble dominated reach until river km 17, where it widens upstream of another left-bank fan built by Invincible Creek. Downstream of the fan, the river is pinned against the true right valley wall and is downcutting into bedrock. This creates a relatively stable section where the river is currently gauged.

After flowing through a short narrow gorge, the Rees then opens into a wide, piedmont braided channel corridor downstream of Lovers Leap (river km 15).







The lower braidplain is highly dynamic and has an active width of between 200-400 m (and up to 600 m locally). There are minor river engineering works around and upstream of the Glenorchy-Paradise Bridge at river kms 8-10. There is also evidence of more extensive braided topography on the true right (now under pasture) that is bounded to the north by the Earnslaw Burn fan and confined further by an earthen stopbank constructed in the 1980s (ORC, 1999). A limited gravel mining operation exists within this reach and the ORC report (ORC, 2013) extraction of c. 27,000 m<sup>3</sup> between 2006 and 2013. Similar volumes were extracted in 2020 and 2021 (see section 2) and current activity is focused at the highway bridge in an attempt to enhance conveyance of flood flows. The volumes of gravel removed are small relative to the estimated sediment throughput and are unlikely to have had significant impact on river morphology.

Below Mount Alfred, the Rees and Dart merge into a 5 km wide sedimentation zone and a diffuence in the Rees at river km 2.5 currently diverts a minor portion of flow directly into the Dart. The gradient in the lower 10 km averages 0.0045.

In these lowest reaches above the delta front, historic aerial photography (Figure 5a and b) shows the Rees occupying a more easterly position than at present, with multiple, mobile distributary channels discharging into the current location of the Lagoon around the turn of the 20<sup>th</sup> Century and later into Lagoon Creek. These images provide compelling evidence of the high rates of landscape evolution in the lower reaches of both the Dart and Rees rivers.



**FIGURE 5.** Oblique aerial image revealing historic distributary patterns in the Lower Rees River. A) Photo #5113 *Tooth Peaks and Glenorchy, Lake Wakatipu* from the Muir and Moodie (Burton Brothers), c. 1900; B) Whites Aviation Ltd: Photograph Ref: WA-08842-F. Alexander Turnbull Library, Wellington, New Zealand, 1947.

A longitudinal survey of bed material composition of the Rees was undertaken in 2009 as part of a UK-funded research programme (Brasington, 2010). The survey involved pebble counts of surface grain-size taken from 12 sites stretching from river kms 3 to 24. These data are presented in Williams (2014) and the longitudinal variation summarized below in Figure 6. Upstream of Muddy Creek, (river km 24), the median particle is very coarse gravel. Downstream of Muddy Creek, the surface sedimentology coarsens to a small cobble due to the injection of coarse sediment and confinement of the channel between river kms 19-18. Further downstream, the riverbed material exhibits distinctive downstream fining (see Rice and Church, 2010), with a change in the median size of  $11.4 \text{ mm km}^{-1}$  between the mountain front and most distal sample. The bed composition is also progressively more sorted downstream of Muddy Creek, reflecting the wide size-range of clasts input by debris flow processes from this sub-catchment.

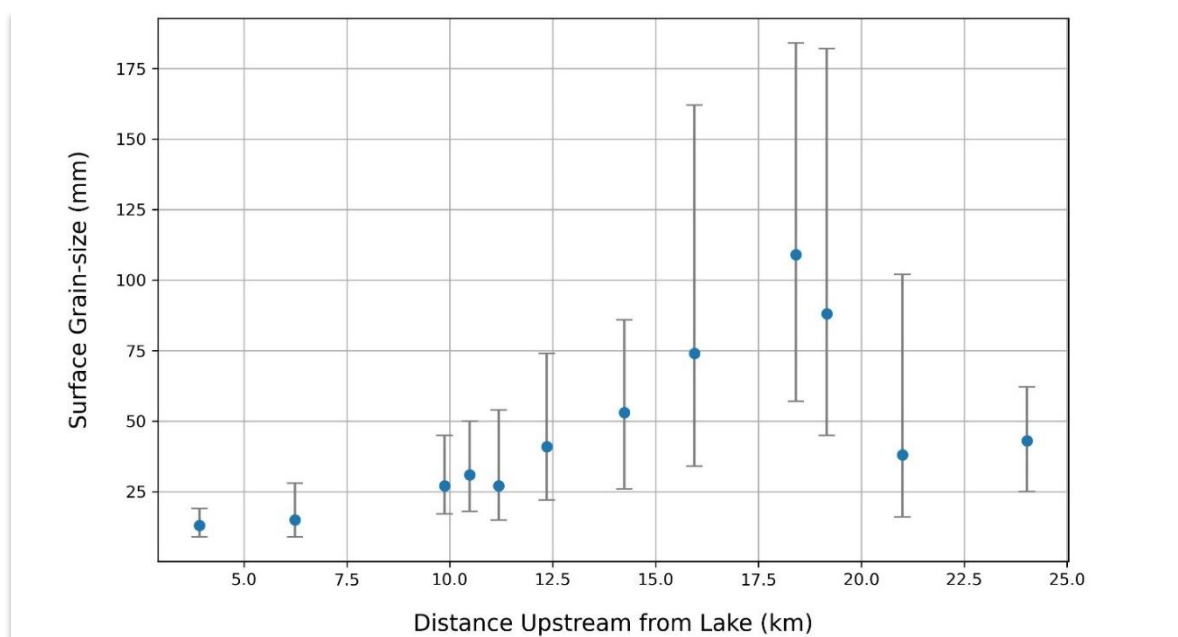


**FIGURE 6.** Box-and-whisker plots showing longitudinal trends in surface grain-size. Median,  $D_{50}$ , is represented by the dot, while the whiskers extend to  $D_{16}$  and  $D_{84}$  respectively. Samples were taken from randomly selected locations on bar heads. At each site, 100 clasts were sampled using a  $1 \text{ m}^2$  frame.

## 1.4 THE DELTA AND LAKE WAKATIPU

The Dart and Rees Rivers coalesce into a 3 km wide delta front with Lake Wakatipu, the third largest lake in New Zealand. The rivers represent the principal flows into the lake, which now drains through the Kawarau River at Frankton. The level of Lake Wakatipu has been monitored since 1924 and generally lies in the range of 309.4-311.0 m. The range reflects the balance between inflows and outflows and the maximum recorded level is 312.78 m in November 1999. High lake levels are influenced by the timing of peak flood flows from the Shotover River, the confluence of which lies just c. 3 km downstream of the lake outlet at Frankton. High flows on the Shotover River coupled with the low gradient of the upper Kawarau can result in reduced conveyance of the lake outlet channel and, in extreme situations, may even reverse the flow back into the

lake (see Webby and Waugh, 2006 for further discussion). Levels above 312 m pose a risk of flooding to many of the lakeside communities, including Glenorchy.

Mohssen (2021) used hourly lake level data from Willow Place in Queenstown (dating from 1962) along with daily level data from 1924 to compute an annual maxima series of lake levels. These data were supplemented by historic levels from floods in 1878 and 1919. Using this series, the average recurrence intervals were estimated using a Generalized Pareto distribution and are shown in Table 3 below.

ANNUAL RECURRENCE INTERVAL (YEARS)	LAKE LEVEL (m)
5	311.19
10	311.54
25	311.97
50	312.23
100	312.57
200	312.85

**TABLE 3.** Lake Wakatipu levels for a range of ARIs between 5 and 200 years, after Mohssen (2021).

#### 1.4.1 SEDIMENTATION AND DELTA PROGRADATION

As discussed in 1.1 above, it is likely that Lake Wakatipu – with palaeo-shorelines reaching elevations of 360 m – once extended upstream as far as Camp Hill (on the Rees) and the above Hillocks (on the Dart). Subsequent recession of the lake down to its present height of c. 309 m has resulted in Holocene infilling of the lower Rees and Dart valley floors. Lalor and Purvis (1970) report stratigraphic logs derived from four boreholes in the Rees braidplain, between the Lagoons and Lovers Leap. These are summarized in Figure 7 (after Williams, 2014). The two upper sites reveal graded sediments comprising coarse to fine sandy gravels with no discernible bedrock bottom to depths of >50 m. In the downstream boreholes, sandy gravels give way to lake sediments (silts and clays) at depths of 15-30 m, shallowing towards the current shoreline.

These stratigraphic data indicate progressive sedimentary infilling, which over contemporary timescales, is evidenced by increasing river bed levels (see Section 2) and progradation of the delta. This is consistent with anecdotal observations and early survey plans (see URS, 2007) that suggest that the Rees-Dart delta has been advancing for at least the last 150 years. A more recent comparison with the earliest reliable metric photography from 1966 reveals advances of between 100-250 m of the Rees and active areas of the Dart delta over the last c. 60 years.

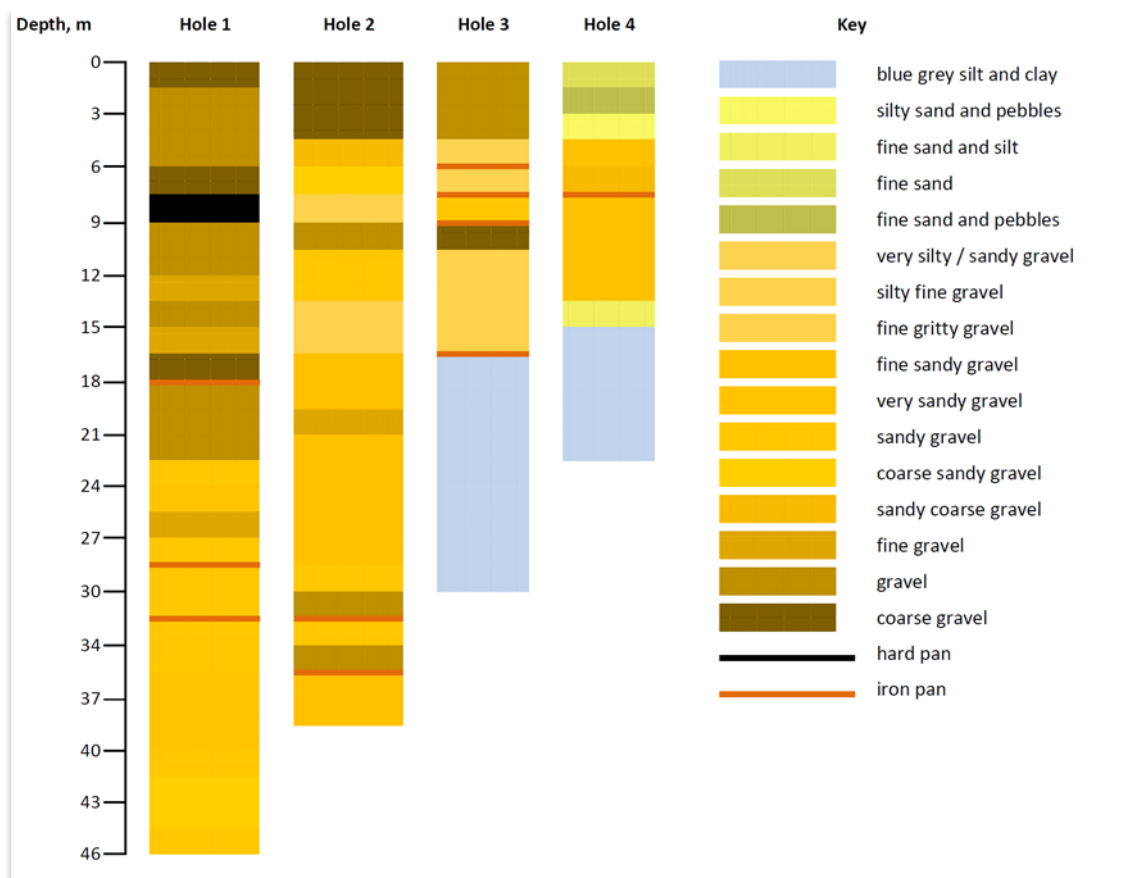


**FIGURE 7.** Stratigraphic logs interpreted from Lalor and Purvis (1970) and reproduced by Williams (2014). Approximate locations for the four holes are: Hole 1 (1,239,820E 5,036,330N); Hole 2 (1,238,515E 5,034,830N); Hole 3 (1,236,630E 5,031,075N); Hole 4 (1,235,400E 5,024,680N);

The morphological structure of the delta is revealed by bathymetric surveys reported by Wild (2013). More recently, multibeam sonar surveys have been undertaken by NIWA (Coursey and Mountjoy, 2022) though these data are not yet publicly available. Wild (ibid.) mapped only single transects, but nonetheless was able to show the rapid transition from topsets to steep sloping foresets (15-30°) within 20 m of the shoreline across the delta front. The transects reveal a linear to concave profile that attains a depth of 90-100 m (210-220 m elevation) within less than 1 km of the shoreline. Wild (ibid.) combined these sonar transects with historic bathymetric data to interpolate the changing delta morphology between 1966 and 2007. The data were converted into gridded elevation models which were then differenced to estimate sedimentation rates by computing the volume of the sediment prism. The results of this analysis are reproduced here in Figure 8.

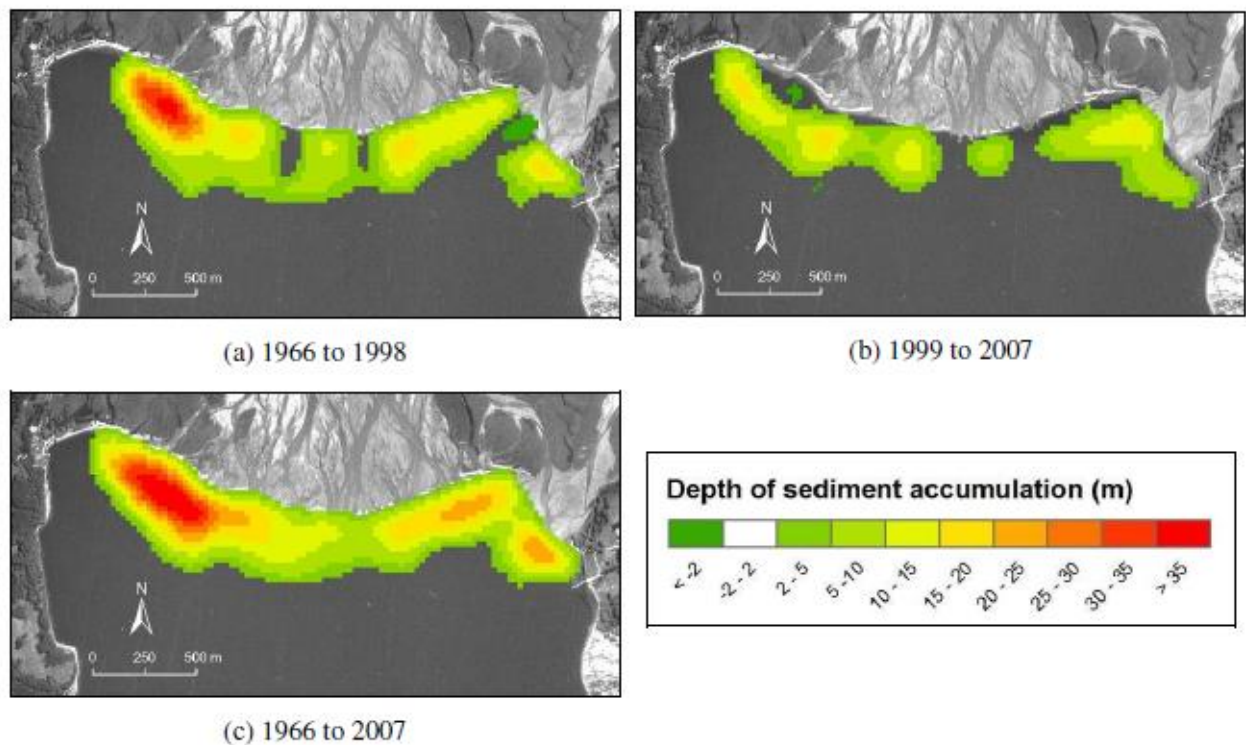


**FIGURE 8.** Depth of sediment accumulated on the Rees-Dart delta over the period 1966-2007, after Wild (2013).

The analysis shows extensive sedimentation across the delta front focused, in particular, on the true right of the Dart closest to Kinloch and associated with the sediment delivered from the Rees. This pattern reflects the westerly migration of the Dart River since (at least) the late 1960s as discussed in Section 3. Based on the mapped sediment prism and relative discharge, Wild (*ibid.*) provides a first order estimate for bedload delivery to the delta from both the Rees and Dart as  $30,000\text{--}70,000 \text{ m}^3 \text{ yr}^{-1}$  and  $180,000 - 270,000 \text{ m}^3 \text{ yr}^{-1}$  respectively.



## 2. CHANNEL MORPHOLOGY AND DYNAMICS

### 2.1 GEOMORPHIC STRUCTURE OF THE LOWER REES-DART BRAIDPLAIN

The Rees and Dart Rivers are actively infilling the sedimentary basin created by the recession of Lake Wakatipu. In their lower reaches downstream of Mt Alfred, the rivers coalesce to create a c. 4-5 km wide aggradation zone. Both rivers exhibit laterally mobile braided planforms, evolving dynamically in response to the combination of high sediment supply, unconsolidated bed material and the unconfined setting.

The geomorphic structure of the valley floor in the lower 10 km of the rivers is revealed in Figure 9. This shows a 'Relative Elevation Model' or REM, constructed by locally-detrending a 1 m resolution lidar-derived DEM acquired for the ORC in 2019. Specifically, the absolute elevations are normalized relative to the mean bed level of the nearest (orthogonally) active channel corridor (i.e., the Rees or Dart). The resulting map thus shows the height of the valley floor relative to this hydromorphological datum, with relative elevations colour-scaled from -3.0 to +3.0 m, symmetrically about zero.

The REM highlights the antecedent imprint of the enlarged Lake Wakatipu. Well-established palaeo-shorelines documented around the wider lake are also evident along the true left valley wall of the Rees, stretching upstream beyond 12 Mile Creek (see Cook et al., 2014 and Sutherland et al., 2019). These provide compelling evidence that the lake previously encompassed the entire valley floor shown in Figure 9 and stretched beyond to include Lake Reid and Diamond Lake. The presence of multiple shorelines at the Bible Terrace above Glenorchy attests to a complex history of lake level adjustment, with periods of comparative stability punctuated by rapid change (Sutherland et al., 2019). This pattern is most likely controlled by unsteady incision of the Kawarau outlet channel. Mackey (2015) reports evidence of submerged shorelines in Frankton Bay, at an elevation of 305 m, suggesting a more recent history of lake rise, possibly associated with reduced outflows due to landsliding in the Kawarau.

The current valley floor morphology reflects differential rates of sedimentary infilling of this basin and reworking by the principal channel belts. Dominant features include the marginal fans associated with Precipice Creek, 12 Mile Creek and Earnslaw Burn and what has been inferred to be a landslide deposit at the Hillocks (McColl and Davies, 2011; McColl et al., 2019). The Rees and Dart are the main axes of sediment transport and the REM shows the Rees to be superelevated above the surrounding marginal basins, evidencing the high rate of aggradation. This is a highly unstable configuration as illustrated by cross-sections XS1 and XS2 plotted on Figure 9. There is a high probability that the Rees may avulse – and has likely avulsed periodically in the past - into these depressions.



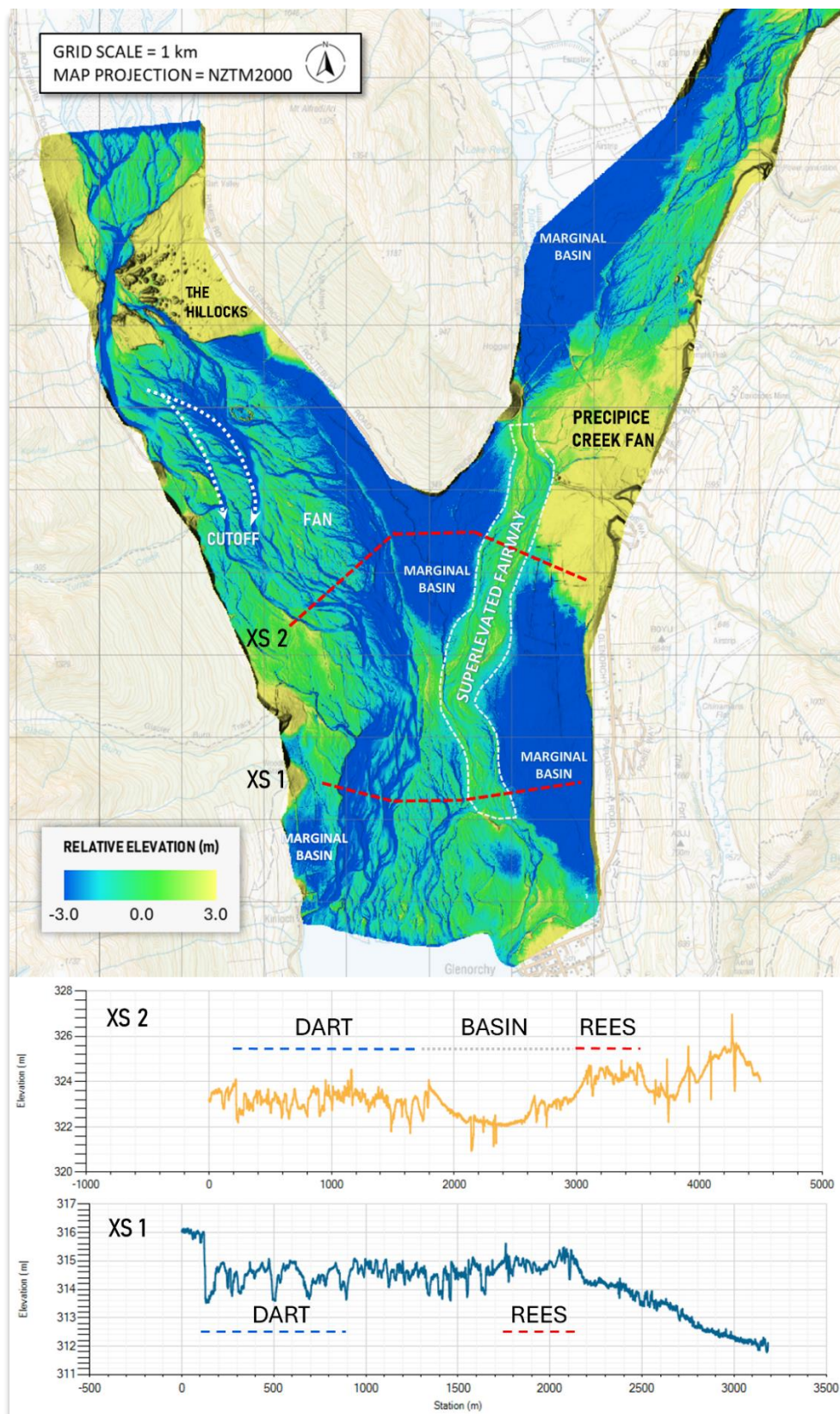


**FIGURE 9.** Relative Elevation Model (REM) of the lower 10 km of the Rees-Dart Rivers. Cross-sections XS1 and XS2 reveal the elevation profile of the wider valley floor below Mt Alfred, highlighting the currently superelevated active channel of the Rees River and the marginal topographic depressions (note the different horizontal scales).

Between river kms 5-10, the Dart exhibits the characteristics of a low gradient fan, infilling the basin to the east (true left). As described below in Section 3, the recent pattern of decadal-scale channel migration reveals the active corridor of the Dart to have migrated westwards (towards the true right) over the past 50-years. This has led to significant bank erosion between river km 3-7. The REM shows the migration to be linked to a switch at the apex of this fan that has reorientated the principal anabranches along a shorter, steeper westerly axis. Further downstream, westerly migration of the Dart, leading to further bank erosion between river km 1-3, appears to be a response to aggradation in the apex of the valley (see section XS1).

This large-scale morphological context highlights the likelihood of significant lateral channel migration occurring on both rivers. High rates of sediment transport through the principal drainage axes of the Dart and Rees lead to aggradation of the active channel, that in turn adjusts by migration, widening or avulsion. Over centennial timescales, on-going adjustment serves to fill the wider sedimentary basin.

## **2.2 BED-LEVEL ADJUSTMENT ON THE REES RIVER**

Concerns that high rates of fluvial sediment transport and progradation of the delta may elevate risks of flooding and threats to infrastructure due to riverbed aggradation have long been established. Particular areas at risk include Glenorchy-Paradise road, the Glenorchy-Paradise Bridge, the northern perimeter stopbank in Glenorchy and the Kinloch Road. Anecdotal and photographic evidence has suggested significant aggradation at the Glenorchy-Paradise bridge since its construction in 1950 (see ORC, 2019).

The Otago Regional Council have monitored a series of monumented cross-sections throughout the lower Rees to support assessments of channel conveyance and sustainable gravel extraction. Sections were initially established between 1978-1987 and are distributed from the delta to Lovers Leap with an approximate mean spacing of 1000 m but vary between 500 – 3000 m. A series of ORC reports between 2003-2019 document mean bed-level changes across the active channel width (ORC, 2003; 2008; 2017 and 2019). The time elapsed between surveys varies by section and the last comprehensive re-survey was conducted in 2011, with partial re-surveys of the downstream sections in 2015 and 2019. The early reports in 2003 and 2008 suggest a consistent trend in aggradation with typical increases in mean bed level of between 0.01-0.02 m yr<sup>-1</sup>.

### **2.2.1 RELIABILITY OF CROSS-SECTION SURVEYS**

An updated analysis in 2019 found only weak evidence of any trend in bed level change and highlighted the difficulty of establishing robust inferences due to:

- high rates of lateral channel mobility, affecting section orthogonality;
- inconsistent definitions of active width;
- the use of multiple vertical datums.

The reliability of mean bed level estimates depends on how frequently cross-sections are spaced and how complex the channel shape is. The advent of fully distributed models of channel topography (i.e., DEMs)

generated through airborne lidar and/or digital photogrammetry, has enabled statistical assessments of the effect of undersampling topography.

Lane et al. (2003) report numerical experiments with photogrammetric DEMs of the Waimakariri River to assess this bias. Their results reveal that for section spacings of less than 100 m, error rates were typically below 10%. However, for lower spatial frequencies, the error rate grew significantly and exceeded 100% for spacings greater than 500 m. This bias can flip the interpretation of bed-level changes (e.g., from aggradation to degradation), raising concerns about current monitoring practices in New Zealand. In this context, it is noteworthy that Brasher's (2006) review of practice around NZ revealed that typical section spacings were between 300-1500 m, similar those used on the Rees.

## 2.3 DEM DIFFERENCING

Technological advances in airborne survey, most notably through lidar and softcopy photogrammetry have enabled the acquisition of continuous digital elevation models (DEMs) with high spatial fidelity (see Tomsett and Leyland, 2019 for a review). These data create new opportunities to monitor channel, indeed landscape-scale, kinematics through the differencing of time-sequential terrain models (Vericat et al., 2017). This approach can be applied directly to 3D point cloud data (Lague et al., 2013; Winiwarter et al., 2021) but due to indeterminacies in the vector of topographic change and the definition of an integration volume, is more commonly applied to quantify vertical (elevation) changes using raster, or gridded elevation data. DEM differencing enables direct identification of the vertical components of erosion and sedimentation which can be integrated spatially to compute the areal, volumetric or average elevation (bed-level) changes over time.

### 2.3.1 MANAGING DEM UNCERTAINTY

While the principles of DEM differencing are comparatively straightforward, the results may be strongly influenced by the quality of the underlying elevation models. Uncertainty in the net elevation change incorporates errors in the individual DEMs ( $\delta z$ ) so that modelled elevations should be represented as:

$$Z_{Actual} = Z_{DEM} \mp \delta z \quad 2.1$$

where,  $Z_{Actual}$  is the true elevation and  $Z_{DEM}$  is the estimated elevation at that point. Brasington (2003) showed that the individual errors in the DEMs are propagated into a DEM of Difference, or DoD, as:

$$\delta u_{DoD} = \sqrt{\delta z_{new}^2 + \delta z_{old}^2} \quad 2.2$$

where,  $\delta u_{DoD}$  is the propagated error in the DoD and  $\delta z_{new}$  and  $\delta z_{old}$  are the errors in the *new* and *old* DEMs used to compute the elevation change. This method assumes that the DEM errors are randomly distributed and independent but can be treated as spatially uniform (i.e., as a single value for the entire DEM), spatially

distributed (i.e., co-varying with a driver of DEM quality such as vegetation cover) and can be specified individually for each DEM.

This framing of uncertainty provides a basis for assessing the significance of apparent changes in elevation computed through DEM differencing. Essentially, the key question is to establish a threshold that partitions the geomorphic signal of elevation change from the noise that results from combining DEM errors. Brasington et al. (2003) and Lane et al. (2003) both draw on the statistical theory of errors (Taylor, 1997) to show how a probabilistic threshold can be defined for a given confidence interval. They demonstrate that if the estimate of DEM error,  $\delta z$ , can be assumed to be a reasonable approximation of the standard deviation of error (*SDE*), equation 2.2 above can be reformulated as:

$$U_{crit} = t \left( \sqrt{SDE_{new}^2 + SDE_{old}^2} \right) \quad 2.3$$

where  $U_{crit}$  is the critical error threshold, assuming that errors are distributed according to Student's  $t$ -distribution and where:

$$t = \frac{|Z_{DEM_{new}} - Z_{DEM_{old}}|}{\delta u_{DoD}} \quad 2.4$$

The term,  $|Z_{DEM_{new}} - Z_{DEM_{old}}|$  is the absolute value of the DoD change model. The probability of a predicted change occurring due to chance measurement error can then be calculated by relating the computed  $t$ -score (2.4) to its cumulative distribution function. This approach provides a flexible method to threshold predicted changes according to their likelihood and segment them from 'noise'.

A 0.05 significance level ( $\alpha$ ) is commonly used to test for differences. This conservative approach reduces the chance of false positives (Type I errors), where a change is identified even if none exists. While this may be appropriate for high consequence decisions, for example, to set lethal doses or evaluate the efficacy of drug treatments (see Payton et al., 2003), tests designed for high Type I error rates may be overly conservative in a noise-rich, environmental context.

This issue is important in the context of the analysis of fluvial morphodynamics for two reasons. First, the vertical expression of fluvial processes is often a similar magnitude to the accuracy and precision of DEMs. Robust segmentation of signal:noise is therefore challenging, requiring high fidelity DEMs with accurate horizontal and vertical co-registration. While random errors will likely sum to zero (Anderson, 2019), systematic differences between repeat surveys, such as mismatched datums or survey blunders, may introduce significant bias.

The second problem relates to the asymmetry of the vertical changes produced by fluvial processes. Scour and bank erosion create localized and high magnitude elevation changes, while sedimentation is spatially

dispersive and dominated by low amplitude sheets of bed material. This disparity means that symmetric tests for significance in elevation change are likely to treat these processes unevenly. Such tests may overemphasize the effects of erosion while underestimating deposition. In the limit, for a region in geomorphic balance - where the volume of erosion matches deposition – overly conservative significance tests may generate an apparent a negative bias. This happens because erosion, being more spatially concentrated, is more likely to exceed the detection threshold, while sedimentation is overlooked.

A further problem for quantifying morphological change in fluvial systems is the presence of inundated areas which are rarely resolved bathymetrically. Emerging technologies like shortwave (532 nm) topo-bathymetric lidar offer promising solutions to address this critical data gap (Stout and Brasington, 2022). Such datasets remain scarce however and most DEMs are hydroflattened so that the elevation of submerged areas is recorded as the water surface elevation at the time of the survey. Despite this, flashy, laterally mobile rivers such as the Rees and Dart remain good candidates for DEM differencing as at low flow, much of the channel bed is subaerially exposed. Moreover, assuming that river levels between surveys are similar, and that the lateral migration of the active anabranches is locally-balanced (scour=deposition), then the predicted mean bed level change will be robust even though the total volume of material transferred is likely to be underestimated.

## 2.4 SURVEY DATA AND UNCERTAINTY MODELLING

Four airborne lidar surveys have been acquired over the lower Dart and Rees since 2011. The extent of these surveys varies as shown in Figure 10, while a summary of the survey acquisitions is presented in Table 4.

	2011	2019	2021	2022
<b>DATE</b>	3 OCTOBER	25 JUNE	9 AUGUST	18 OCTOBER
<b>DATUM</b>	DUN 1958	NZVD 2016	NZVD 2016	NZVD 2016
<b>SENSOR</b>	OPTECH ALTM3100	LEICA ALS60	RIEGL VUX240	RIEGL VUX240
<b>FLYING HEIGHT (m)</b>	1200	1500 – 2400	300	300
<b>DENSITY (pts/m<sup>2</sup>)</b>	2	4	40	40
<b>Z QUALITY (<math>\sigma</math>, m)</b>	0.026	0.104	0.032	0.035
<b>SUPPLIER</b>	AERIAL SURVEYS	LANDPRO	UNI. CANTERBURY	UNI. CANTERBURY

**TABLE 4.** Acquisition specifications and reported quality metrics for the Rees/Dart Lidar surveys.



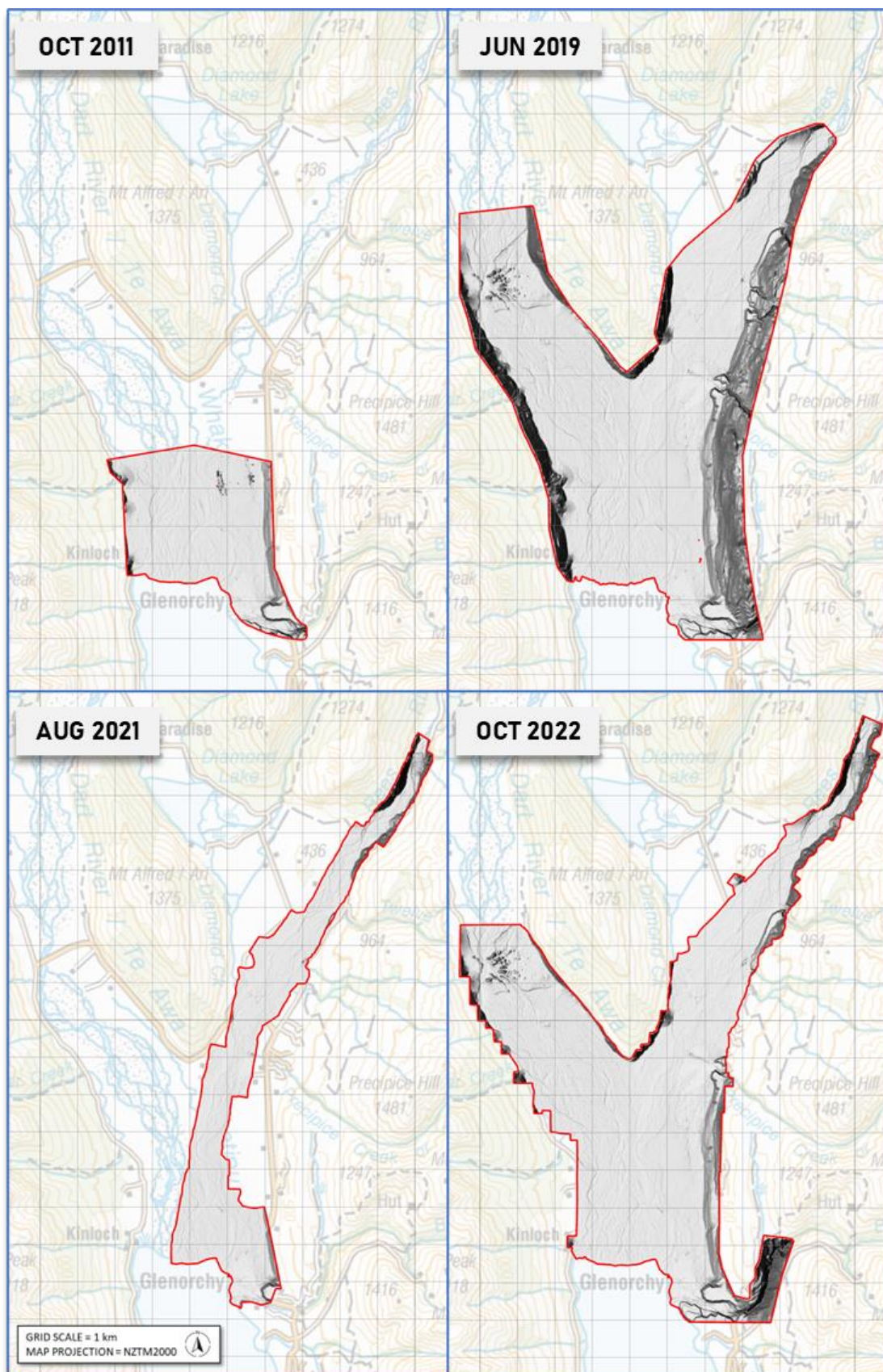


**FIGURE 10. Timeseries of 1 m DEMs. The 2011 survey covers only the lower 3-4 km of the delta, while 2019 and 2022 extend over the wider valley floor. The 2021 survey is limited to the active corridor of the Rees.**

The quality metrics in the supporting data reports are based on an unspecified number of ground control points. Information on these reference observations (i.e., the survey method), their location and surface cover are also unavailable. In some reports, it is also unclear whether reference observations were used for both lidar calibration and independent quality assessment. Even assuming these estimates are reliable and spatially consistent, there remain untestable ambiguities surrounding ground penetration through vegetation and the impacts of point density on the interpolation and quality of the derived raster 1 m DEMs.

#### 2.4.1 DEM REGISTRATION AND QUANTIFYING UNCERTAINTY

While absolute registration to an independent coordinate reference system is desirable, DEM differencing involves the assessment of change between surveys. This requires an assessment (and correction if needed) of the co-registration of the gridded DEMs. This was examined by first transforming the 2011 DEM to same vertical (NZVD2016) datum as the 2019, 2021 and 2022 surveys using a datum relationship grid produced by Land Information New Zealand (<https://data.linz.govt.nz/layer/53428-dunedin-1958-to-nzvd2016-conversion/>).

Co-registration of the DEMs was then assessed by computing elevation differences in a set of reference areas that, through visual inspection, were assumed to have remained geomorphologically stable over the period. A total of 26 reference polygons were digitized (Figure 11). These vary in size between 333 to 19,888 m<sup>2</sup> and incorporate land cover classes of increasing complexity: ROAD (n=6); PASTURE (n=11); SCRUB (n=5); TREES (n=4). The surveys in 2011 and 2021 are confined to the active river bed, limiting the number of stable reference locations. Only nine reference sites were within the bounds of the 2011 survey and 18 within 2021, while the full set of 26 polygons were used to analyse the fit between 2019 and 2022.

Elevation differences within each polygon were computed for all DEMs pairwise, resulting in six sets of differences: 2011-2019; 2011-2021; 2011-2022; 2019-2021; 2019-2022; 2021-2022. For each reference area, descriptive statistics of the elevation differences were computed and then aggregated by-year and by-land cover. The results are presented as box-and-whisker plots in Figure 12, showing the interquartile range ( box) and median (centre bar), while the grand mean (by year and by cover class) and the pooled standard deviation (weighted to account for sample size) are shown as labels. The complete dataset is presented in Appendix 1.

This provides a data rich assessment of DEM co-registration, incorporating changes over >600,000 m<sup>2</sup>. It should also be stressed that the metrics reflect differences between models, not an assessment of absolute DEM accuracy relative to a reference standard and thus computed differences combine uncertainties in two DEMs being compared.



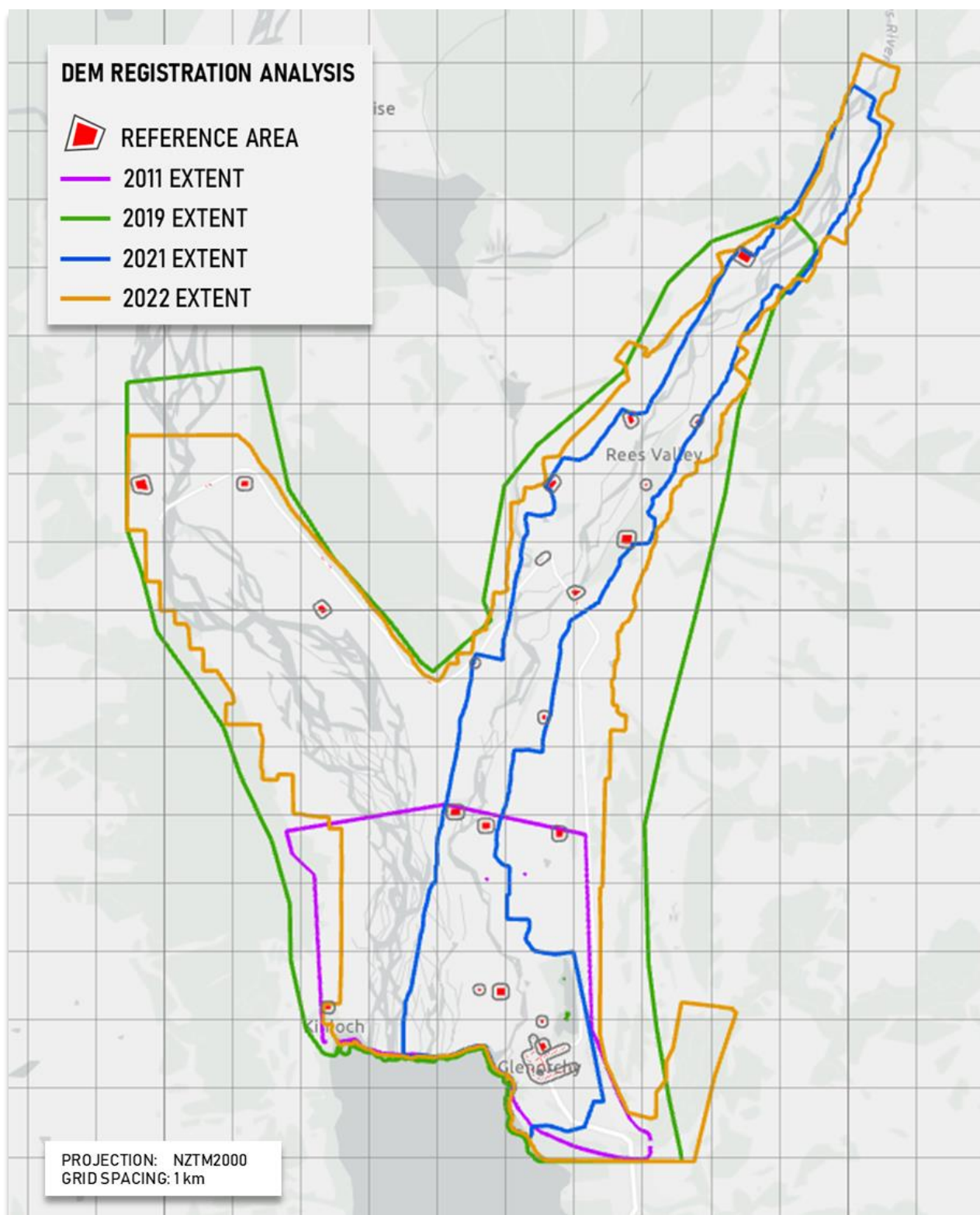


**FIGURE 11.** Distribution of reference areas used for the co-registration assessment. A total of 26 sites were manually identified using aerial imagery and hillshade models to assess their stability. These are distributed across a range of land cover types, including hard points on roads and across a range of more vegetated land covers of varying density (pasture < scrub < trees). The extent of each survey is shown by the bounding polygons revealing the range of sites available to assess the registration quality between years.

The grand mean, combining all samples over all pairwise assessments of the reference sites, is just 0.02 m (grand absolute mean = 0.057 m) and the standard error 0.008 m ( $\sigma/n^{0.5}$ ). Figure 12 provides a more granular assessment of differences by year (A) and by land cover (B). Differences by year have means that vary between -0.024 – 0.078 m. The results appear to show that 2011 is ‘high’ relative to 2019, 2021 and 2023 (positive difference residuals). However, closer examination of the differences by land cover between 2011 and the later surveys, shows that this high mean is strongly influenced by differences in the scrub cover class: 0.16, 0.14, 0.155 m for comparisons with 2019, 2021 and 2022 respectively. By contrast on roads, the variation is just 0.007, 0.083 and 0.058 m for 2019, 2021 and 2022 respectively (see Appendix 1).

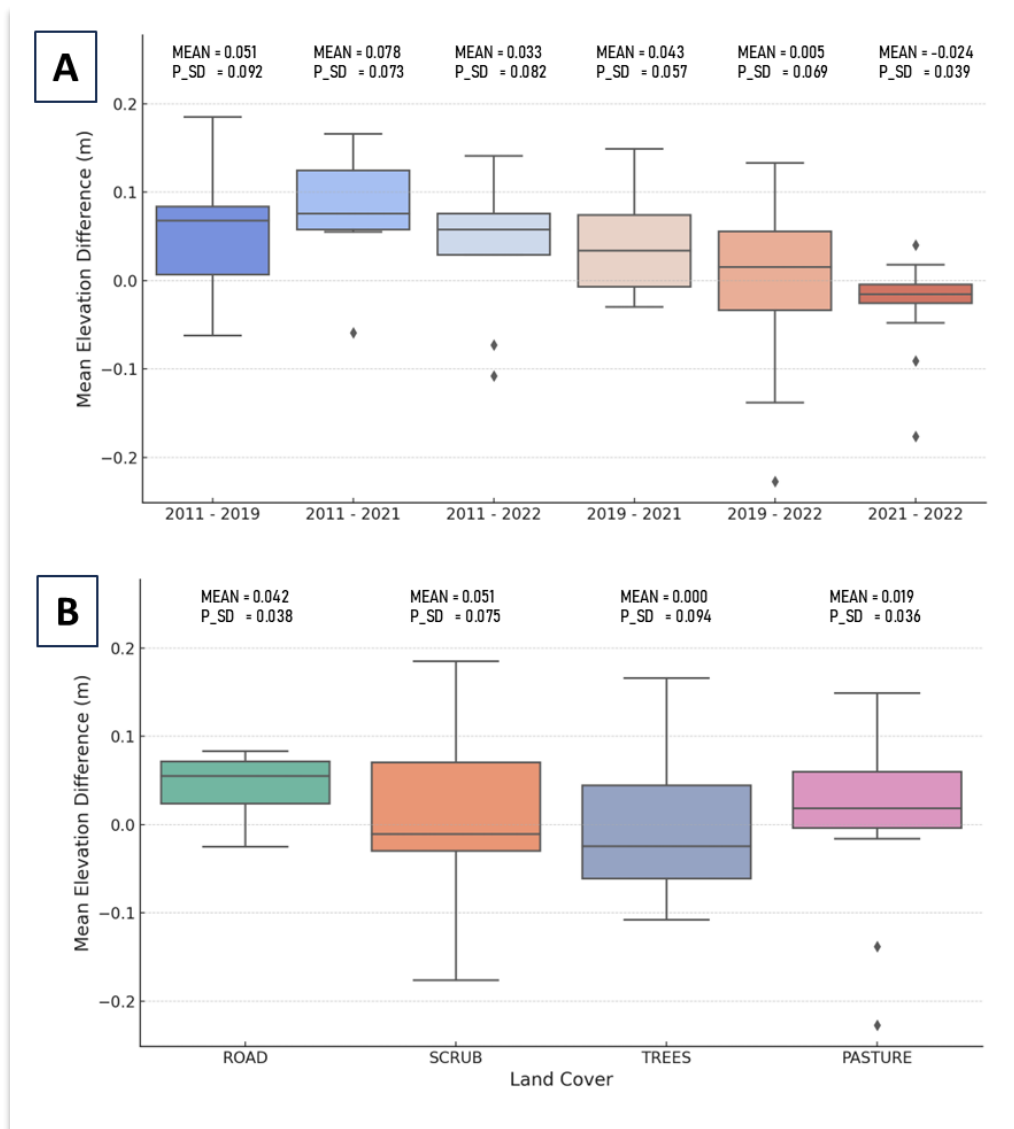


**FIGURE 12.** Elevation differences in stable reference areas aggregated by pairwise year comparisons and by land cover classes. The box and whisker plots show the median (central bar) and interquartile range (box) while the grand mean and pooled standard deviations are presented as labels. All differences in metres.

These comparisons represent the longest interval over which changes occur (8-11 years). They also incorporate the effects of lower point density in the 2011 survey, which is linked to a reduced likelihood of

laser pulses penetrating dense vegetation. Failure to penetrate to ground could account for net positive elevation bias under vegetated land covers. This effect is, however, less likely to confound the analysis of change on the more significant bare gravel surfaces as indicated by the improved fit between surfaces on the road cover class.

The vertical correspondence of the 2019, 2021 and 2022 surveys is improved, with mean differences of -0.024 to 0.043 m. The pooled standard deviation (a measure of precision) by year reveals a tight fit between 2021-2022 ( $\sigma = 0.039$  m). Both these surveys were undertaken by the same operator and were acquired at a high nominal point density (40 ppsqm). By contrast, the fits between 2019-2021 and 2019-2022 exhibit greater variance,  $\sigma = 0.057$  m and 0.069 m respectively. This is consistent with lower precision of the 2019 dataset indicated in the survey report as shown in Table 4. Overall, though, the pooled  $\sigma$  across years varies from just 0.039 m to 0.092 m suggesting reliable surface comparisons over the stable reference areas.

Elevation differences on the land cover classes irrespective of year reveals an expected pattern; lower variance for the 'smoother' road ( $\sigma=0.038$  m) and pasture ( $\sigma=0.036$ ) cover classes relative to the denser vegetation cover on scrub ( $\sigma=0.075$ ) and tree ( $\sigma=0.094$ ) reference areas.

In summary, the results of this extensive comparison show the DEMs to be effectively co-registered, with mean differences on these stable areas to be similar in magnitude to the surface uncertainty associated with gravel/cobble packing on the active riverbed (i.e., less than 10 cm). There is some indication of a systematic datum bias between 2011 and the other surveys. This difference is, however, evident principally on vegetated surfaces and is consistent with the affects by growth and differential laser penetration. Such effects are less likely to confound comparisons on the unvegetated riverbed. **Given these results, no vertical corrections were applied to the independent surveys.**

If we assume that the mean datum difference for the surveys is zero, the pooled standard deviations of differences provide an appropriate indicator of DEM uncertainty (precision) about the mean. The pooled SD for the yearly comparisons ranges between 0.039 m to 0.092 m (for 2011-2019), similar to the pooled SD of all years under differing land covers, 0.036 m to 0.094 m. Following the uncertainty framework presented in equations 2.1 and 2.2, this difference represents the propagated uncertainty ( $\delta u_{DoD}$ ) resulting from combining DEM errors in quadrature. Following 2.2 and assuming equal contributions of uncertainty from both surfaces (i.e.,  $\delta z_{new} = \delta z_{old} = \delta z$ ) then the uncertainty ( $\delta z$ ) for an individual DEM can be estimated as:

$$\delta u_{DoD} = \sqrt{\delta z^2 + \delta z^2} = \sqrt{2\delta z^2} \quad 2.5$$

$$\delta u_{DoD} = \sqrt{2} \cdot \delta z \quad 2.6$$

$$\delta z = \frac{\delta u_{DoD}}{\sqrt{2}}$$

2.7

Applying 2.7 to the range of pooled SDs described above, suggests individual DEM uncertainties ranging from 0.028 m to 0.065 m with a 90% confidence interval of 0.06 m. **This conservative value (0.06 m) of elevation uncertainty was attributed to all DEMs as a simple, spatially uniform quantity in all following analyses.**

## 2.5 CHANNEL ADJUSTMENT ON THE REES RIVER 2011-2022

The Geomorphic Change Detection (GCD) software (<https://gcd.riverscapes.net>) was used to support the assessment of bed level adjustment by DEM differencing. This software builds on the uncertainty framework described above and discussed in more detail by Vericat et al., (2017); Wheaton et al., (2010); and Brasington et al., (2003). GCD provides a library of geospatial methods to compute DEMs of Difference (DoD) under uncertainty. The software facilitates the use of spatial masks to summarize and visualize longitudinal or regional patterns of change; multiple approaches to represent and model DEM uncertainty; tools to threshold change models probabilistically; and compute error ranges for areal, volumetric or average vertical change estimates. Data are stored within a portable 'GCD project' which incorporates self-documenting descriptions of the methods applied, graphical plots and tabular summaries, along with an enclosed database of all input and results data in generic .tif and .xml formats.

As described in 2.4 above, DEM data from four surveys are available to quantify recent channel adjustment in the lower Rees River. The three most recent surveys, 2019, 2021 and 2022 cover the active corridor from the delta to Lovers Leap (1,239,200E, 5,035,360N), representing the lower c. 14.5 km of the river. The older 2011 survey only extends over the lower 4.5 km from the delta to 1,234,485E, 5,027,080N.

Each DEM was attributed a spatially uniform vertical uncertainty of 0.06 m as discussed above. This implies a 1  $\sigma$  change detection threshold of 0.085 m. Any changes greater than this magnitude are, therefore, considered significant at the 68% confidence level. In this analysis an 84% (1.5  $\sigma$ ) confidence level is used to threshold changes, reflecting a compromise between a conventional, but conservative 95% threshold (or  $\alpha = 0.05$  significance level) and a lower, permissive 68% threshold (see discussion in 2.3 above).

Figure 13 shows an illustrative DEM of difference calculated for the epoch 2019 – 2022 for a c. 4.5 km reach of the Rees between river km 3.75 to 8.25. Areas of surface lowering or erosion are scaled in red and surface raising or sedimentation in blue. Areas below the change detection threshold are shaded as white.



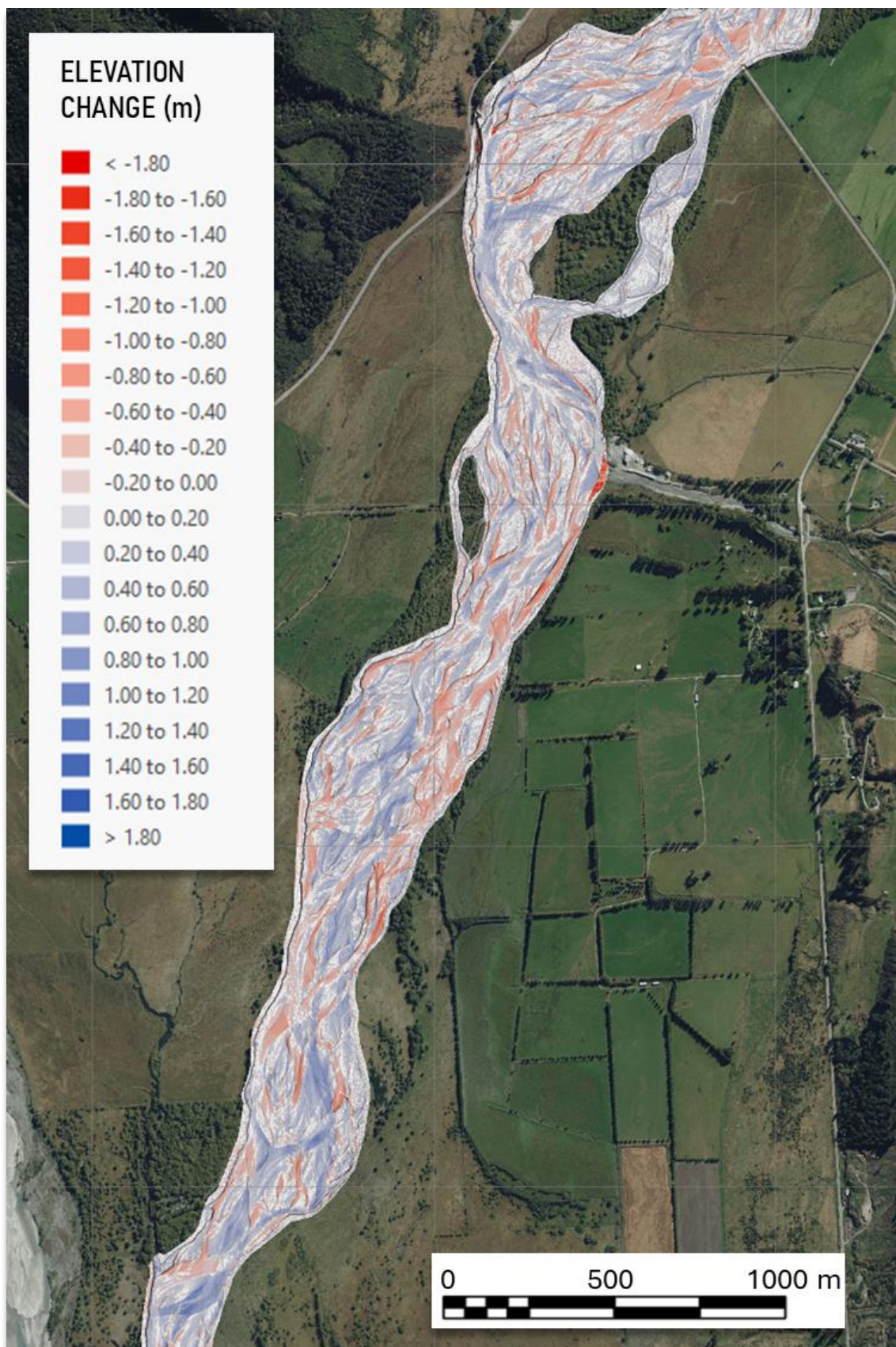


**FIGURE 13.** An illustrative DEM of Difference thresholded at the 84% CI for the Rees River (between river kms 3.75 and 8.25) for the period 2019 - 2022.

### 2.5.1 REACH-AVERAGE CHANNEL CHANGE

Estimates of areal, volumetric and vertical channel changes, integrated over the active channel width are presented in Table 5. DEM differences were computed for an Area of Interest (AOI) that encompasses the union of the active channel over the period 2011-2022 (see also Figure 15 below). The AOI extends over the lower 14.5 km of the Rees and has an average width of 337 m. Masking DoDs to the active riverbed restricts measured changes to areas where fluvial processes are most likely to be responsible for morphological adjustment. It also provides direct insights into changes in mean bed level.

It should be noted, however, that the effective AOI is also limited to the intersection of the DEMs, which vary in their spatial extent. The area over which changes are derived ranges from 976,269 m<sup>2</sup> for the 2011-2019 comparison to 4,900,426 m<sup>2</sup> for 2019-2021 (see Table 5 and Figure 11). The vertical average change presented in Table 5 normalizes this effect (where Vertical Average, m = Net Volumetric Difference, m<sup>3</sup> / Total Area of Interest, m<sup>2</sup>).

#### AREAL CHANGES

	Total Area of Surface Lowering (m <sup>2</sup> )		Total Area of Surface Raising (m <sup>2</sup> )		Total Area of Detectable Change Thresholded	Total Area of Interest (m <sup>2</sup> )	AOI % with Detectable Change
	Raw	Thresholded	Raw	Thresholded			
<b>2021 - 2022</b>	2,528,698	<b>759,748</b>	2,340,556	<b>743,832</b>	1,503,580	4,869,254	<b>31%</b>
<b>2019 - 2021</b>	1,476,997	<b>895,740</b>	3,423,429	<b>2,257,010</b>	3,152,750	4,900,426	<b>64%</b>
<b>2011 - 2019</b>	309,246	<b>193,301</b>	667,023	<b>520,814</b>	714,115	976,269	<b>73%</b>

#### VOLUMETRIC CHANGES

	Total Volume of Surface Lowering (m <sup>3</sup> )			Total Volume of Surface Raising (m <sup>3</sup> )			Total Net Volume Difference (m <sup>3</sup> )		
	Raw	Thresholded	Error	Raw	Thresholded	Error	Raw	Thresholded	Error
<b>2021 - 2022</b>	304,711	<b>242,274</b>	± 64,467	256,948	<b>196,077</b>	± 63,116	-47,763	<b>-46,197</b>	± 90,220
<b>2019 - 2021</b>	349,607	<b>318,146</b>	± 76,006	802,689	<b>726,733</b>	± 191,514	453,083	<b>408,587</b>	± 206,045
<b>2011 - 2019</b>	83,971	<b>77,406</b>	± 16,402	194,281	<b>185,300</b>	± 44,193	110,309	<b>107,894</b>	± 47,138

#### VERTICAL AVERAGES

	Average Depth of Surface Lowering (m)			Average Depth of Surface Raising (m)			AOI Average Net Thickness Difference (m)		
	Raw	Thresholded	Error	Raw	Thresholded	Error	Raw	Thresholded	Error
<b>2021 - 2022</b>	0.12	<b>0.32</b>	± 0.08	0.11	<b>0.26</b>	± 0.08	-0.01	<b>-0.01</b>	± 0.02
<b>2019 - 2021</b>	0.24	<b>0.36</b>	± 0.08	0.23	<b>0.32</b>	± 0.08	0.09	<b>0.08</b>	± 0.04
<b>2011 - 2019</b>	0.27	<b>0.40</b>	± 0.08	0.29	<b>0.36</b>	± 0.08	0.11	<b>0.11</b>	± 0.05

**TABLE 5.** Areal, volumetric and average vertical changes for the lower Rees River computed for DEM differences 2011-2019; 2019-2021; and 2021-2022, integrated over the active channel. Changes are shown both before (raw) and after thresholding at the 84% confidence interval. This analysis assumes a spatially uniform DEM uncertainty of 0.06 m for all surface models.

The data summary reveals the highly mobile character of the Rees River, with up to 78% of the AOI experiencing detectable morphological change between 2011-2019; 64% between 2019-2021 and 34% between 2021-2022.



The balance between surface raising (sedimentation) and lowering (erosion) reveals a strong signal of aggradation in the lower 4.5 km of the river between 2011 and 2019, with a net volumetric change of  $+107,894 \text{ m}^3 \pm 47,138 \text{ m}^3$ . This equates to a rise in the mean bed level over the entire active width of 0.11 m (11 cm). This pattern is also evident between 2019 and 2021, with a further net volumetric change of  $+408,587 \text{ m}^3 \pm 206,045 \text{ m}^3$ , now integrated over the wider 14.5 km AOI. Despite the short interval (776 days) this equates to a similar magnitude of surface raising of 0.08 m (8 cm) implying an increase in the effective rate of aggradation over this period. This signal of change is reversed between 2021-2022, with a net volumetric balance of  $-46,197 \text{ m}^3 \pm 90,220 \text{ m}^3$ , or an average vertical change of -0.01 m (1 cm).

Comparison of the changes in each epoch must be considered carefully due to variations in the time elapsed. Ultimately, however, the observed responses reflect variations in the driving flow and sediment supply conditions between the survey dates. The lack of continuous flow data for the Rees makes linking these changes to the history of high flow events challenging. It is noteworthy, however, that the period between 2019-2021 brackets a major flood on the 4<sup>th</sup> February 2020. This event had a reconstructed peak discharge of  $642 \text{ m}^3 \text{ s}^{-1}$  at the Glenorchy-Paradise Road Bridge, representing an Annual Exceedance Probability of c. 0.05 or 1 in 20 (after Mohssen, 2021; see also LRS, 2022). In the absence of relevant historic flow data, the discharge record for the Dart River provides a useful, though not entirely reliable proxy, shedding some insight into flood frequency and magnitude over this period. Figure 14 reveals the DoD epochs relative to this flow record.

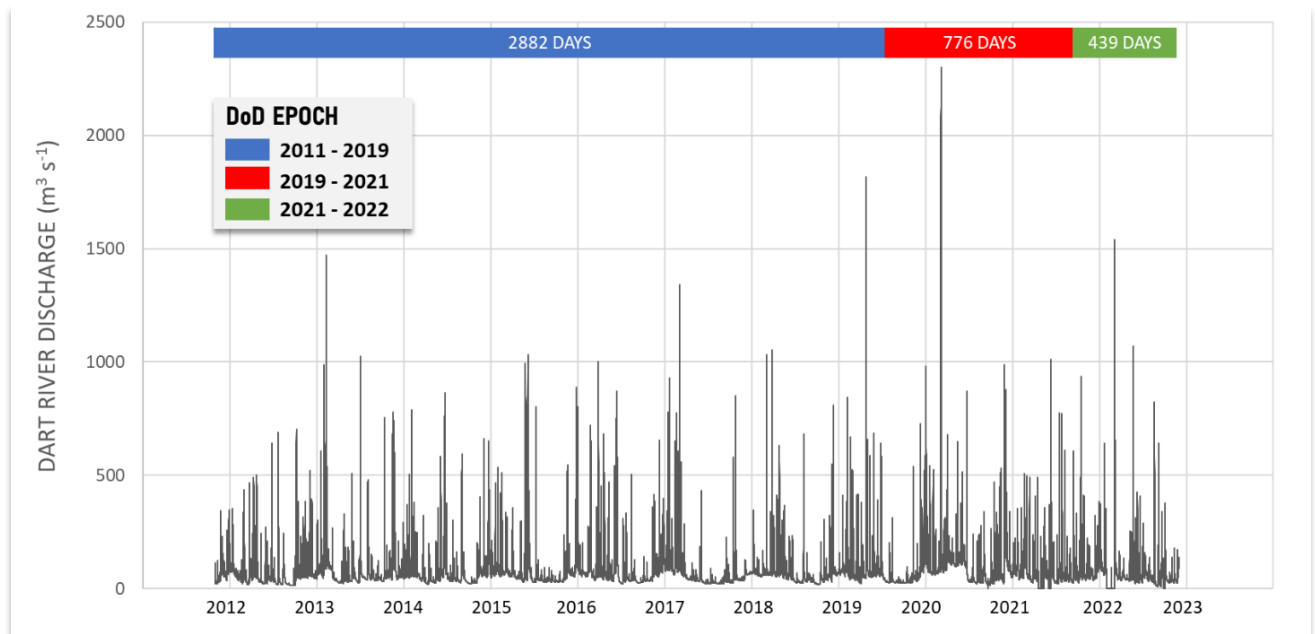


**FIGURE 14.** Hourly maximum river discharge on the Dart River at the Hillocks between October 2011 and November 2022. The DEM difference change epochs over this period are visualized by the coloured bars above the flow series.

Table 6 shows the rates of volumetric and vertical change derived by dividing by the number of days between surveys: 2011-2019 = 2882 days; 2019-2021 = 776 days; and 2021-2022 = 439 days.

VOLUMETRIC CHANGES (per day)

	Total Volume of Surface Lowering (m³)			Total Volume of Surface Raising (m³)			Total Net Volume Difference (m³)		
	Raw	Thresholded	Error	Raw	Thresholded	Error	Raw	Thresholded	Error
2021 - 2022	694	552	± 15	585	447	± 144	-109	-105	± 145
2019 - 2021	451	410	± 98	1,034	937	± 247	584	527	± 266
2011 - 2019	29	27	± 6	67	64	± 15	38	37	± 16

VERTICAL AVERAGES (per day)

	Average Depth of Surface Lowering (m)			Average Depth of Surface Raising (m)			AOI Average Net Thickness Difference (m)		
	Raw	Thresholded	Error	Raw	Thresholded	Error	Raw	Thresholded	Error
2021 - 2022	0.00014	0.00011	± 0.0000	0.00012	0.00009	± 0.0000	-0.00002	-0.00002	± 0.0000
2019 - 2021	0.00009	0.00008	± 0.0000	0.00021	0.00019	± 0.0000	0.00012	0.00011	± 0.0001
2011 - 2019	0.00003	0.00003	± 0.0000	0.00007	0.00007	± 0.0000	0.00004	0.00004	± 0.0000

**TABLE 6.** Rates of volumetric and vertical average change for each of the change epochs, calculated per day.

These data highlight the role of the February 2020 flood. The net vertical rate of change between 2019-2021 is an order of magnitude higher than the surrounding epochs due to a doubling in the rate of sedimentation relative to 2021-2022 and a fall in the relative rate of erosion. This suggests that this piedmont reach of the Rees acted as a sediment ‘sink’ during this event, sequestering material supplied from the upstream catchment. During the less flood rich period 2021 – 2022, smaller events remobilize this stored material and the active channel shifts from being a sink to a source of sediment, albeit with a lower net rate of transfer.

The longer integration period, 2011-2019 will be affected by a greater number of compensating changes, cycles of cut and fill that result in a net elevation change of zero. The observed volumes of change are, therefore, likely to underestimate the total sediment transfer significantly; a pattern that increases with the time elapsed between surveys (see Lindsay and Ashmore, 2002). Nonetheless, the strong aggradational trend in the lower 4.5 km is robust, with the rate of sedimentation roughly double the rate of lowering.

These results are consistent with the cross-section surveys discussed in 2.2 and the superelevated character of the river revealed by the REM shown in Figure 9. In the lower 4.5 km of the Rees, the DEM differences can be integrated over the full 11 year period (see later discussion). This reveals a mean bed level adjustment of > +10 cm widely and as high as >+25 cm locally. In the absence of lateral confining margins (i.e., natural levees or anthropogenic embankments) this vertical adjustment creates an increasingly unstable channel morphology, accentuating the potential for a major channel avulsion.

The results also hint at an important alteration in the future dynamics of bed level adjustment. The latest regional climate change projections (NIWA, 2019) suggest a likely increase in the frequency of high magnitude flood events for this region of western Otago. The DoDs suggest that this climate shift may accelerate the current rate of aggradation, as elevated upstream sediment supply during large events will be sequestered in this piedmont sediment sink. This may be further compounded by a reduction in the inter-arrival time between such events, limiting the scope for this material to be reworked from the sediment store during

smaller floods. This behaviour will ultimately enhance the likelihood of a major channel realignment as the superelevated channel corridor becomes increasingly unstable.

### 2.5.2 LONGITUDINAL CHANNEL CHANGE

To interrogate the longitudinal pattern morphological adjustment, the AOI was split into a set of 500 m long, contiguous cells as shown in Figure 15. These cells were used to segment the DoD and summarize the mean average bed level and volumetric changes in a streamwise direction. Integrating change over these large spatial units provides a robust estimate of bed level adjustment compared with traditional cross-sections.

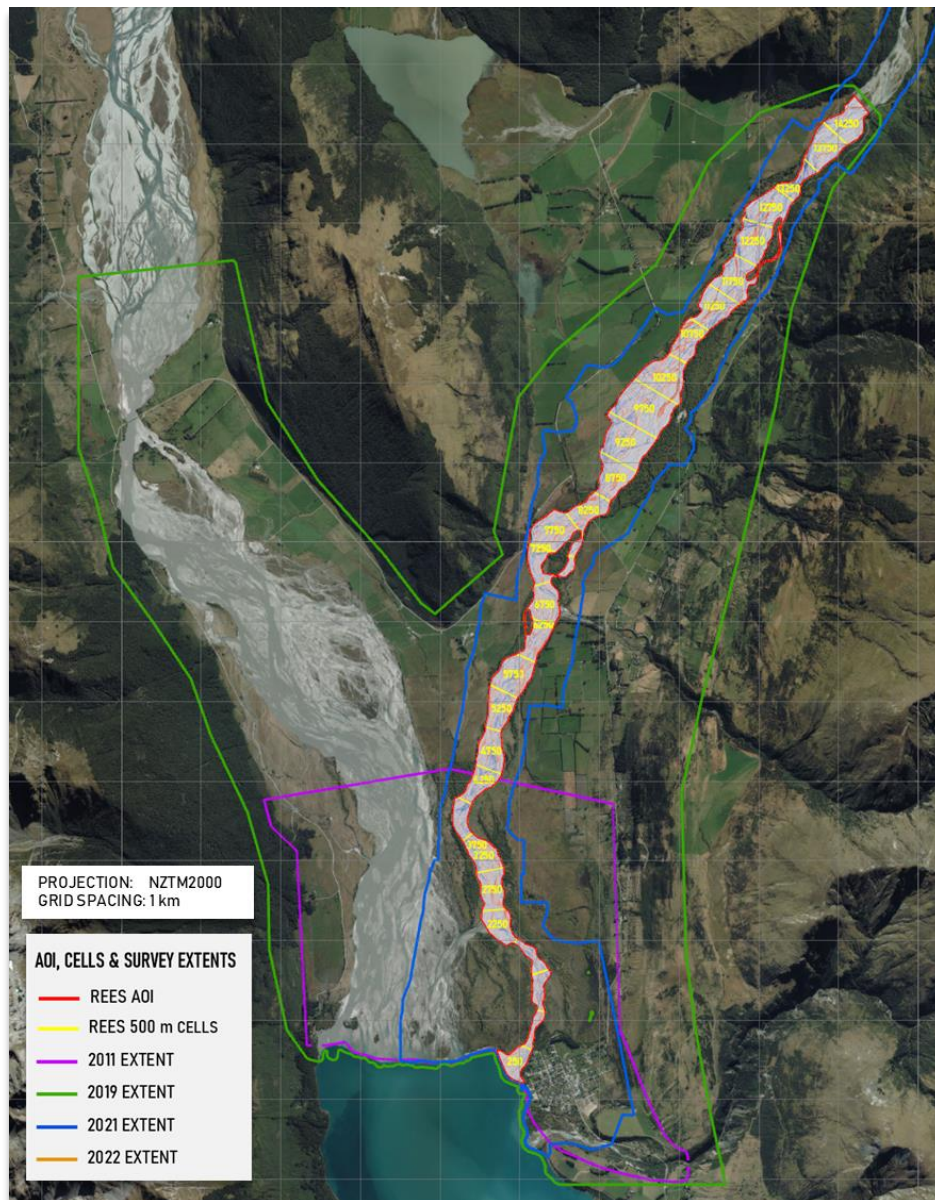


**FIGURE 15.** AOI and the 500 m scheme of discrete cells used to summarize longitudinal channel changes on the Rees River. Distances plotted represent the cell centroid, measured from the delta front. The extent of the 2011, 2019, 2021 and 2022 surveys is shown for reference.

The pattern of volumetric changes over the three epochs is shown in Figure 16. For each 500 m cell, the volume of surface raising and lowering is plotted together with the estimated volumetric error based on the

84% CI threshold. The x and y-axis for each subplot are scaled to enable simple cross-comparison. It is important to note that while the chainage between cells is constant, their area varies with the channel width. To account for this variation, the average vertical change for each of the 500 m cells is plotted in Figure 17. Figure 16 therefore provides insight into the volumes of material stored and eroded in each cell, while the net balance of these two terms determines the change in mean bed level that is represented in Figure 17. A spatial map of these changes is further presented in Figure 18, which shows the longitudinal pattern of mean bed level adjustment (integrated for each cell); this highlights the connection between Figures 16 and 17.

As discussed in 2.5.1., the three epochs of change exhibit differing reach-averaged patterns of adjustment. Between 2011-2019, the smaller 4.5 km lower reach is dominated by a strong aggradational signal, with the mean bed level rising an average of 0.08 m over the c. 8 year period. This rate of aggradation accelerates over the flood dominated period 2019-2021, before switching closer to an equilibrium with a minor degradational tendency between 2021-2022. Figures 16-18 reveal that these are system wide trends, and while there are focal points of adjustment, the temporal trends are broadly coherent across the AOI.

#### 2011-2019

Between 2011-2019, while the whole 4.5 km aggrades, with the greatest accumulation of sediment between river kms 2 - 3 where mean bed level rises by 0.17 - 0.21 m. This reach is characterized by a major bifurcation where the Rees divides into western (true right) and eastern (true left) branches. An increased rate of sedimentation at this point likely reflects a localized reduction in stream power as the river widens and the flow shallows. In the main eastern branch downstream of diffluence, the active channel width narrows and the long-term behaviour appears to be closer to equilibrium with a comparatively stable section. In the final 1.5 km towards the delta, mean bed levels again rise and (while not visible in this analysis) the delta progrades.

This sequence is visualized in Figure 19, which shows cross-sections extracted from the 2011 and 2019 DEMs at the boundary of the 500 m cells. Eight sets of sections are plotted, spanning the 0.5 km to 4.0 km chainage. These illustrate the coherent pattern of aggradation above and below the diffluence. These sections also reveal the diminishing freeboard on the true left, with the channel effectively unconfined on the left bank at sections 1.5 km, 2.5 km and 4 km. This loss of freeboard increases the likelihood of overbank flooding and local observations along with satellite imagery recorded a significant outbreak at river 1.5 km during the February 2020 flood. These areas are also identified as important breach points in recent 2D hydrodynamic modelling commissioned by the ORC (see LRS, 2022 and Damwatch, 2023).

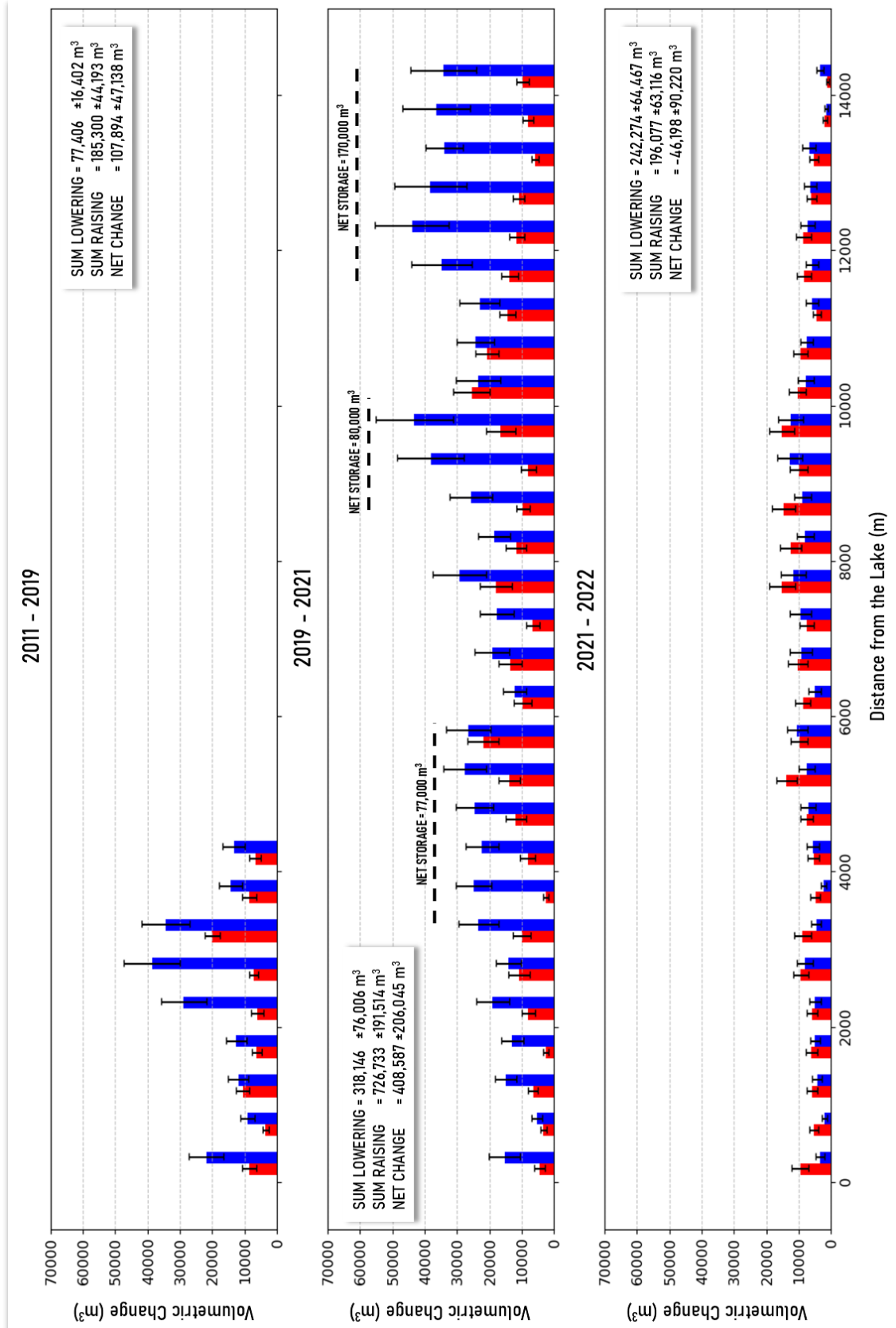


**FIGURE 16.** Longitudinal patterns of volumetric channel change segmented using the 500 m scheme of cells. All changes and associated error bars are based on a level of detection defined by the 84% CI. Key zones of sediment storage during the flood-dominated 2019-2021 epoch are highlight, which together represent >80% net storage.



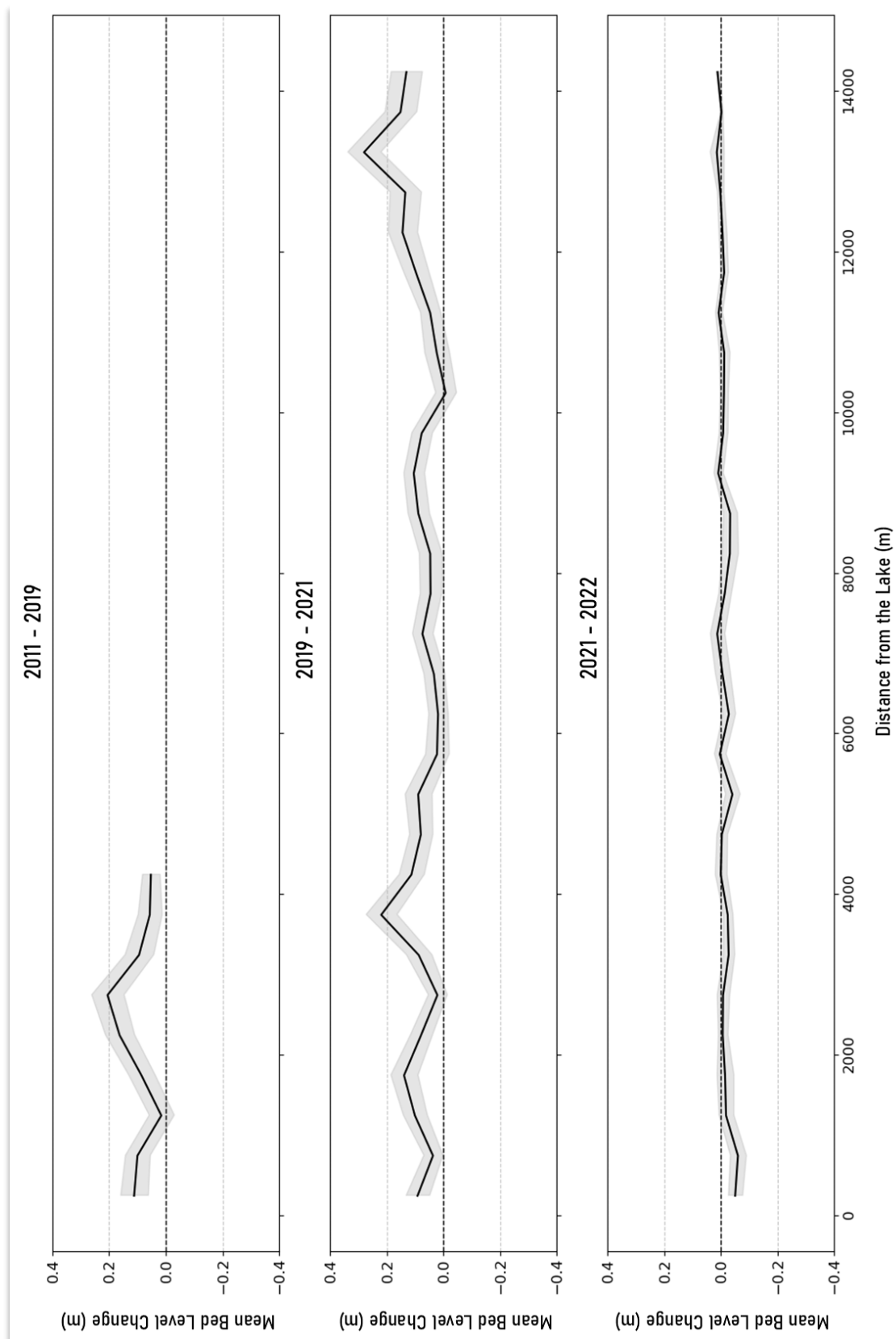


**FIGURE 17.** Longitudinal patterns of mean bed level change based on the continuous array of 500 m cells. The grey envelope represent the uncertainty associated with thresholding at the 84% confidence interval.



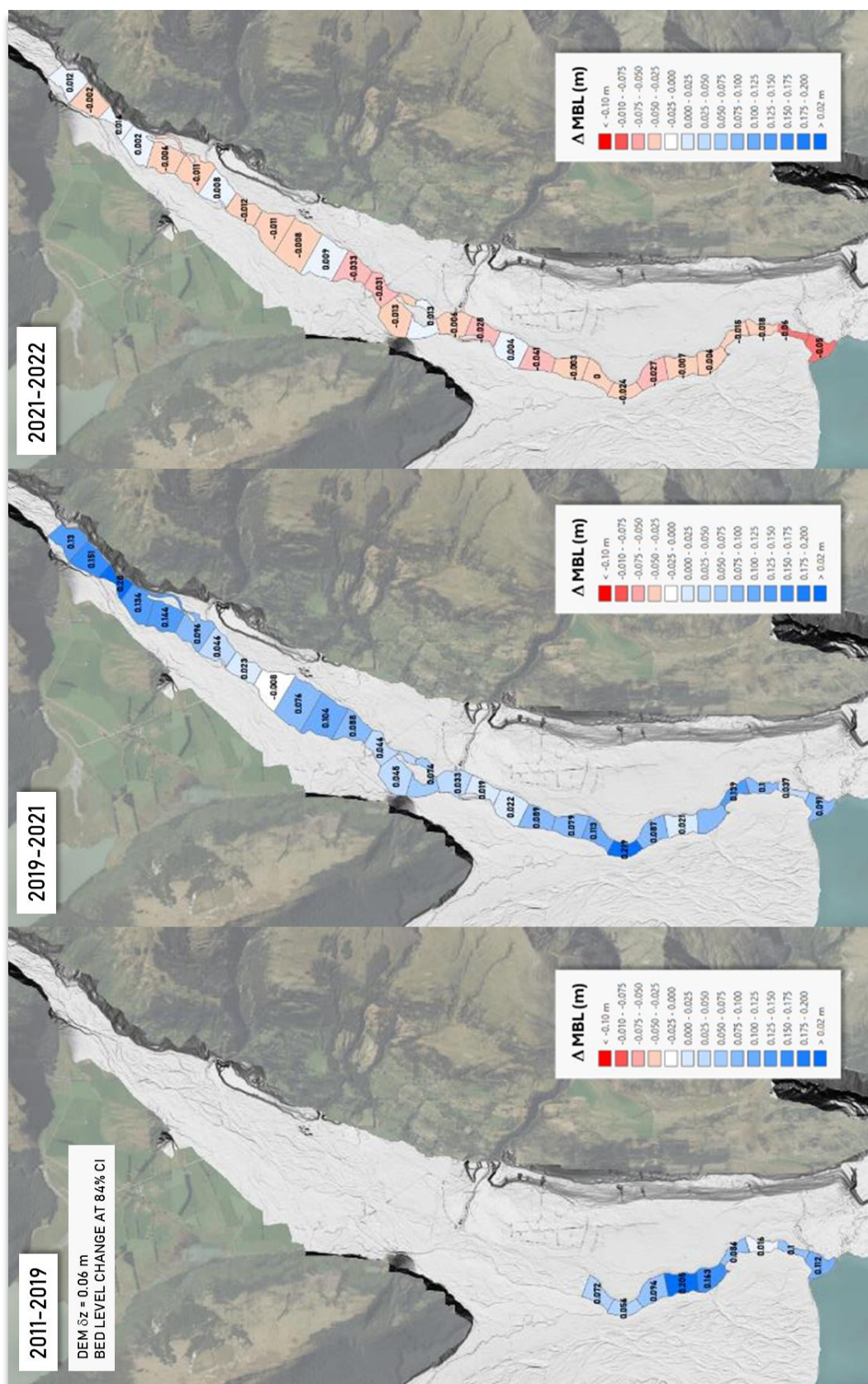


**FIGURE 18.** Longitudinal maps of the pattern of mean bed level change as defined by the 500 m streamwise cells. Positive (aggradation) is mapped in shades of blue, while negative changes (degradation) are coded in shades of red. All changes are thresholded at the 84% CI. The labels represent the estimated change bed level (m) for each cell.

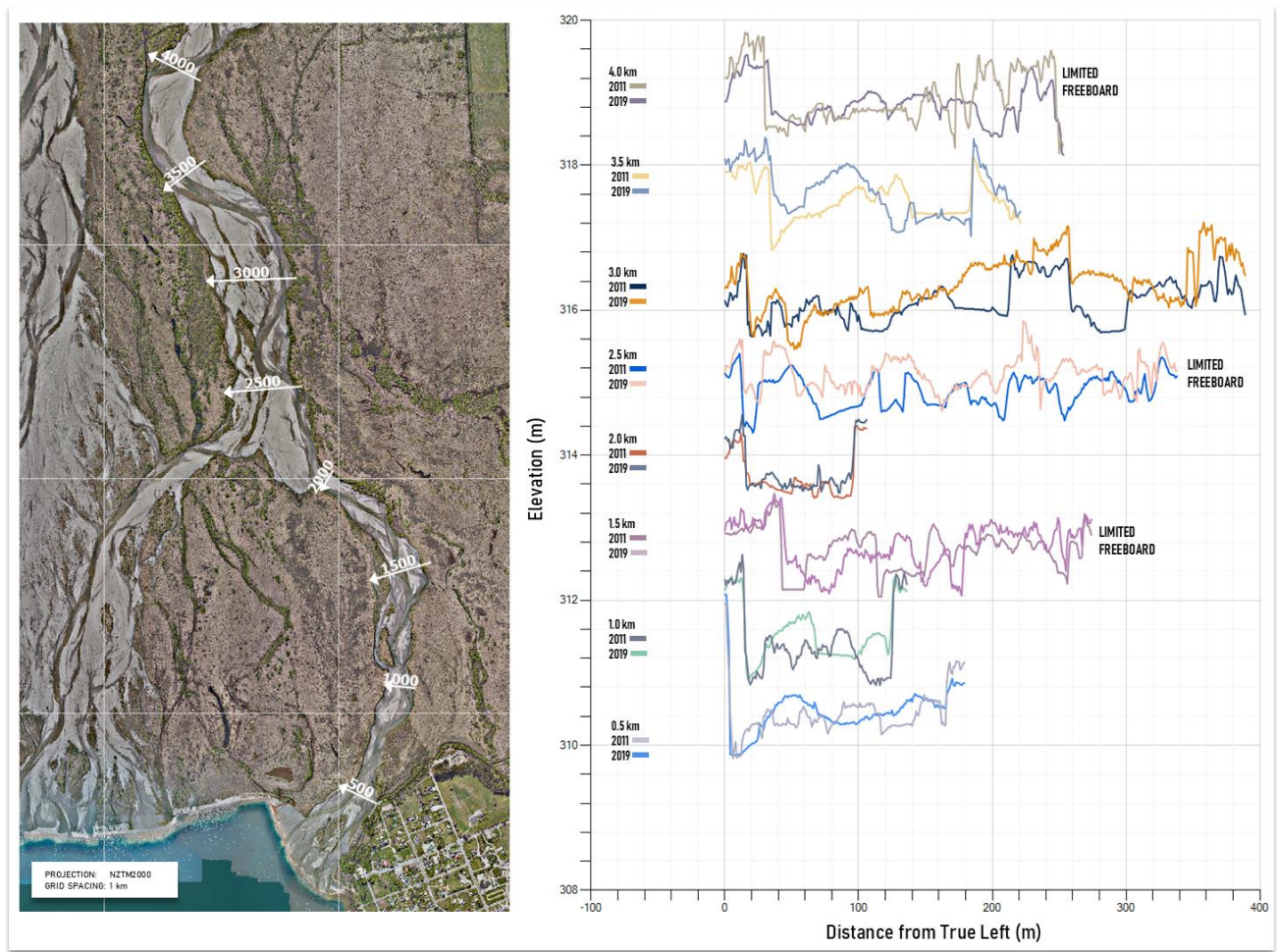


**FIGURE 19.** 500 m sections extracted from the 2011 and 2019 DEMs in the lower 4 km of the Rees reveal the longitudinal pattern of aggradation (see also Figure 18). The inset map shows the location of sections. The limited freeboard on the true left at river 1.5, 2.5 and 4 kms is highlighted and these represent important potential breach points and appear to link to pre-existing floodplain drainage as shown on the inset aerial image.

The extent of the 2011 lidar limits any long-term insights into the longitudinal pattern of the adjustment across the full piedmont reach. A shorter-term picture is afforded by the comparisons between the 2019-2021 and 2021-2022 DEMs. These again show system-wide coherent patterns that flip from aggradation during the flood-dominated 2019-2021 epoch, to marginally degradational during the following year, 2021-2022.

#### 2019-2021

During 2019-2021, three key zones of sediment storage are evident in the longitudinal series shown in Figure 16: a) river kms = 3 – 6 km; 8 - 10 km; and 11.5-14.5 km. Together, these sedimentation zones account for >80% of the net sediment storage within the whole reach. Variations in active width mean that these stores translate into bed level adjustment unequally. The highest rates of bed level change occur in the upper 3 km of the reach and peak at 0.28 m between 13-13.5 km and are widely above 0.15 m in this zone. The highest rate of aggradation occurs at the historic river crossing at Lovers Leap Road (1,238,625E 5,034,685N). This is an intriguing pattern, as confinement through a river narrows would be expected to enhance depth and shear



stress and thus the rate of sediment transport; a principle used in river training to maintain an equilibrium profile. However, in circumstances where sediment supply rates are very high, narrowing has also been linked to accelerated sedimentation. A physical explanation for this is somewhat unclear but may reflect a reduction in the variance of section averaged shear stress as confinement reduces the number of confluences that play a critical role as hotspots of shear stress and sediment flux (see Davis and McSaveney, 2003).

Figure 20 shows the morphological adjustment that occurred at the pinch point between river km 13 – 13.5. Hillshade rendered DEMs for 2019 and 2021 reveal the bar-scale changes (likely) driven principally by the major flood event in February 2020. The upstream mid-channel bar appears to accrete laterally and prograde and in so doing, reduces the size of the true left anabranch, which is confined against the eastern valley wall. Lateral growth of this bar on the true rights causes the remaining main anabranch to migrate west causing the channel to widen until it too is confined, here by a stopbank. Downstream the confluence is likely reduced in intensity, with most of the flow now channelled through the true right anabranch. As a result, the downstream attached TR bar complex grows outwards, like a point bar, and the main thalweg aggrades.

This evolution is consistent with a high rate of sediment supply choking the channel, reducing the morphological complexity and encouraging sedimentation. While, this location poses little threat to existing assets, it does indicate the risk of using conventional river training methods to manage aggradation in a system dominated by high sediment supply events (see comments relating to the highway bridge below).

Downstream, the next major sedimentation zone is occurs at river km 8 – 10, just upstream of the Glenorchy-Paradise Bridge. Here, over 80,000 m<sup>3</sup> of sediment goes into storage. This net change implicitly incorporates the anthropic extraction of gravel in clearly defined mining operations; at the bridge (1,235,900E 5,030,380N m); and close to the gravel yard at river km 10 (1,236,900E 5,031,800N m), shown in Figure 21. Net volumes of change in the two areas represent lower bound estimates on the volume of gravel extracted (i.e., the changes could be compensated by sedimentation) and suggest the removal of at least c. 23,500 m<sup>3</sup> of sediment. Incorporating this into the net fluvial sediment budget, suggests the sequestration of gravel in this reach could be as high as 103,500 m<sup>3</sup>. (i.e., the original +80,000 m<sup>3</sup> + the further 23,500 m<sup>3</sup>).

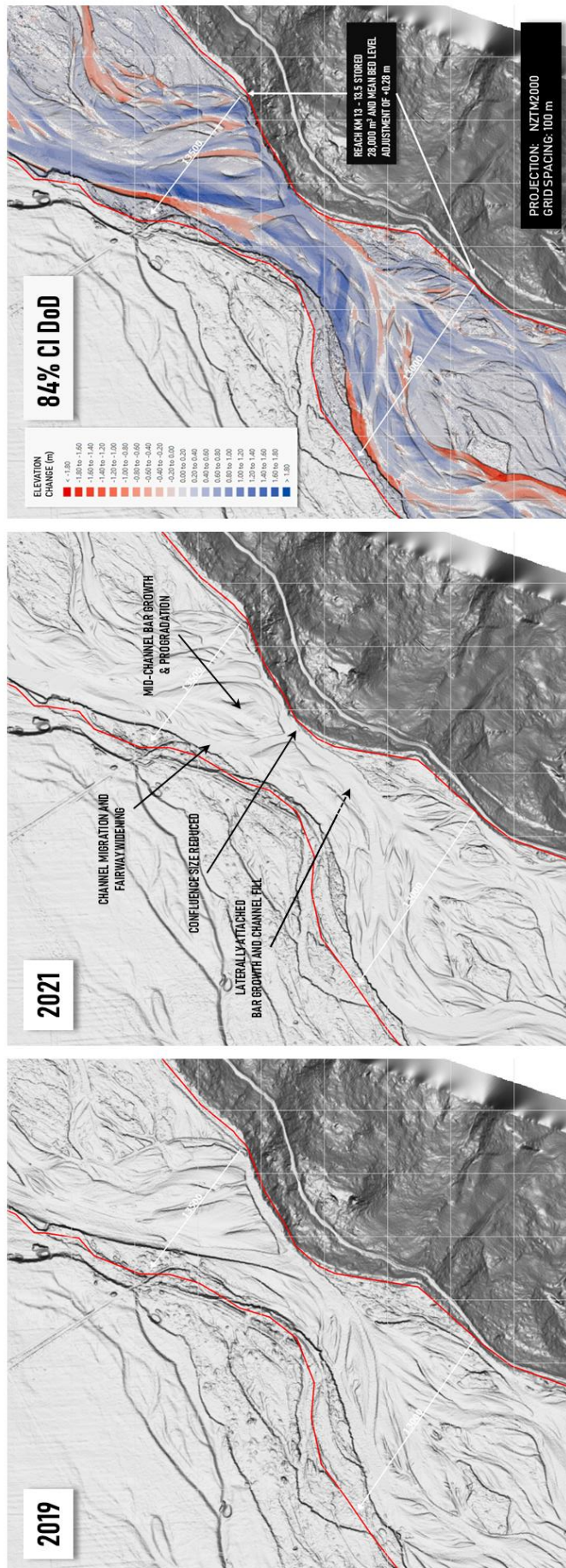


**FIGURE 20.** Morphological adjustment at the narrows between river km 13-13.5. The DEMs in 2019 and 2021 reveal lateral expansion of the upstream central bar the drives widening of the active section on the true right, while choking the true left anabranch. The intensity of the downstream confluence is reduced and the true right bar complex grows and the main thalweg aggrades. The DoD shows the cumulative impact of these changes.



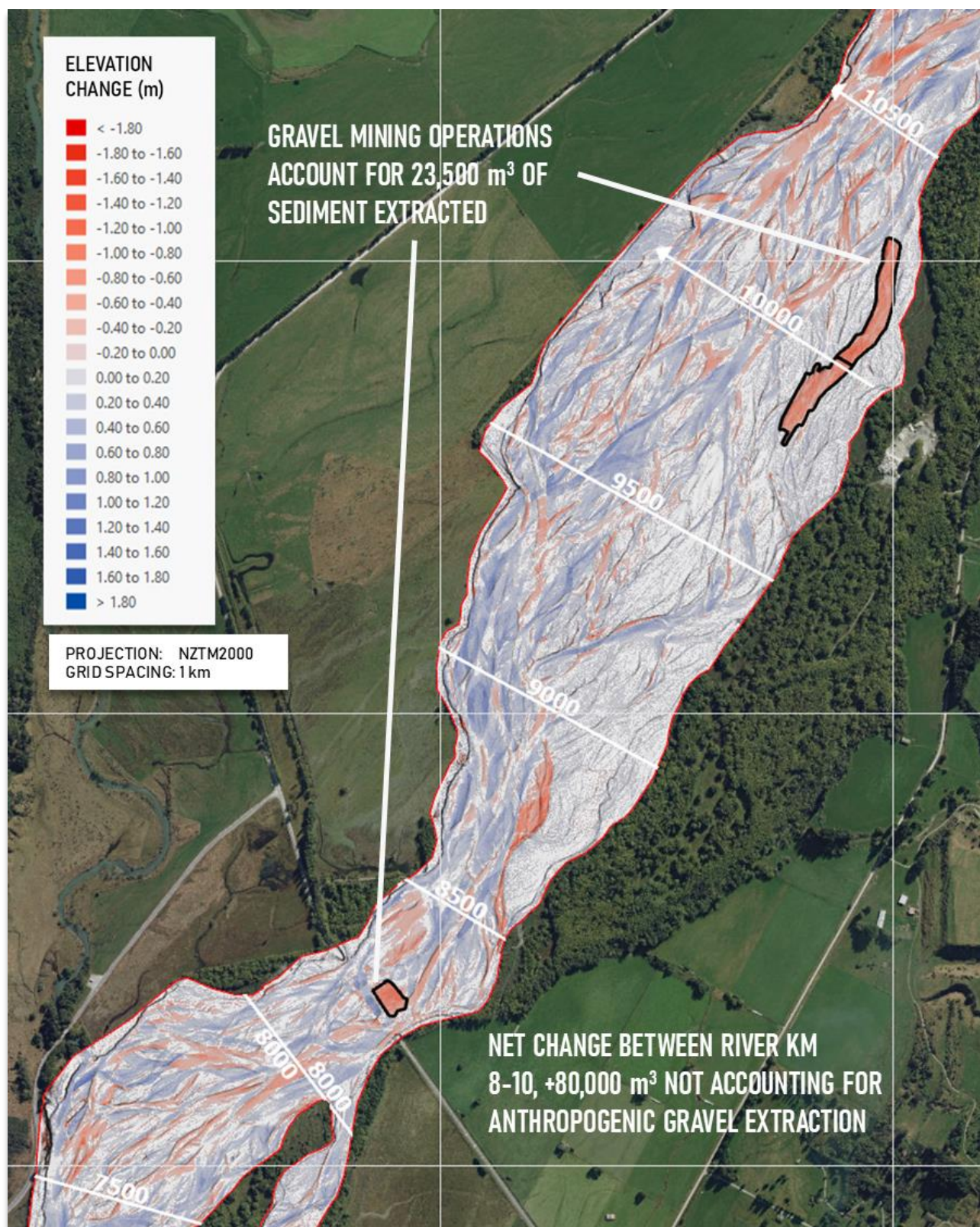


**FIGURE 21.** DEM of Difference for 2019 – 2021 for river km 8-10, revealing gravel extraction areas and high rates of sedimentation on the true right of the river and close to the Glenorchy-Paradise Bridge. All changes computed using an 84% CI threshold.



Figure 21 shows that sedimentation is focused on the true right, together with a significant volume close to the bridge at river km 8 – 9. In this sensitive location, the net change is c. +25,000 m<sup>3</sup> (after accounting for 2,300 m<sup>3</sup> of gravel extraction) resulting in mean bed level adjustment of +0.05 m below the bridge to +0.10 m upstream of the bridge (see Figure 18).

As discussed below, this is partly compensated by a net fall in bed level between 2021 and 2022, but nonetheless still represents a significant short-term rate of aggradation close to this critical infrastructure.

This finding corroborates concerns over the high rates of aggradation at the bridge. It also raises a question mark against river management strategies that aim to narrow the channel at this crossing. As reported by Damwatch (2024), the original bridge construction was designed to accommodate overflows through flood relief zones on both the true right and true left of the bridge. Post construction, a new floodbank was constructed on the true right (northern) bank, which has served to confine flows under the bridge. This artificial narrowing of the channel could – as seen at river km 13 – be partly responsible for contributing to the pattern of aggradation at the bridge.

Downstream of the bridge, another locus of sediment storage is evident between river km 3 – 6. While rates of sedimentation are high here, they are partly offset of high rates of erosion. The volume of erosion through this reach declines downstream (see Figure 17 and Figure 22 below), and the net result therefore is a very high volume of aggradation at the downstream end of this reach. Between river km 3.5 – 4.0, the bed rises by 0.22 m. Recall, this is an average rate computed for the full 500 m wide cell, not local adjustment at a section.

This very high rate of aggradation again appears to coincide with narrowing of the active channel – a pattern similar to that discussed at river km 13 – 13.5 and also at the Glenorchy-Paradise Bridge. At each of these major narrows, a similar pattern of bed response is therefore observed. In 2019-2021, this also holds for the narrows below the diffluence at river km 1.5 - 2.0. While less pronounced than the aggradation at river km 3.5 - 4.0, mean bed level here rises by 0.14 m. This location was also highlighted as a zone with limited freeboard (Figure 19) and breakout flooding was observed here in the February 2020 event.

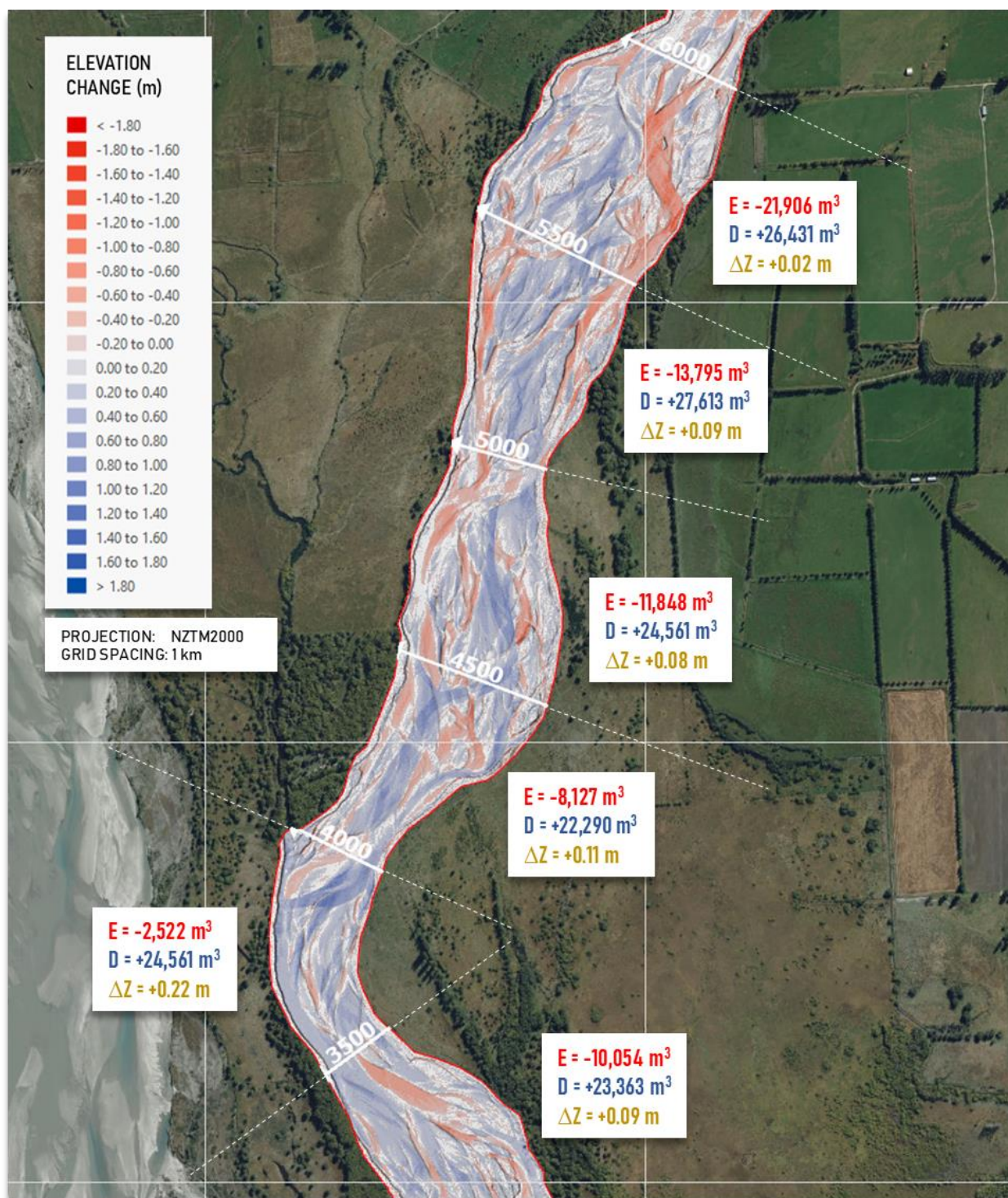


FIGURE 22. DEM of Difference 2019-2022 for river km 3 – 6. Volumes of deposition through this reach remain high but are the volume of erosion falls systematically downstream. The net consequence is an increase in mean bed throughout but, in particular, at the downstream end of the reach where the bed level rises by 0.22 m.

2021-2022

The final epoch of change represents a just over a year between August 2021 and October 2022. A partial flow record is available for this period (after December 2021) and shows only a single event with a peak discharge above  $100 \text{ m}^3\text{s}^{-1}$ . This compares to four events above this threshold in the 2023 calendar year and

six in 2024. While difficult to draw any substantive insights into event frequency, it seems reasonable to assume that this was a relative quiet period hydrologically. Unlike to two preceding epochs, this period is characterized by comparative stability and minor degradation occurring throughout the entire reach. The net result is some limited reworking of the material that went into storage in the preceding decade. There is some indication of a longitudinal trend in the rate of degradation, with incision increasing downstream.

#### INTEGRATING CHANGE 2011-2022

For the lower 4.5 km of the Rees, for which lidar data are available for the 11 years, it is possible to integrate the combined morphological adjustment over this period. Figure 23 shows bed level adjustment for each epoch together with the integrated pattern in this downstream reach. This reveals mean bed level to have risen by over +0.2 m between river kms 1.5 – 4.0 with a peak rate of aggradation of  $+0.25 \text{ m} \pm 0.06 \text{ m}$ .

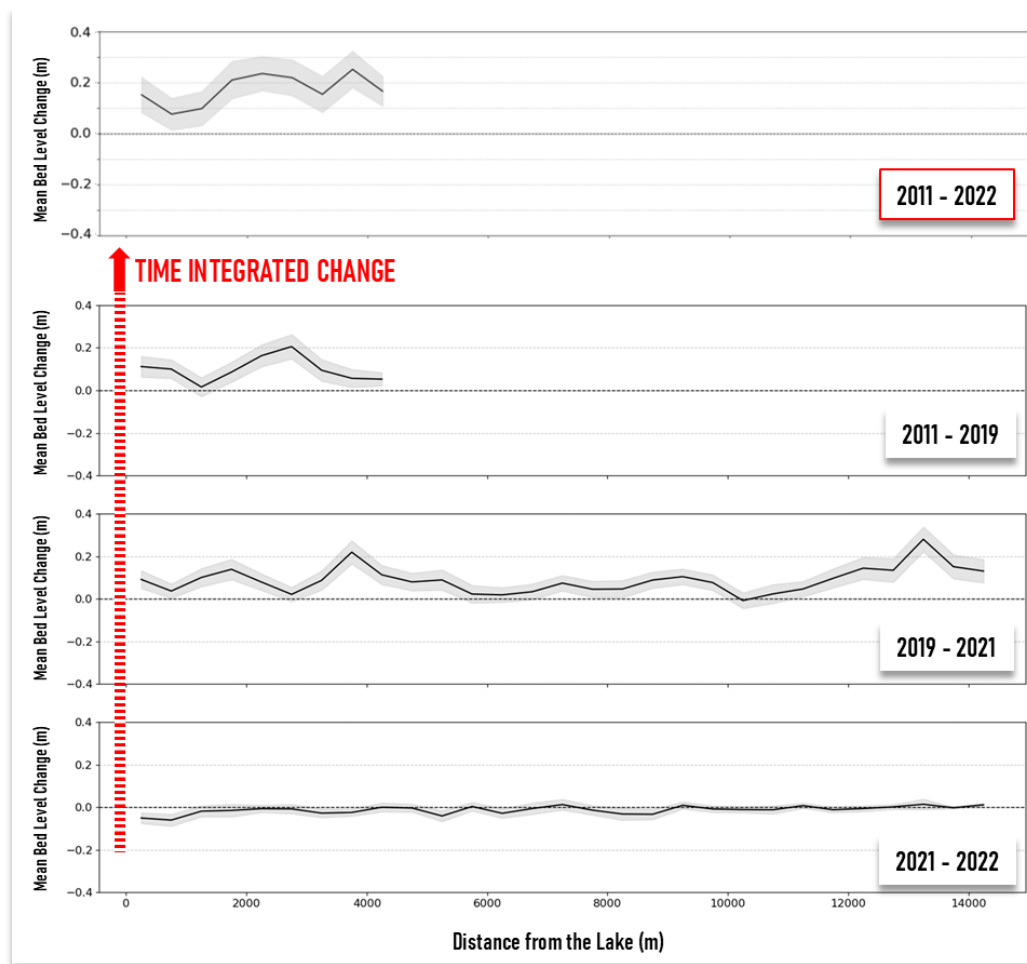


**FIGURE 23.** Integrated trend in mean bed level for the period 2011-2022 limited to the area where surveys intersect.

#### 2.5.3 A CONCEPTUAL MODEL OF MORPHODYNAMIC ADJUSTMENT

The flip-flopping of coherent, system-wide aggradation-degradation patterns is consistent with a model of river adjustment suggested in 2.5.1. This posits that sediment supply from the upstream catchment is



effectively unlimited. During large storms, significant volumes of sediment are delivered to the piedmont reach, which has insufficient transport capacity to pass this load downstream. During these events, the lower Rees is transport capacity-limited and behaves as a sediment sink and aggrades system-wide. Under such high sediment supply conditions, the rate of aggradation is maximised where the active channel narrows and morphological simplification exacerbates the reduction in transport capacity. Between major events, with comparatively limited supply from the upstream catchment, the river switches to a supply-limited state and ‘mines’ the stored material, partially compensating for the aggradation. This trajectory of riverbed adjustment is thus controlled by the frequency and magnitude of severe events, as illustrated in Figure 24.

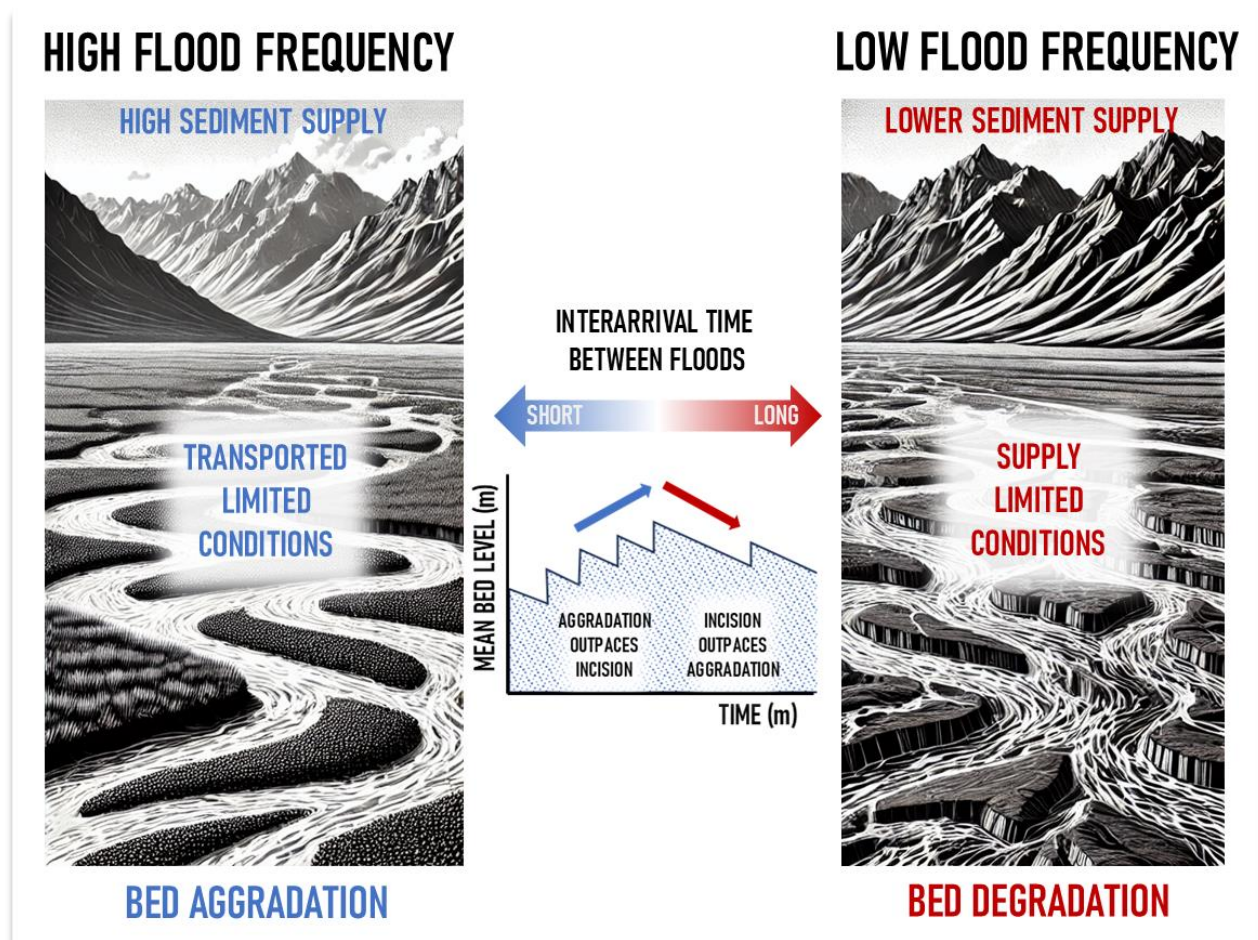


**FIGURE 24.** A conceptual model of the relationship between sediment supply, sediment transport conditions and bed adjustment. Sediment supply from upstream catchment is unlimited, so that during high flow events large volumes of material are delivered to the piedmont braidplain. The hydraulic conditions are incompetent to transport this high load and the river aggrades. In between floods, lower sediment supply from upstream enables the river to rework material the deposited and the river degrades. The long-term tendency of bed level is ultimately controlled by the interarrival time between large events.

Higher magnitude events are likely to generate stronger aggradational signals, while longer inter-arrival times between events would enable this material to be reworked downstream. However, with both the frequency and severity of events forecast to increase under climate change (NIWA, 2019), current trajectory of long-term aggradation appears likely to accelerate.

While the DEMs of Difference presented here offer only a short-term insight into typical rates of processes, the change volumes presented can be interpreted to provide lower bound estimates on sediment fluxes. For example, the net depositional signal in 2019-2021 implies a minimum input to the reach of c. 400,000 m<sup>3</sup> or c. 500,000 tons (assuming a bulk density of 1.25). While this represents changes over a two year period, this minimum flux is an order of magnitude higher than the average annual rate of sedimentation estimated by Wild et al. (2013, see 1.4). By contrast, the net DoD calculated for 2021-2022, suggests a net delivery to the delta of c. 40,000 m<sup>3</sup> (or 50,000 t), close to the annual average estimated by Wild et al. (ibid). These totals are very likely to underestimate the actual volumes of material being transported, not least because the epochs integrate multiple events that drive compensating patterns of cut of fill (see, Lindsey and Ashmore, 2002), but because the DEMs ignore changes in the subaqueous zone. While, as discussed above (section 2.3.1), these may sum to zero in terms of changes in storage, there are likely to be significant volumes of material transferred that are not quantified.



### 3. EVOLUTION OF THE DART RIVER CORRIDOR

#### 3.1 ARCHIVAL REMOTE SENSING

While the analysis of lidar-derived DEMs provides powerful insight into the fully three-dimensional nature of river morphodynamics, the availability of repeat survey data remains limited. Where multiple surveys do exist, the depth of temporal perspective they offer is narrow. Very few datasets in New Zealand (or elsewhere) stretch back to the early 2000s and where multiple epochs of data are available, they rarely span more than the last decade.

An alternative approach to quantify longer-term patterns of channel change is through the analysis of repeat aerial orthophotography or satellite imagery. These data provide only a 2D or planform perspective, but in the case of aerial photography, offer a depth of historical coverage that stretches back to the 1950s or even earlier. Open access satellite imagery dates back only to the 1970s, but data from Earth Resources Satellites such as those of the Landsat and Sentinel programmes provides multispectral information across the wider optical and thermal spectrum. These data, in the form of spectral image bands, can be used to derive spectral indices, such as the normalized difference vegetation index (NDVI; Rouse et al., 1973) and the normalized difference water index (MNDWI, Xu, 2006). Easily computed, these metrics have proved effective at differentiating fluvial landscapes and their surface cover (see Spada et al., 2018; Bothroyd et al., 2020).

In the past five years, rapid advances in digital infrastructure have led to the development of cloud-based IT platforms that offer on-demand computational processing power and access to publicly available catalogues of satellite imagery. The Google Earth Engine or GEE provides a web-based interface and scriptable APIs to access and analyze Landsat, Sentinel and other open-access image and vector data (Gorelick et al., 2017). This platform eliminates the need for users to manage their image collections; run their own local high performance computing facility; and through scalable computing, can enable truly planetary-scale analyses (e.g., Allen and Pavelsky, 2018; Bizzi and Carbonneau, 2024).

The data hosted on GEE have been pre-processed and standardized to enable their direct use without the need for the extensive corrections normally required of raw image data. These 'Analysis Ready Data' (ARD) are orthorectified, resampled and projected; radiometrically corrected to surface reflectance units; have automatic cloud and shadow identification or masking; and are supported by comprehensive metadata and quality assurance flags.

The following section describes the development of an analysis framework built on GEE that is used to classify the changing 2D form of the Dart River corridor over the last 30-50 years. The approach offers a multidecadal perspective that reveals the structure of the river corridor and the pattern and rate of its evolution. This is facilitated by the high temporal resolution afforded by the Landsat data and the scalability of analysis within

GEE. However, while the methods described here were also applied to interrogate the Rees River corridor too, the comparatively coarse spatial resolution (30 m) of the imagery limit the reliability of inferences made about changes in this smaller river system. As such, only data for the Dart River are comprehensively quantified in the following analyses.

### 3.2 AUTOMATED MAPPING OF RIVER CORRIDOR COVER WITH GEE

A simple scheme is proposed that classifies land cover in the river corridor into one of three categories: a) open water; b) exposed sediment; c) fully vegetated. For any snapshot in time, the combined area of open water (taken to be channels) and exposed sediment quantifies the area that is being reworked fluvially. The stable class, by contrast, defines the undisturbed riparian area or parts of the river corridor that have been fully colonized and stabilised by vegetation. Amalgamating the water and exposed sediment into an ‘alluvial’ class reduces any potential bias associated with transient high or low flood events, enabling a clearer focus on the ‘fluvially-active’ versus inactive areas of the river corridor.

A stepwise, automated classification workflow was built in GEE using its Python API and leveraging *geemap* (Wu, 2020) to support the analysis and visualization of results. To maximize the historical perspective, a range of Analysis Ready Data from the Landsat program, dating back to the 1980s were used. This includes 30-meter resolution imagery from the following sensors: Landsat 5 Thematic Mapper; Landsat 7 Enhanced Thematic Mapper+; and Landsat 8 Operational Land Imager. Using multiple generations of Landsat sensors offers access to a variety of spectral bands, providing reflectance information on the visible, near-infrared, shortwave infrared, and thermal infrared response. All image data are geometrically and atmospherically corrected to give units of surface reflectance and Quality Assurance (QA) bands included to identify pixels affected clouds, shadows and instrument artefacts. To minimize misclassification of pixels, only images with less than 10% cloud cover were used as input for the workflow.

Binary ‘water’ and ‘alluvial’ (i.e., wet plus exposed sediment) masks were created for each image by combining a range of spectral indices. Spectral indices are combinations of spectral bands used to highlight features in the data, such as vegetation, water content or soil. The spectral indices used include the NDVI (Normalised Difference Vegetation Index), which is used to highlight healthier and denser vegetation (Huang et al. 2021). It is a combination of the reflectance in the Near Infrared (NIR) and the Red spectral bands:

$$NDVI = \frac{NIR - RED}{NIR + RED} \quad 3.1$$

The MNDWI (Modified Normalised Difference Water Index, Zhou, et al. 2015), is used to enhance open water features while suppressing land and vegetation and is a combination of the reflectance in the shortwave infrared (SWIR) and GREEN spectral bands:

$$MNDWI = \frac{GREEN + SWIR}{GREEN - SWIR} \quad 3.2$$

The EVI (Enhanced Vegetation Index, Matsushita et al. 2007) was also used to highlight vegetation. This is an optimized version of the NDVI that improves sensitivity by reducing atmospheric influences, soil brightness and sensitivity to biomass variability. EVI is a slightly more complicated index, combining NIR, RED and BLUE spectral bands; a gain factor,  $G$ , that enhances the vegetation signal (typically set to 2.5);  $C1$  and  $C2$  aerosol resistance coefficients (typically set to 6 and 7.5 respectively); and a parameter,  $L$ , that adjusts the background influence of soil brightness (typically set to 1):

$$EVI = G \times \frac{NIR - RED}{(NIR + C1 \times RED - C2 \times BLUE + L)} \quad 3.3$$

A set of rules, leveraging these indices, was then used to attribute pixels to either the water or alluvial class. The classification of water was based on Zou et al. (2018) and defined by the condition ( $[MNDWI > NDVI]$  or  $[MNDWI > EVI \text{ and } EVI < 0.1]$ ). For the alluvial area, the approach of Boothroyd et al. (2020) was adopted, where for a pixel to be considered alluvial, the  $[MNDWI > -0.4 \text{ and } NDVI < 0.2]$ . These rules were applied, image-by-image, to a timeseries of images sampled from GEE.

Each image was processed to yield a binary mask that defines the distribution of water and alluvial areas. This mask was then placed into an image stack, corresponding to a temporal window or ‘timeslice’. Two approaches to stacking the masks were used. The first placed all masks into a single group, representing the complete analysis period, 1995-2024 (29 years). The second approach defined stacks for shorter temporal windows, each corresponding to a five-year timeslice: 1995-1999; 2000-2004; 2005-2009; 2010-2014; 2015-2019; and 2020-2024.

For each stack, corresponding pixels were analysed to determine the number of times they belonged to either the water or alluvial class. The total number was then converted into an empirical frequency, based on the total number of images in the stack, modified to account for cloud cover/shadow flags in the Quality Assurance mask. This approach enables the user to then threshold the classification at any chosen significance level and thus create maps of class membership for a given time period. A finalized classification was then obtained by applying hierarchical rules to pixels based on their class membership. Water pixels are first defined; pixels that are alluvial but not water are classed as exposed sediment; and pixels that are neither water or exposed sediment are by default assumed to be stable vegetation cover. An integrated alluvial or active channel class is also defined which represents the combined water and exposed gravel.

Once class memberships were finalized, the data were clipped to a Area of Interest (AOI) defined by the geomorphologically derived valley floor, discussed and presented in Figure 3 (Section 1.2.2). The longitudinal pattern of river character was then summarized using a network of 1 km contiguous, streamwise cells, that were used to extract metrics including a proportion of the valley floor within each cover class and variation in average active alluvial and wetted width of the corridor downstream.

The workflow is summarized graphically overleaf in Figure 25.

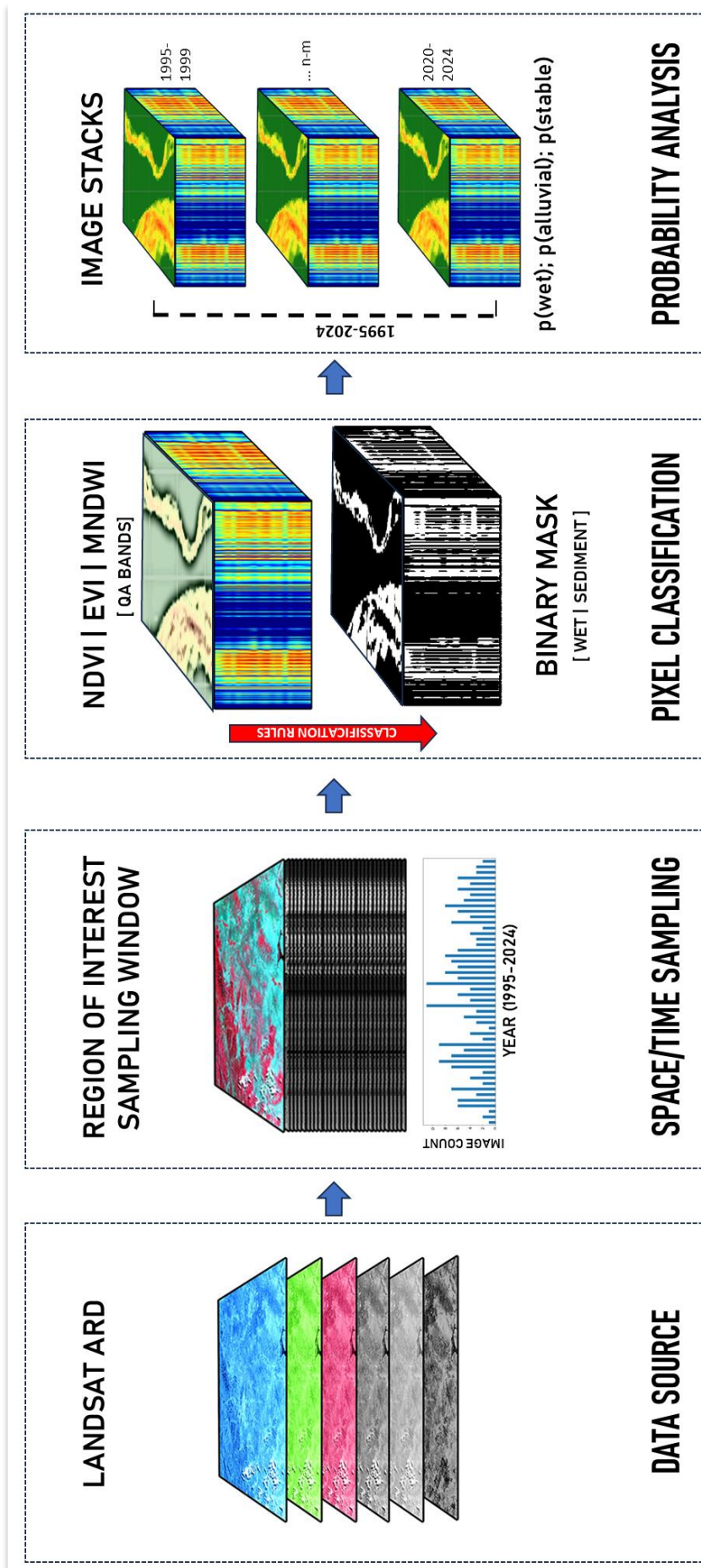


**FIGURE 25.** Schematic illustration of the workflow for probabilistic mapping of river corridor land cover. Analysis Ready Data from GEE are filtered and sorted and classified using a multi-index approach. Image stacks for multiple time windows are then analyzed statistically, and the probability of pixel membership of land cover classes determined.



### 3.3 STRUCTURE AND EVOLUTION OF THE DART RIVER CORRIDOR

A total of 160 images with less than 10% cloud cover were filtered and analyzed from the three Landsat image libraries, spanning the temporal range shown in Figure 26. As described above, these images are sourced from multiple generations of Landsat sensors, which differ in both their spectral and spatial resolution. For this analysis, all data were resampled to a consistent raster resolution of 30 m and projected into the NZTM coordinate system.

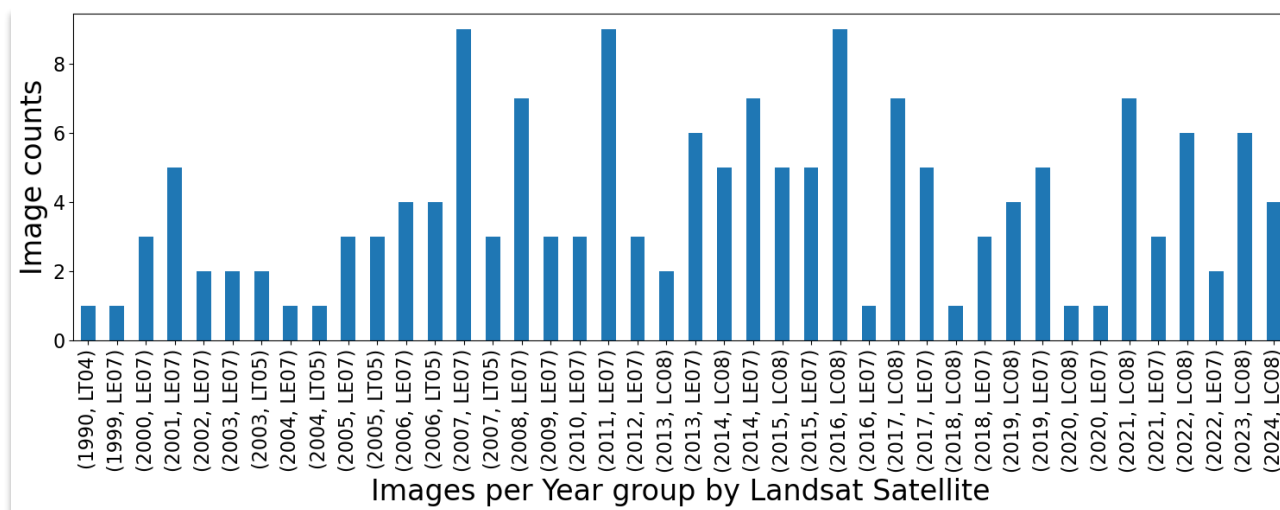


**FIGURE 26.** Number and temporal distribution of images covering the Dart River catchment accessed through Google Earth Engine. This list only includes images with less than 10% cloud cover and no significant image artefact flags.

Through the lower 25 km of the Dart, the river corridor varies from 300 - >2000 m in width, with individual anabranches between 10-100 m wide at low flow. Pixel sizes here are small relative to the dimensions of the active width and the imagery is able to characterize major anabranches. Upstream, while there are periodic widenings at valley flats (e.g., Slip Stream and Dredge Flat), the river is increasingly confined and above river km 40, is single thread and confined within a single pixel. Figures 27 and 28 show colour rendered probability models of the water and alluvial class maps for the full Dart and Rees River corridors mapped through the 29 year period. Both Figures show the probability of membership mapped for each 5 year period, and also the full 29 years. The temporal probability [0-1] is colour-rendered in shades of blue for the water class, while the alluvial class map uses a multicolour green-yellow-red rendering. These probability scores quantify the proportion of this time each pixel belonged to the class over the time period analyzed.

To aid visualization, Figure 29 and Figure 30 show maps of the dynamic reaches below Chinamans Bluff on the Dart and Lover's Leap on the Rees.

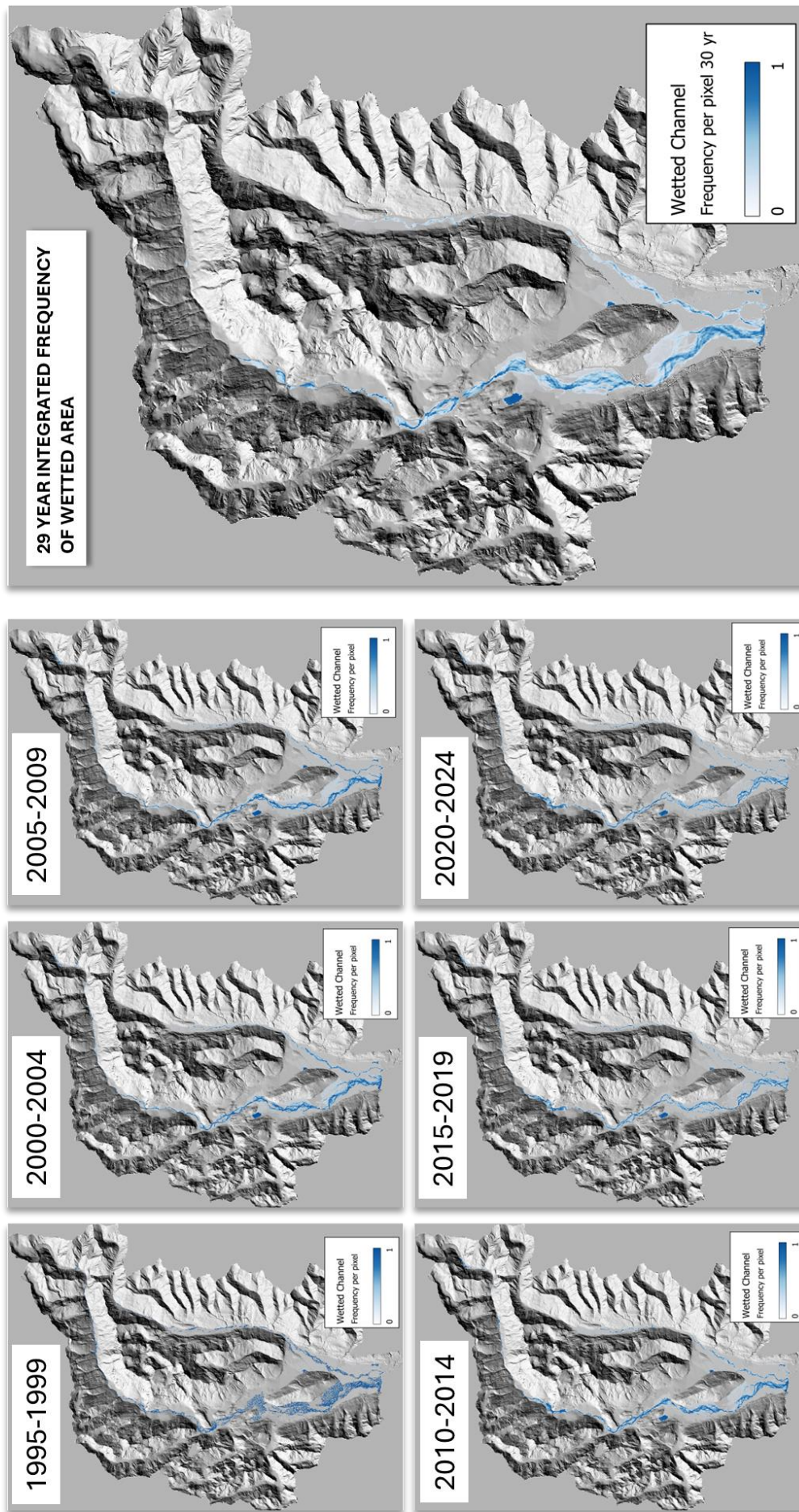


**FIGURE 27.** Probability maps revealing the distribution of 'water' pixels from 1995-2024. The small inset images show probabilities based on 5-year timeslices, while the large image shows the likelihood mapped for the full 29 year period. This pattern captures the inherent dynamism of the active anabranches of the period, giving rise the blurred patterns evident in the 29 year composite, particularly within the lower 10 km of the Dart River.



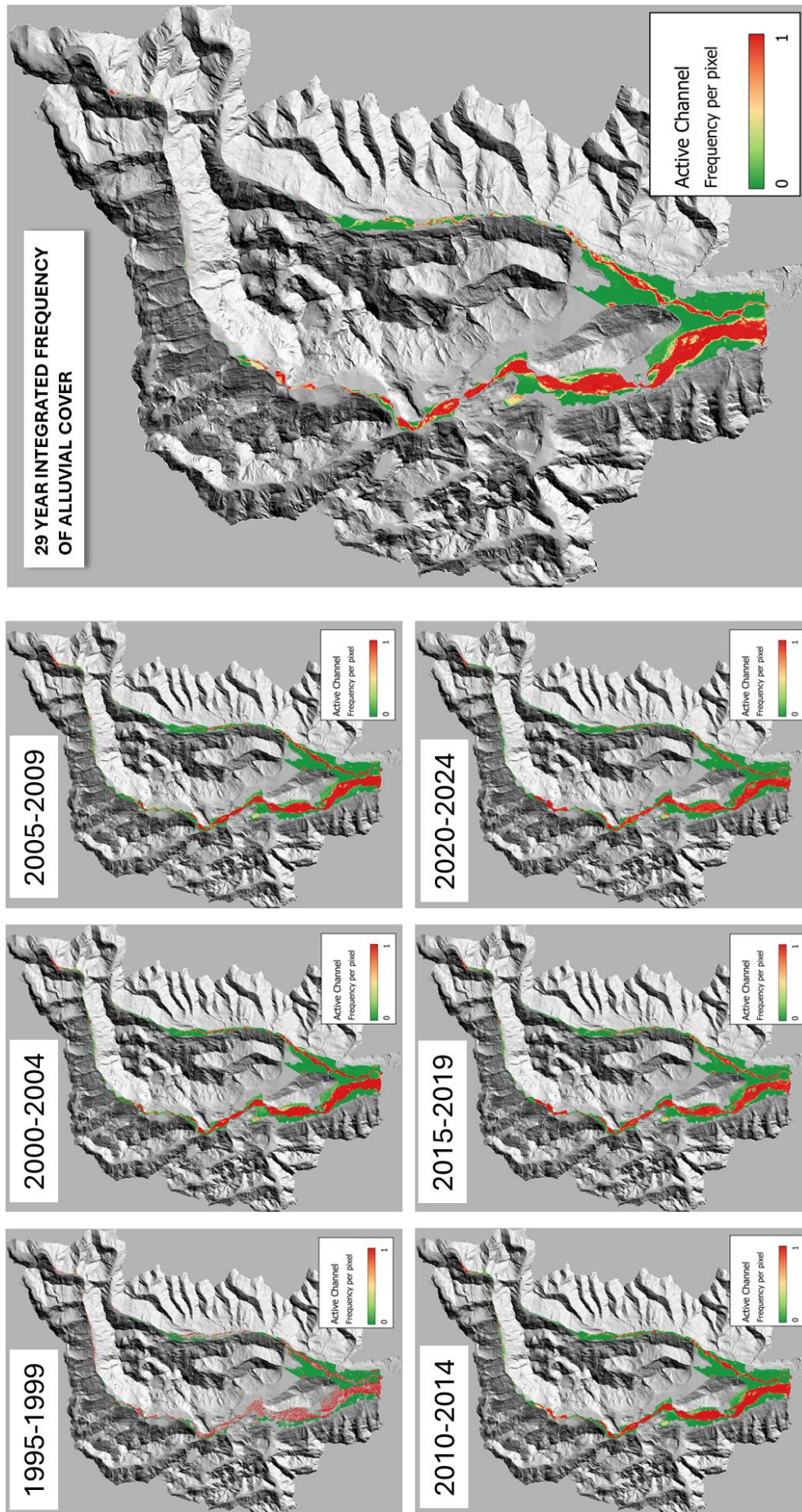


**Figure 28.** Probability maps revealing the distribution of pixels belonging to the active channel or alluvial class – comprising the wet channels and exposed sediment. Again, the small inset figures show 5 year timeslices, while the large map captures the distribution of the full 29 year record. Areas of the valley floor that are consistently active (wet or exposed sediment) appear as red, while stable areas appear green. Active margins of the braidplain are characterized by the low probability yellow areas.



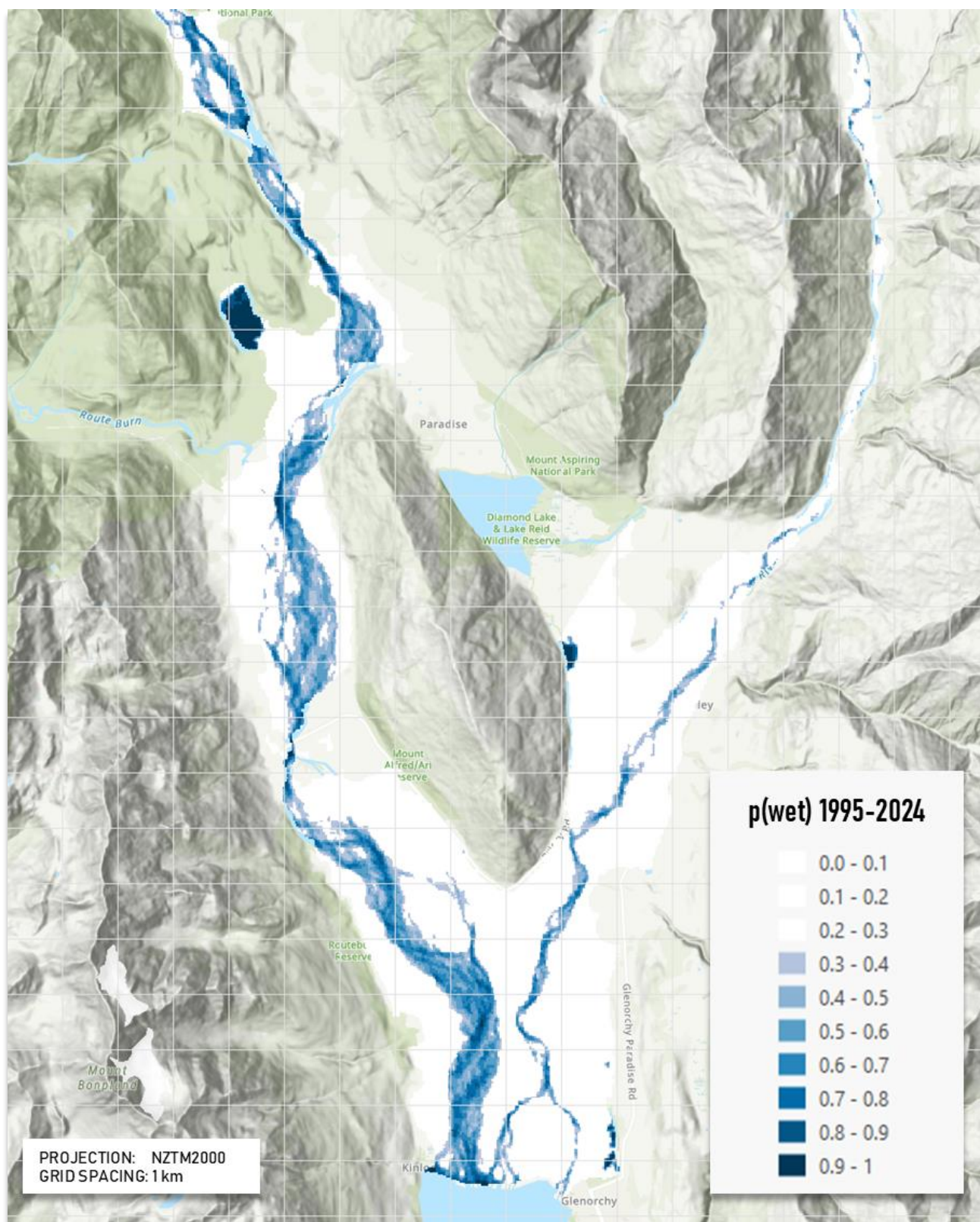


**FIGURE 29.** Probability map for the water class for the lower Dart and Rees Rivers. Probabilities are scaled in 0.1 intervals. Dart blues reveal stable areas of the anabranch network.

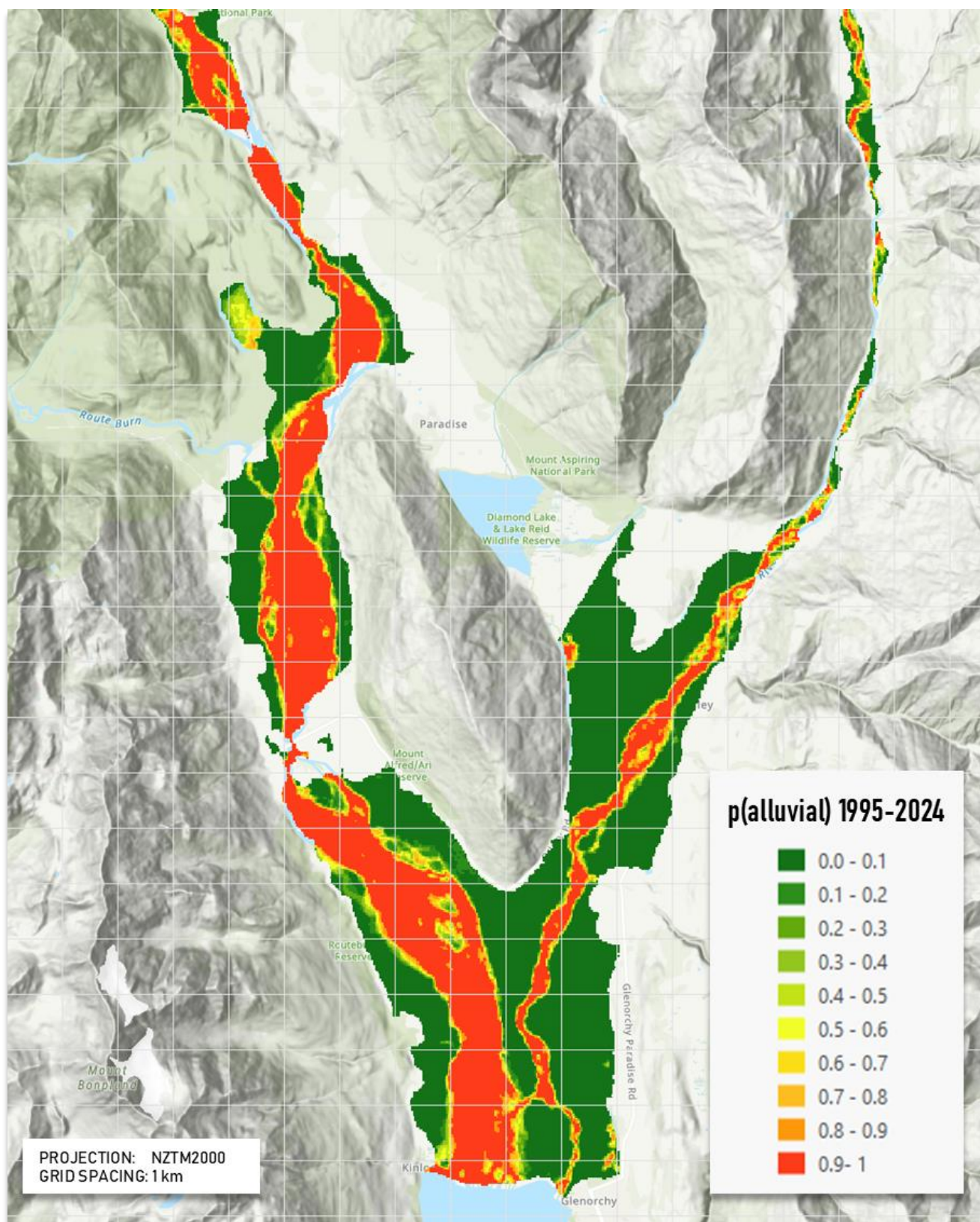


**FIGURE 30.** Probability map for the alluvial or active channel class for the lower Dart and Rees Rivers. Probabilities are scaled in 0.1 intervals. Stable areas of the valley appear in green, while the core active channel is red. Areas associated with migration of the active channel over the last 30 years is shown in shades of yellow.



Figure 30 shows the spatial probability distribution of the alluvial cover class for the entire 29 year sampling period. The high probability values ( $p > 0.9$ ) delimit the persistent braided river corridor where frequent fluvial disturbance and bed turnover suppress vegetation growth. Around the margins of this, a 'halo' of yellow and orange shades reflects a lower probability of alluvial cover and this represents the dynamic margins of the river. In most places, this halo is evident on both sides of the active channel. This pattern depicts either: a) expansion or contraction of the active width; or b) lateral migration of the channel with compensating changes on opposing sides.

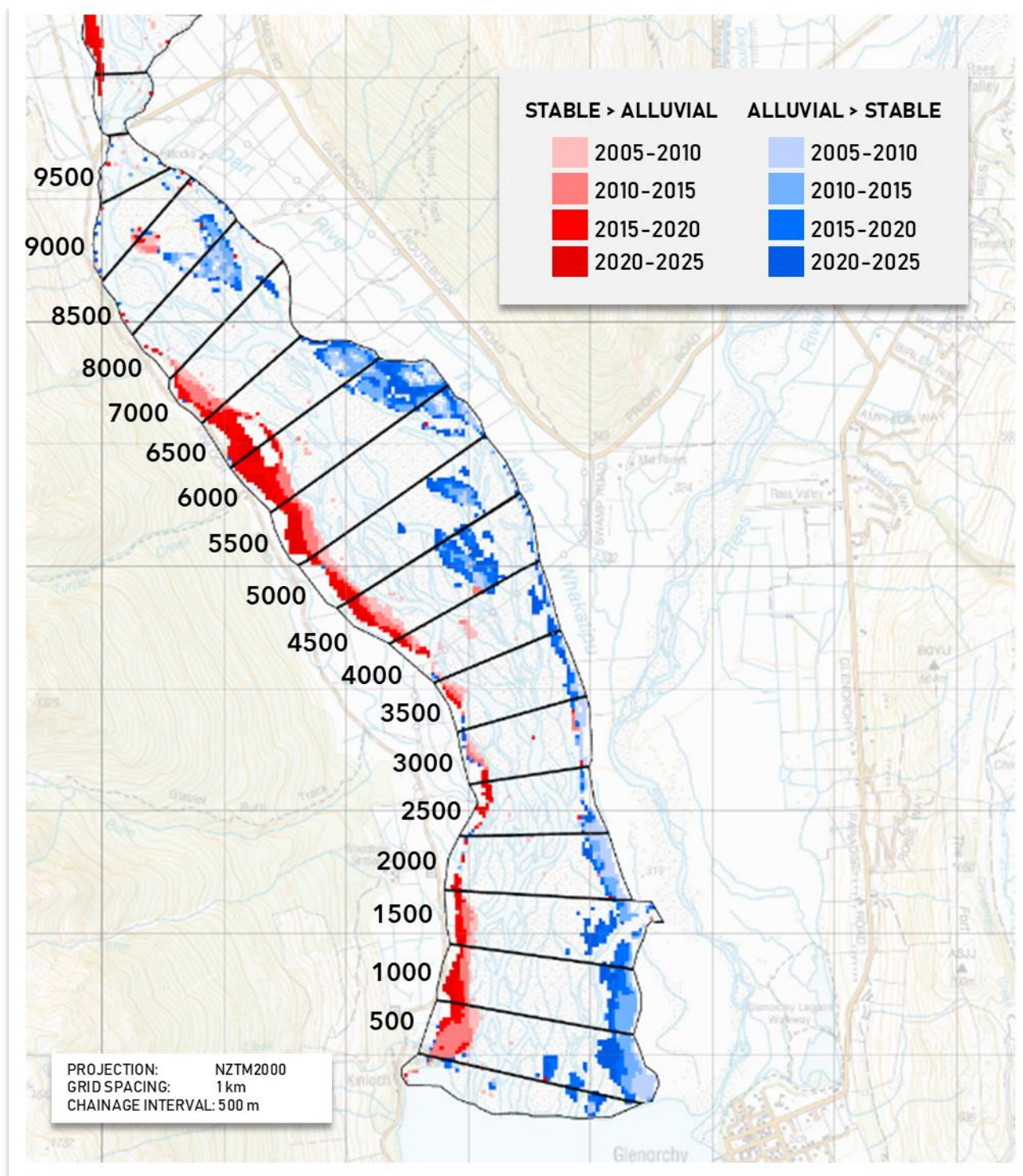
These processes can be disentangled by interrogating the 5-year timeseries (Figure 28) and computing the vector of change in class cover on a pixel-by-pixel basis. For example, lateral migration without significant widening involves in the bank erosion on one side of the channel and vegetative recovery on the other. In this situation, bank erosion is represented by the conversion of stable to alluvial cover classes; while bed stabilization involves the conversion of the alluvial to stable cover classes.

Figure 31 shows the spatial distribution of these class changes for the lower Dart River computed in 5-year timesteps from 2005-2025. This reveals a rapid westward – true left to true right - migration of the river corridor through this period. To quantify the rate and longitudinal distribution of these changes, this reach was segmented into a network of contiguous 500 m 'cells' and the area of 'erosion' and 'recovery' computed for each unit. The resulting area was then converted into an average linear rate of erosion and recovery by dividing the area by the length of each cell (500 m). The longitudinal distribution of erosion and recovery are plotted in Figure 32, where A and B show each 5 year interval and C and D show the total accumulated change.

The peak rate of channel migration is focused at two locations upstream from the delta front: 0 – 2 km; and 4-7 km. Westward migration downstream peaked between 2010-2015 with the active corridor migrating over 160 m during this period. Since then, the rates of adjustment have slowed, but still average  $> 10$  m/yr.

Upstream, the pattern of adjustment reflects redirection of the flow at the head of the fan complex described in Section 2.1 and Figure 9. Here, rapid migration was facilitated by outflanking an existing stopbank between Turners and Kowhai Creek (1,230,630E, 5,029,390N m) in 2016. This led to rapid bank retreat that is continuing at an average annual rate of c. 20 m/yr and is actively undermining the Kinloch-Hillocks Road.

Throughout the reach, the total area of bank erosion (1,292,312 m<sup>2</sup>) is less than the area 'recovering' (1,764,102 m<sup>2</sup>). This implies a marginal net average contraction of the active width of c. 50 m over through these lower 10 km over the last 20 years.



**FIGURE 31.** Westward migration of the Dart River corridor from 2005-2025 mapped in 5-year intervals. Areas of erosion on the right bank are shown in shades of red and are matched by recovery and stabilization of the channel bed, shown in shades of blue on the true left. Areas of change are computed for the 500 m cells shown (labels are chainage from the delta) and plotted as average linear changes in **Figure 32**.

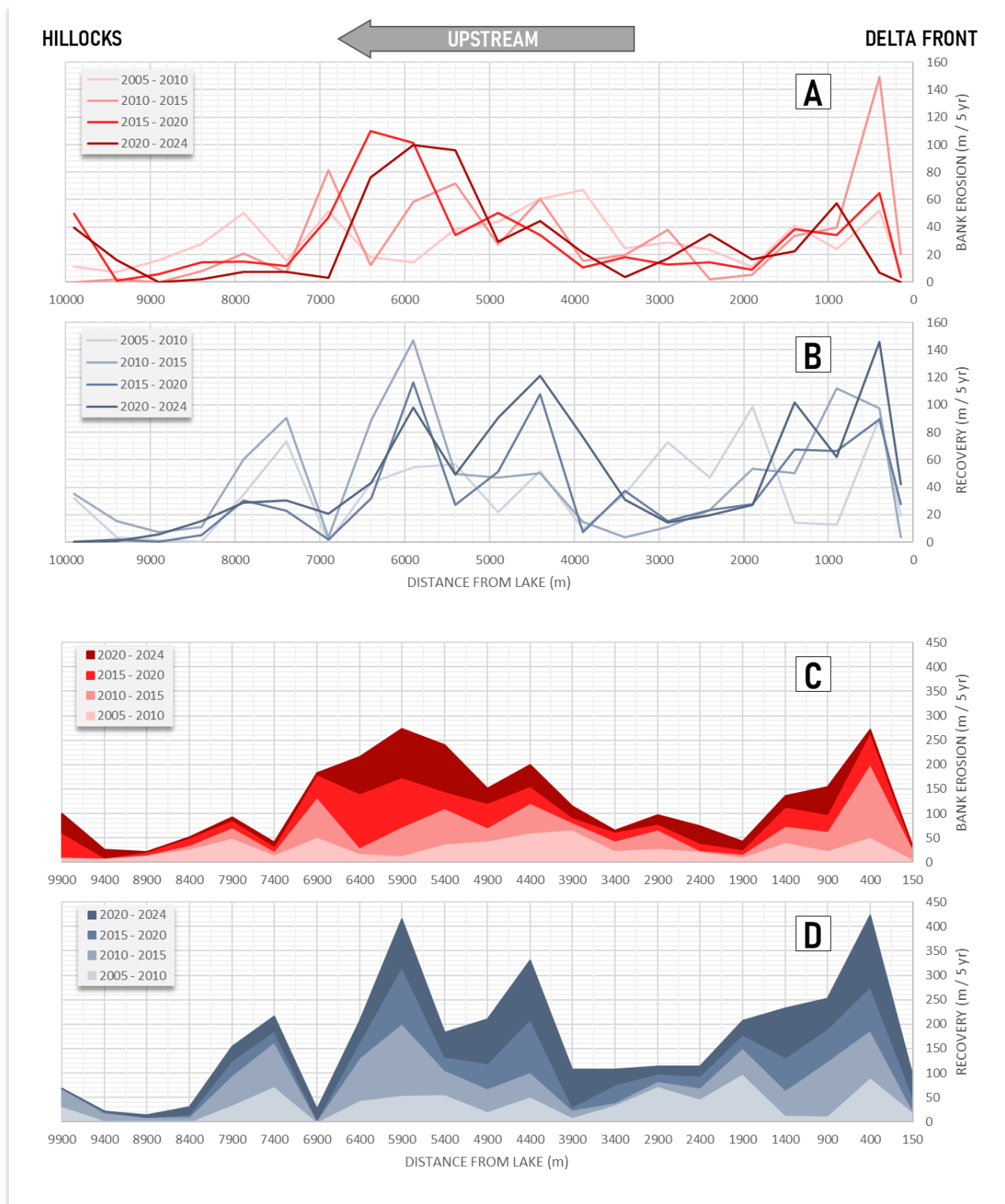


**FIGURE 32.** Average longitudinal rates of bank erosion and channel recovery calculated for 5-year intervals. Data are integrated over 500 m intervals. Highest rates of bank erosion occur between 4 -7 km upstream and are widely above 200 m over this 20 year period. Total rates of recovery slightly outpace erosion, suggesting a marginal decrease in the active width over the full period.

### 3.4 DEEPENING THE HISTORICAL PERSPECTIVE

Google Earth Engine archives only very limited imagery for New Zealand prior to the 1990s. To deepen the analysis of planform dynamics, the approach outlined in Section 3.1-3.3 was augmented with imagery downloaded directly from the USGS Earth Explorer data portal. This supports imagery from the earliest Landsat missions (Landsat 1 and 2), dating back to the early 1970s. These early scenes were imaged using the Multispectral Scanner System. Unlike later generations of optical sensors on Landsat 4 onwards, this sensor had only four spectral bands, captured at 6-bit radiometric resolution (64 grey levels) and a ground sample distance of 79 m. Data downloaded from Earth Explorer are however, resampled to 60 m to enhance compatibility with the later generation of (30 m) imagery generated by Landsat 4-9. While this lower resolution presents an additional constraint on the granularity of detectable change, as the typical active channel width exceeds 1 km for much of the lower Dart (downstream of river km 25), the degradation in resolution is not a limiting factor.

A new timeline of active channel width was compiled using a selection of cloud-free images from 1973 to 2019, sampled at c. 15 year intervals as shown in Table 7.

ACQUISITION DATE	PLATFORM	SENSOR	SCENE ID
10 DECEMBER 1973	LANDSAT 1	MSS	LM10810911973344AAA05
21 DECEMBER 1990	LANDSAT 4	TM	LT40760911990355XXX03
17 JANUARY 2001	LANDSAT 7	ETM+	LE70760912001017EDC00
17 APRIL 2019	LANDSAT 8	OLI	LC80760912019107LGN00

**TABLE 7.** Archival Landsat scenes used to compile a historical analysis of channel planform dynamics from 1973 – 2019. MSS = Multispectral Scanner System; TM = Thematic Mapper; ETM+ = Enhanced Thematic Mapper+; OLI = Operational Land Imager.

Given the range of different sensors involved, an alternative approach to image classification was employed. A random forest algorithm was to develop a supervised classifier. This was trained using labelled land cover polygons, created by visual interpretation of the true colour composites. A four-fold classification scheme was used comprising: (1) water; (2) exposed gravel; (3) partially vegetated bars; and (4) stable vegetation. Classes (1) and (2) were also aggregated to define an ‘alluvial’ class that represents the active channel bed.

The classifier was trained on each Landsat scene individually to account for variations in band wavelength and radiometric bit depth. The classified images were then summarized longitudinally, using 1 km cells spanning the 39 km of the Dart River to just beyond Slip Stream (765,520E 4,941,420S m). Upstream of this, the valley floor was deemed too narrow for reliable quantification with the lowest resolution (1973) imagery.

The temporal sequence of active channel width (classes 1 + 2; water and exposed gravel) is shown spatially for the lower river below Paradise and also summarized at 1 km resolution for the wider reach in Figure 33.



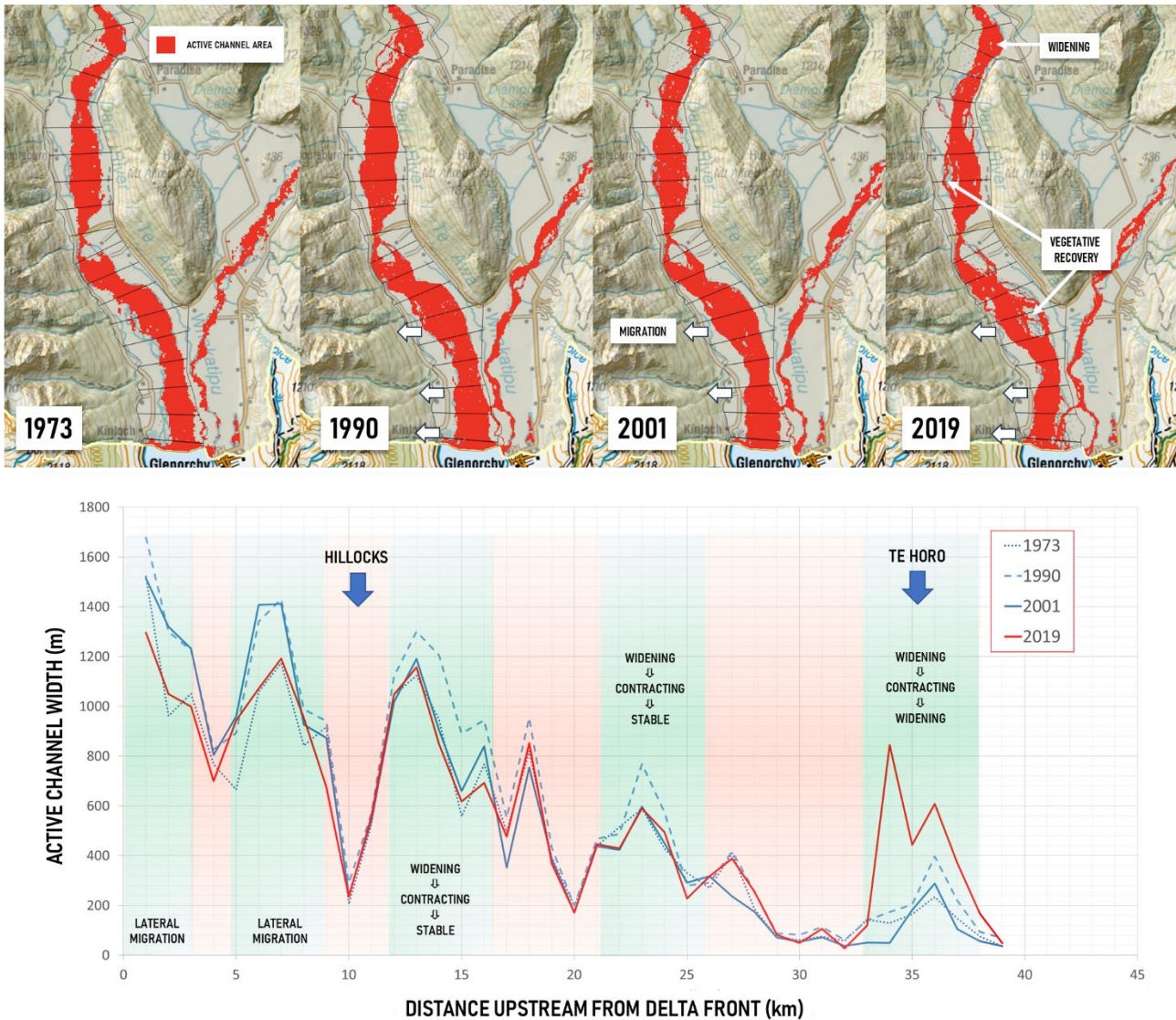


**FIGURE 33.** Long-term pattern of planform adjustment on the lower Dart River, compiled from the analysis of Landsat scenes from 1973 to 2019. The data reveal a widespread pattern of widening between 1973 – 1990, followed by progressive contraction of the river, most marked in the lower 10 km. The influence of recent landsliding a Slip Stream/Te Horo landslide at river km 25 is evidenced by the significant increase in exposed gravel between 2001-2019.

A number of key observations are evident from this analysis:

- The left-to-right migration of the active channel of the Dart downstream from the Hillocks is apparent through the entire series, with the axis of the lower river veering west by over 600 m since 1973.
- Where the channel is unconfined, the active width expands between 1973-1990, before contracting to 2001 and further still by 2019. This initial expansion exceeds 200 m in sections of the channel below the Hillocks, but is also evident at river kms 12-16, and also above Slip Stream (km 32-38). While the expansion between 1973 and 1990 may be linked to the lower spatial and spectral resolution MSS to Thematic Mapper imagery (Landsat 1 to Landsat 4), the subsequent reduction in width between 1990-

2019 is likely to be more robust. Moreover, this trend is mirrored in the analysis of the GEE imagery discussed in section 3.3. which found a c. 50 m decrease in active width over the last 20 years. This pattern appears linked to vegetative recovery and the establishment of islands that fragment the active channel, particularly between 2001 and 2019.

- A significant expansion of the ‘active channel’ at the Slip Stream landslide is evident between 2001 and 2019. This reflects both growth of the basal fan (river km 32-33) and the upstream sedimentation zone (river km 34-38) following reactivation of this landslide complex in January 2014. By 2022 the riverine lake created by the landslide had largely drained, however, extensive sedimentary flats were still unvegetated and dominate the signal here (see 3.5 below).

The long-term pattern of channel migration highlights the centennial timescales associated with the dynamics of the whole channel belt as it progressively reworks the valley floor. The REM (Relative Elevation Model) shown in Figure 9 highlights the likelihood for the active channel to continue to migrate into the lower lying western margins of the valley floor. The recent outflanking of the stopbank north of Turner’s Creek also creates the opportunity for the river to exploit the topographic low in the western valley floor between river km 6-7. Downstream of this, there is a low-lying pathway between Turners Creek and Glacier Burn and, if activated, this will cut-off and strand the current Kinloch-Hillocks Road in a new mid-channel island.

The recent contraction of active channel between 2001 and 2019 is less readily interpreted. There remains the potential for methodological bias (given the difference between the ETM+ and OLI sensors), but the pattern shown is consistent with visible interpretation of the true colour composite images. The contraction in active width is clearly related to vegetation encroachment and island development. This is evident in the 2019 classified image on the true left between river km 4-5 and upstream on the true right between river km 10-11 (see labels on Figure 33). Intriguingly, there is some evidence that this trend is reversed upstream of Paradise (river km 16), with an expansion in channel width between 2001 and 2019 (see the longitudinal plot of active width). One possible explanation for this, is the downstream translation of a sediment wave created by the Slip Stream landslide in 2014. Such waves have the potential to create transient cycles of channel aggradation (linked to widening) and degradation (linked to narrowing). Further analysis is required to establish whether this is the driver of longitudinal variability in the adjustment of channel width, but it is plausible that asynchronous downstream changes in channel width are linked to the translation of sediment pulses from discrete sources such as Slip Stream.

### 3.5 THE SLIP STREAM LANDSLIDE

The major landslide complex at Slip Stream represents the most significant contemporary sediment source in the Dart River catchment. The structure and history of this landslide is discussed in detail in Thomas and Cox

(2009) and more recently in Cox et al., (2014). The slope failure lies on the eastern side of the Cosmos Peaks and stretches from the ridge crest at between 1800-2100 m ASL, down to the valley floor at c. 440 m. The landslide has created a large debris fan with its apex at 600 m ASL. The fan is c. 1800 m wide and 1000 m from apex to toe, with an average gradient of 16%. Thomas and Cox (2009) used vegetation changes on the fan, observed in aerial photography, to infer the pattern of activity of this landslide since 1966. They estimate that the slide periodically fed debris flows comprising  $10^4 - 10^5 \text{ m}^3$ , reworking 65% of the fan surface between 1966-2009.

In late 2013, there were anecdotal reports of increased activity and then following heavy rainfall, a major debris flow impounded the Dart on the 4<sup>th</sup> January 2014. Cox et al. (2014) undertook a rapid reconnaissance survey following this event and found that while the dam was breached quickly after formation, they observed remnant alluvial terraces that suggested the transient dam had a crest level of >16 m. Following the breach, growth of the fan toe had displaced the channel towards the true left where it was actively undermining the valley walls below Sandy Bluff and introducing significant woody debris into the channel. Reduced conveyance through the breach also led to the formation of a new riverine lake that extended over 4 km upstream, inundating Dredge Flat.

In April 2014, a UK NERC project ([https://gotw.nerc.ac.uk/list\\_full.asp?pcode=NE%2FM005054%2F1](https://gotw.nerc.ac.uk/list_full.asp?pcode=NE%2FM005054%2F1)) led by James Brasington (then of Queen Mary, University of London) was established to quantify the impact of this major landslide on the fluvial system of the Dart catchment. This research provided critical information on the volume of sediment contribution from this landslide into the Dart River and the upstream impact of impoundment by the breach.

### 3.5.1 FORMATION AND DRAINAGE OF THE RIVERINE LAKE

The newly formed lake was surveyed using a boat-tethered Sontek HydroSurveyor in May 2015. While the survey occurred some 16 months after the initial debris flows impounded the river, satellite imagery confirmed that the extent of the lake had remained largely unchanged over this period. More than 54,000 survey grade soundings, spanning the full length of the lake were captured. These were interpolated to generate the 1 m raster bathymetric and water depth models shown in Figure 34.



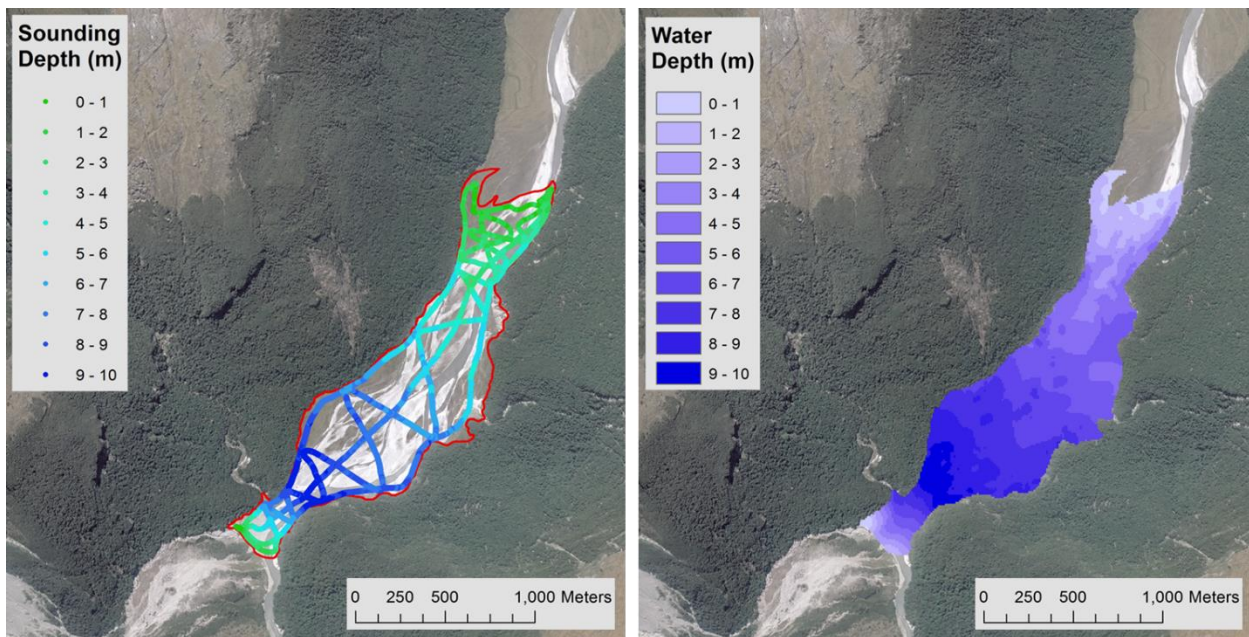


**FIGURE 34.** Soundings and interpolated bathymetry of the lake formed by impoundment of the Dart River. The survey revealed the lake to have a surface area of 1,100,000 m<sup>2</sup> (or 110 ha) and a volume of 6,300,000 m<sup>3</sup>. The maximum observed depth was 10.1 m and the mean depth 5.7 m. The size and scale of the system provides compelling contemporary evidence for the inferred genesis of the alluvial flats in the both the upper Dart and the Rees above Muddy Creek (see earlier discussion in 1.2 and 1.3).

Satellite imagery reveals that this lake had largely drained by 2022. However, during this time, the lake acted as a significant sediment trap, reducing the longitudinal connectivity of bedload sediment transport from the upstream catchment. The debris flows in 2014, therefore, not only created a major sediment pulse in the Dart - injecting a large volume of material following the landslide - but also served to then reduce dramatically the upstream supply. This highly unsteady sediment supply has the potential to generate cyclical patterns of channel adjustment that translate downstream as waves of aggradation (sediment fill) followed by subsequent degradation (incision). Such behaviour may explain the longitudinal adjustment of active width described above in 3.4.

Incidentally, the possibility to quantify the volume of sediment fill in the now drained lake now presents a remarkable research opportunity to understand sediment supply in the upper Dart catchment.

### 3.5.2 LANDSLIDE VOLUME AND FLUVIAL SEDIMENT SUPPLY

During initial reconnaissance, Cox et al. (2014) mapped the perimeter of fresh debris flow deposits on the Slip Stream fan to provide a first order estimate of the volume of material delivered by the January 2014 event. Their calculations suggested that c. 1 m m<sup>3</sup> of sediment may have been emplaced on the fan but note that this estimate was based on the interpretation of planimetric data alone. Smaller events are likely to



deposit most of their failed material on the fan. In more substantial failures, such as January 2014, the ratio of material being supplied directly to the river is likely to be much higher. Accurate information on this volume of fluvial sediment supply is needed to understand the relative role of such high magnitude events and to contextualize this within the longer-term averages established from the rate of delta sedimentation discussed in 1.4.

Brasington et al., (2018) used photogrammetric modelling of Maxar WorldView 1 and 2 satellite imagery to create a timeline of 3D models of the Slip Stream sediment delivery system. These were used to quantify the landslide sediment budget using standard DEM differencing techniques as discussed in section 2.3. This approach enables segmentation of volumetric changes in the key components of the landslide system: a) the source erosion volume; b) sedimentation on the fan; c) the total contribution of (all grades of) sediment to the river system by inference (i.e.,  $[a] - [b]$ ).

The WorldView series of satellites capture 'very high resolution' (VHR) along-track stereo-panchromatic and multispectral imagery from nadir and off-nadir views. This enables precise 3D scene restitution using the supplied rational polynomial coefficients to model the camera interior and exterior geometry (see Sefercik et al., 2013 and Wang et al. 2019 for further details). Panchromatic imagery from the Worldview 1 and 2 imagers has a ground sample distance of 0.3 and 0.46 m respectively. Using automated stereo-matching, this facilitates the production of digital surface models (DSMs) at 1 m horizontal resolution and with theoretical vertical accuracies that range from 0.8 - 1.3 m (RMSE at 1 sigma). These performance metrics can be enhanced with the support of high-quality ground control observations and for some cases, reported vertical accuracies approach those more typically associated with airborne lidar (see Wang et al., 2019).

Photogrammetric modelling was undertaken using the NASA AMES Stereo Pipeline (Shean et al., 2016), employing a network of GCPs associated with paint marks and hardpoints, acquired retrospectively using RTK GNSS in 2017. Two sets of stereo scenes, bracketing the event in 2014 were selected for photogrammetric reconstruction and differencing. These were acquired on **06 Jun 2012** (WorldView 1, Scene 056057382010) and **15 Feb 2015** (WorldView 2, scene ID = 056057385010). Independent checkpoint analysis used 251 ground observations, and found RMS errors (1 sigma) of 0.49 m and 0.55 m for the 2012 and 2015 models respectively.

The two digital surface models were used to compute a geomorphic sediment budget for the landslide, using the GCD software suite described in Section 2.3. Given the large magnitude of vertical change associated with the landslide processes, the 1 sigma (68%) error estimates were used to define a simple uniform error model for each DSM. No attempt was made to correct the raster models to for vegetation cover, rather an

Area of Interest (AOI) was used to limit the change detection model to bare areas. The resulting model of elevation change between 2012 and 2015 is shown in Figure 35.

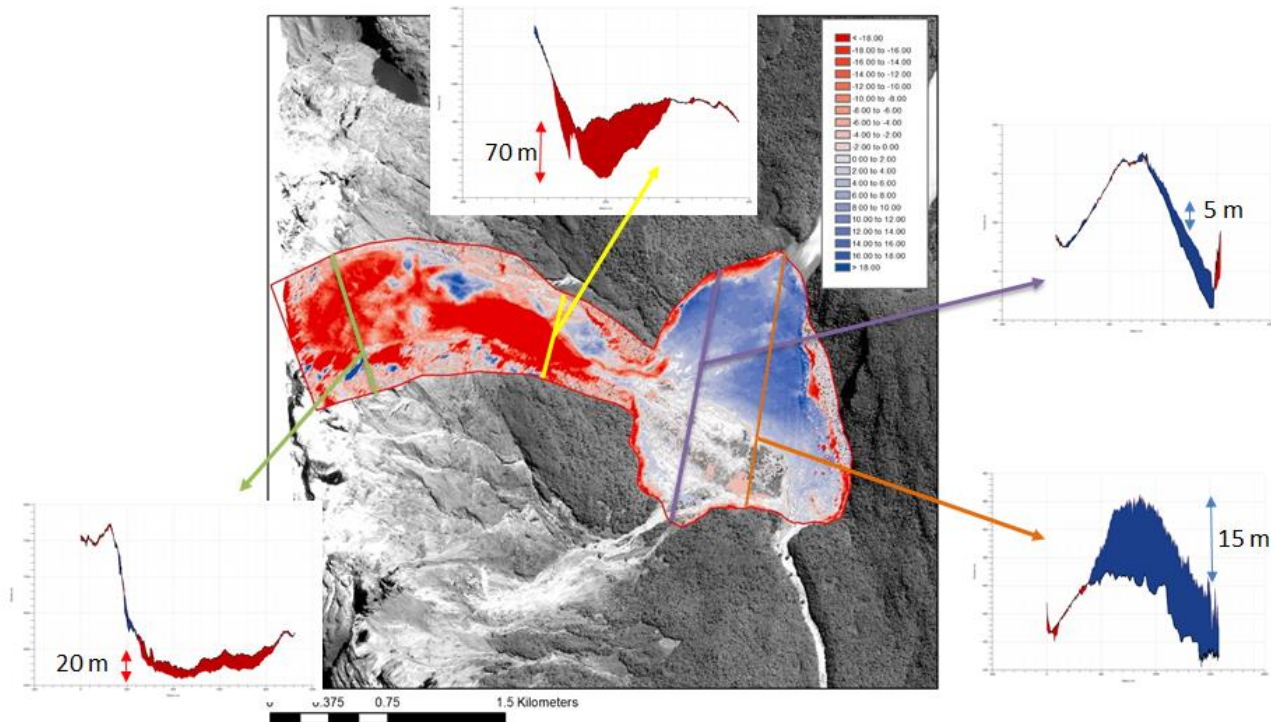


**FIGURE 35.** Elevation change model derived from 2012 and 2015 WorldView DSMs, bracketing the 2014 landslide at Slip Stream. This a large transfer of mass at the top of the landslide (20 m of vertical deformation) to a deep gully above the fan, where flows have scoured to a depth of over 70 m, further destabilising the flanks of the gully. Deposition is focused on the upstream (northern) half of the fan, where sedimentation depths may exceed 15 m.

Widespread vertical deformation is clearly evident at the top of the landslide, where surface elevations are reduced by over 20 m in an arcuate band below the ridgeline. The transfer of this mass downslope, most likely as a debris flows and rapid debris topples, has scoured the central landslide gully by >70 m; oversteepening the flanks of the gully and enhancing lateral flows into the gully and downslope. These debris flows are likely to have episodically blocked the main drainage channel to the fan, created pulsating sediment waves of as the blockages are breached and debris flows spill down-fan and into the river. This behaviour was observed on January 7<sup>th</sup> 2014 during field reconnaissance by GNS (see Cox et al., 2014).

A volumetric budget of the changes between the 2012 and 2015 surface models is presented in Figure 36, in which all elevation changes are computed at the 68% confidence interval.

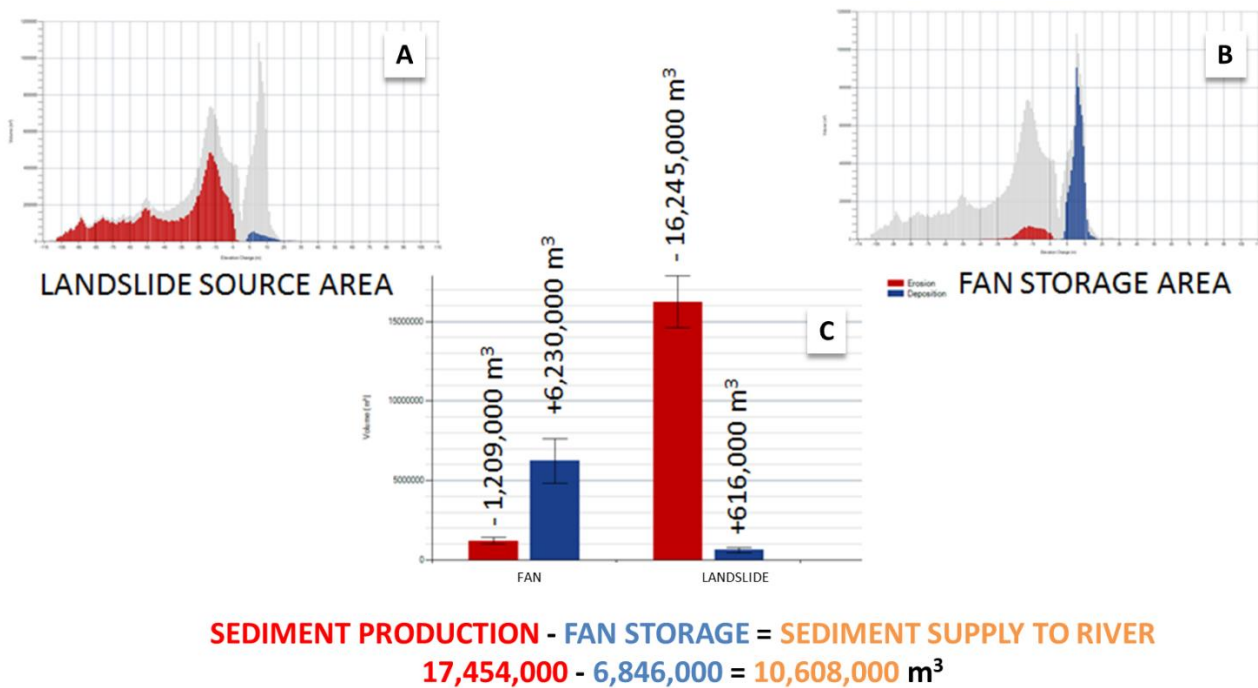


**FIGURE 36.** Volumetric budget for components of the landslide, derived from DEM differencing between the 2012 and 2015 elevation models.

The volumetric surface lowering from the landslide accounts for a net loss of 16,245,000 m³, with a further 1,209,000 m³ eroded from the fan surface. This compares to 6,230,000 m³ of surface raising on the fan (sedimentation), with elevation increases on the landslide (associated with slumped material) contributing a total of 616,000 m³. Balancing these elevation losses and gains provides a first order estimate of 10,608,000 m³ of sediment delivered from the landslide to the fluvial system.

A proportion of this material will have entered the newly formed lake from the northern margins of the fan, where it may remain in storage until reworked following drainage of the lake. The majority of the >10 M m³ however, will have entered the Dart River directly or been stored only transiently as the river was dammed and then breached. This input will have incorporated the full range of sediment size classes, from boulder sized material that was evident in the remnants of the breached dam, through to clay and silt sized material transported in suspension. Rapid dispersion of the wash and suspended load components of this major sediment pulse is evident in the extensive turbidity plume visible through nearly the entire length of Lake Wakatipu by mid-January 2014 (see Figure 37).







The contribution of coarse sediment ( $2\text{ mm} < d_{50} < 256\text{ mm}$ ) to the river remains unknown. This sediment fraction creates the channel framework and its longitudinal flux variability dominates the pattern of morphology adjustment. Unfortunately, the WorldView DEMs are of insufficient vertical accuracy to enable a detailed study of three-dimensional channel changes, and there is no available lidar data that brackets the event. As context however, the long-term record of delta sedimentation discussed in 1.5 inferred an annual (coarse) load of c. 180-270,000  $\text{m}^3$ . This annual yield is just 2-3% of the total landslide flux to the fluvial system estimated for this event. Even after accounting the sequestration of material into long-term storage upstream, it therefore seems likely that the coarse sediment pulse represents at least an order of magnitude more than the average annual rate of delta sedimentation. There are tentative signals of morphological impact in the increasing width of active channel belt above river km 16 (c. Paradise) between 2001 and 2019. This pattern is most notable between river km 26-29 around Chinamans Bluff where the river is first unconfined downstream from Slip Stream. While this result is clearly tentative, it highlights the possibility that widening may be linked to aggradation and, albeit more tentatively, that narrowing may infer subsequent degradation. The downstream passage of sediment pulses associated with discrete inputs, such as landslides of this type, could therefore potentially be tracked by using 2D satellite image analysis and provide important insights into the likelihood of channel instability.

## 4. FLUVIAL PROCESSES AND HAZARDS

### 4.1 GUIDING GEOMORPHIC PRINCIPLES

This analysis of geomorphic processes on the Rees and Dart Rivers highlights a number of important principles that can help to inform future management strategies for communities at the Head of Lake Wakatipu:

**PRINCIPLE 1:** Catchment sediment supply is high and punctuated by extreme climatic and geomorphic events.

**PRINCIPLE 2:** Sediment transport through the mainstem reaches is capacity-limited during large events.

**PRINCIPLE 3:** Observations show that both rivers are undergoing long-term aggradation, a process that drives elevated rates of lateral mobility and contributes to persistent channel instability.

These three principles encapsulate how contemporary river behaviour in the Rees and Dart reflects deeper regional controls. High sediment supply (Principle 1) is driven by a combination of active tectonic uplift and the dominance of weak, easily eroded lithologies, while the transport-limited nature of flood events (Principle 2) and long-term aggradation (Principle 3) are shaped by the inherited landscape template left by Late Quaternary glaciation. Together, these controls create a contingent physical setting—one in which high sediment fluxes interact with glacially sculpted valley floors to produce dynamic and often unstable fluvial systems. It is within this context that the present hazards associated with river processes must be understood.

While both rivers exhibit a long-term tendency toward aggradation, shorter-term fluctuations in bed level reflect the episodic nature of sediment delivery and transport capacity. As outlined in the conceptual model presented in Section 2.5.3, high-magnitude storm events are associated with pulses of sediment delivery from well-connected sources in the upper catchments. During such events, the volume of material delivered to the piedmont reaches is likely to exceed the channel's capacity to transport sediment downstream, resulting in rapid and spatially extensive aggradation. In the periods between major floods, smaller flow events may partially rework and redistribute this deposited material. This pattern of punctuated aggradation and intermittent reworking characterises the short-term bed level dynamics of the system. Under projected climate change scenarios—where both the frequency and intensity of extreme precipitation events are expected to increase (NIWA, 2019)—it is anticipated that the rate and magnitude of sediment accumulation in the lower reaches will intensify, compounding the hazards associated with aggradation.

## 4.2 FLUVIAL HAZARDS

Together, these principles frame a geomorphic system that is highly dynamic and sensitive to episodic disturbance. The combination of high sediment supply, transport-limited flood events, and ongoing aggradation creates a physical environment prone to rapid—and often unpredictable—morphological change. These processes give rise to a suite of natural hazards that are of direct relevance to communities and infrastructure at the head of Lake Wakatipu.

Three key hazard pathways emerge from this understanding:

1. **Loss of channel capacity**, which progressively elevates flood risk over time and reduces the level of service provided by existing assets, including the Glenorchy–Paradise bridge;
2. **High rates of lateral channel migration** and reworking of the valley floor, posing a sustained threat to infrastructure such as the Kinloch Road; and
3. **Increased risk of catastrophic breakout flooding**, associated with the avulsion of super-elevated channels - events that can abruptly redirect floodwaters and outflank existing flood protection.

These pathways are illustrated schematically in **Figure 38**.

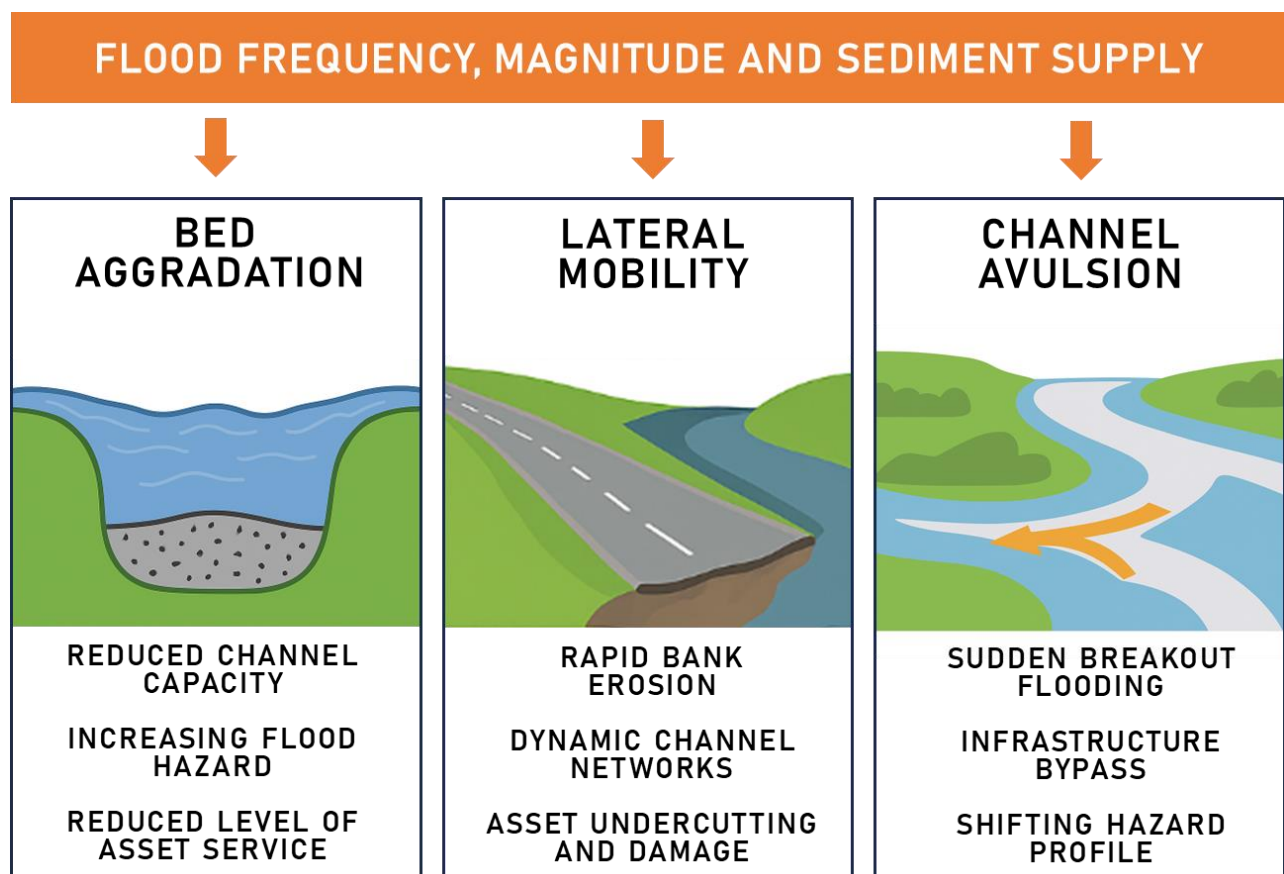


**FIGURE 38.** Geomorphologically driven river hazard pathways at the top of Lake Wakatipu.

Comprehensive assessments of the hazardscape at the head of Lake Wakatipu have been undertaken as part of the Otago Regional Council Natural Hazard Adaptation strategy (see: <https://www.orc.govt.nz/get-involved/projects-in-your-area/head-of-lake-whakatipu>). This programme has incorporated extensive quantitative assessments of the hazards and associated risks, and linked optioneering to evaluate alternative strategies of best management. This report provides important context for the scenarios used to underpin that work.

The recently commissioned reports provide detailed assessments of the specific hazards, so here only a brief overview of the wider context is presented. The following sections examine each of these in relation to the geomorphic dynamics described above.

#### 4.2.1 LOSS OF CHANNEL CAPACITY

The analysis of channel change by DEM differencing reveals significant aggradation occurring in the lower Rees River. This finding is consistent with the long-term trend in delta progradation documented by Wild et al. (2013) and previous examinations of the hazardscape at Glenorchy (ORC, 2013). Analysis of surface elevation change over the past decade reveals bed level increases that exceed 0.2 m widely through the lower 4 km of the Rees. While the lack of upstream lidar coverage before 2019 makes assessment of trends upstream here more difficult, the integrated change between 2022 and 2019 averages close to 0.1 m and locally exceeds 0.2 m, particularly where the channel is semi-confined. This reduction in cross-sectional capacity progressively elevates flood risk by raising water levels for a given discharge and diminishing conveyance.

The implications of such aggradation are threefold. First, the raised bed level lowers the threshold for overbank flooding, thereby increasing the probability of inundation under both current and projected climate conditions. With flood frequency and magnitude anticipated to rise, the progressive accumulation of sediment is likely to emerge as the dominant control on future flood risk in this setting.

Second, aggradation reduces the design level of service provided by existing infrastructure. This is especially evident at the Glenorchy–Paradise Road bridge, where anecdotal evidence supports a long-term trend of rising bed level. It is also relevant for the northern perimeter stopbank that encircles Glenorchy, which provides only a low level of service and is in poor condition.

Third, aggradation heightens the likelihood of infrastructure being outflanked during moderate to high flows. This is particularly apparent again at the GY-Paradise bridge, where flow bypass channels may become more active, but also applies to the true-right stopbank between river kilometres 8 and 12.



#### 4.2.2 LATERAL CHANNEL MIGRATION AND INFRASTRUCTURE EXPOSURE

Lateral migration and channel reworking are characteristic behaviours of aggrading braided rivers. Analysis of archival satellite imagery reveals that the active channel of the Dart has migrated laterally from left to right by over 600 m below river km 7. The resolution of historic satellite imagery limits similar analysis of lateral dynamics on the Rees. However, superimposition of recent DEM differencing models with the earliest comprehensive regional orthophotography confirms that comparable scales of lateral reworking also occur on the Rees (Figure 39).

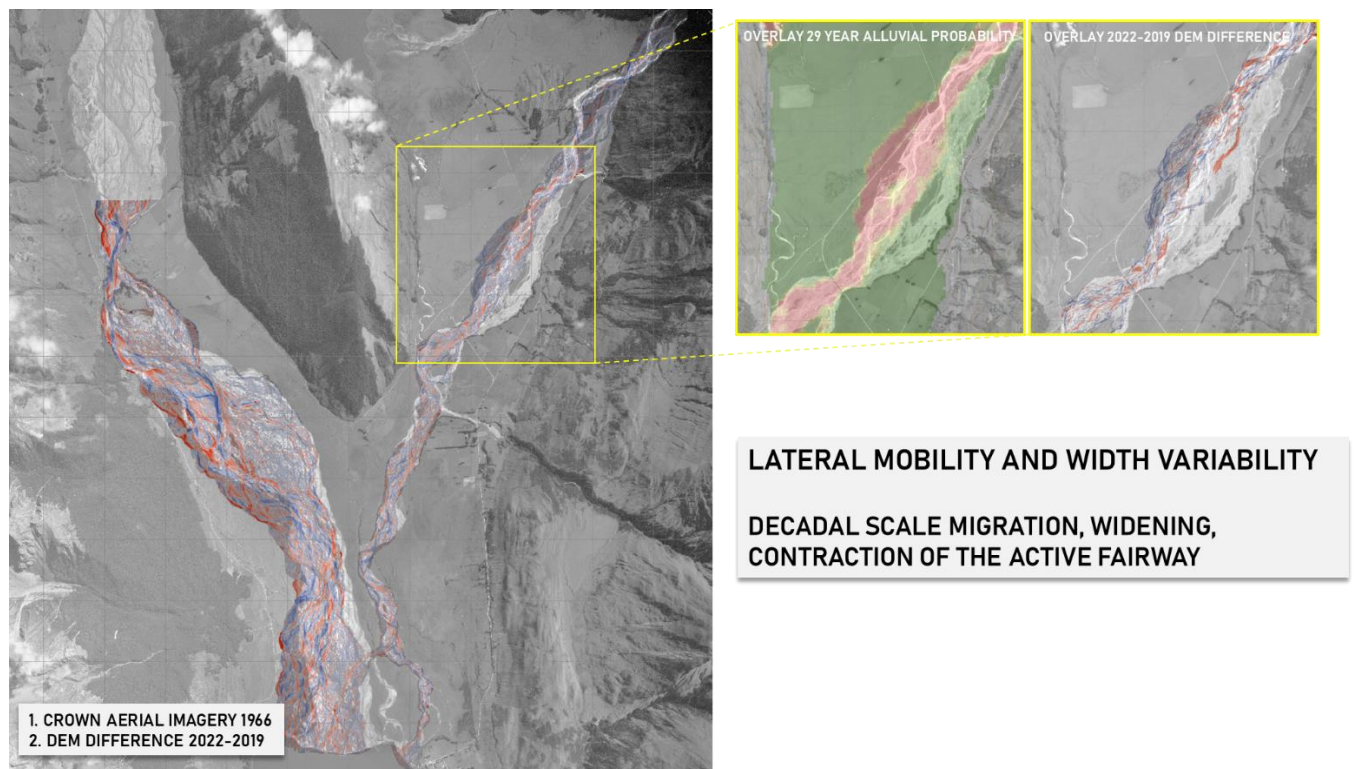


**FIGURE 39.** Comparison of DEM difference models from between 2019-2022 and the earliest comprehensive regional orthophotography from 1966 reveals significant laterally mobility on both the lower Dart and Rees Rivers.

This degree of channel reorganisation poses substantial risk to linear infrastructure located within or near the braidplain margins. The Kinloch Road, in particular, lies within the active zone of lateral adjustment. As the river migrates across the valley floor, bank erosion and channel incision may lead to sudden undermining or exposure of road alignments. Notably, westward migration of the Dart River accelerated after 2016 when the stopbank upstream of Turners Creek was outflanked—highlighting the likely ineffectiveness of piecemeal flood protection infrastructure within such a dynamic corridor.

Over longer timeframes, it is likely that active channel width and lateral mobility respond sensitively to major sediment pulses—such as those generated by the landslide complexes at Slip Stream and Muddy Creek. Ongoing contributions from these sources, combined with increased sediment loads associated with more frequent and intense flood events, are expected to further amplify the threat to unprotected infrastructure.

#### 4.2.3 CHANNEL AVULSION AND BREAKOUT FLOODING

Perhaps the most acute hazard pathway is associated with the avulsion of super-elevated channels. Persistent aggradation, especially where lateral confinement restricts accommodation space, creates a scenario in which the active channel bed is elevated above the adjacent floodplain. As this relative freeboard declines, the likelihood of avulsion increases sharply. Avulsions are typically initiated during high-intensity events where floodwaters breach natural or artificial levees, seeking shorter and steeper alternative flow paths.

Observations from the 2020 flood demonstrate that multiple floodplain pathways exist to reroute floodwaters below the Glenorchy-Paradise. Perhaps the most significant of these, is linked to evidence of breakout flooding on the true left between river km 4-6. Here, floodwaters are rapidly directed down the steep floodplain gradient into the Glenorchy lagoon system, placing pressure on the northern perimeter stopbank. Should this structure be overtopped or fail, floodwaters could circulate around the back of Glenorchy township, presenting a severe and fast-moving flood hazard to residential areas.

The analysis of bed level change in this report was used to guide numerical flood hazard simulations undertaken by Land River Sea Consulting in 2022 (see: LRS, 2022). While these simulations reveal the extent of flooding overtopping the perimeter stopbank to be well confined, the analysis did not consider the erosive power of high-velocity floodwaters. A less well-constrained hazard remains associated with mobile bed dynamics and the potential impact of rafted debris.

Unlike gradual aggradation or bank erosion, avulsions represent step changes in flood behaviour and are notoriously difficult to anticipate. The geomorphic evidence presented in this report indicates that, in the absence of intervention, such events should not be considered anomalous, but rather an inevitable expression of sediment imbalance and dynamic adjustment in this type of river system.

## 5. CONCLUSIONS

This report examined the geomorphic dynamics of the Rees and Dart Rivers and THE physical processes that underpin flood and erosion hazards at the head of Lake Wakatipu. Drawing on high-resolution DEM differencing, image analysis and conceptual process models, the analysis has provided a detailed picture of how sediment supply, transport capacity, and channel form interact to shape these dynamic river systems.

The findings support three overarching geomorphic principles. First, both catchments exhibit high sediment supply, linked to active tectonics, weak lithologies and high rainfall. Sediment supply is punctuated by extremes relating to significant slope failures and severe floods. Second, sediment transport capacity is exceeded during large floods, resulting in widespread deposition. Third, persistent aggradation drives high rates of lateral channel mobility and contributes to instability at multiple scales.

DEM differencing has quantified the magnitude and spatial extent of recent aggradation. In the lower Rees River, bed level increases exceed 0.2 m over the past decade, with localised maxima occurring where confinement promotes deposition. In the Dart, historical imagery and topographic analysis confirm over 600 m of lateral migration since the 1970s, with recent change driven in part by stopbank outflanking near Turners Creek. These observations reinforce the dynamic and contingent behaviour of the system—responses to sediment pulses, event sequencing, and boundary controls are all spatially variable and time-dependent.

This geomorphic context has direct implications for flood and erosion hazard. Three principal hazard pathways emerge from the findings: (1) progressive loss of channel capacity due to aggradation, increasing the frequency and severity of overbank flooding; (2) continued lateral migration of active channels, elevating risk to linear infrastructure and complicating efforts to stabilise channel margins; and (3) increasing likelihood of avulsion, particularly where super-elevated channels intersect low-lying floodplain routes. These hazards are not anomalous but represent natural, process-driven outcomes of the sediment dynamics documented in this study.

Importantly, the evidence presented here highlights that the fluvial hazards at the head of Lake Wakatipu cannot be understood without reference to the geomorphic context in which they arise. The Rees and Dart are not simply conduits for floodwaters—they are sediment-rich, laterally mobile systems whose morphology is constantly evolving. Any future management strategy must acknowledge this inherent dynamism and develop approaches that are responsive to the spatial and temporal variability in river behaviour. The findings of this report provide a baseline for that understanding and offer a geomorphically grounded framework for interpreting past change, assessing present conditions, and anticipating future trajectories.

## 6. REFERENCES

- Allen, G.H. & Pavelsky, T.M. 2018. Global extent of rivers and streams. Science, 361, 585–588
- Anderson, S. W. (2019) Uncertainty in quantitative analyses of topographic change: error propagation and the role of thresholding. Earth Surface Processes and Landforms, 44: 1015–1033.
- ASPRS. 2015 Positional Accuracy Standards for Digital Geospatial Data. Photogrammetric Engineering and Remote Sensing, 81, 1073–1085.
- Barrell D.J.A. 2019. Assessment of liquefaction hazards in the Queenstown Lakes, Central Otago, Clutha and Waitaki districts of the Otago Region. Lower Hutt (NZ): GNS Science. 99 p. Consultancy Report 2018/67.
- Carbonneau, P.E. & Bizzi, S. 2024. Global mapping of river sediment bars. Earth Surface Processes and Landforms, 49, 15–23.
- Cox, S.C., McSaveney, M.J., Rattenbury, M.S., Hamling, I.J. 2014. Activity of the Landslide Te Horo and Te Koroka Fan, Dart River, New Zealand during January 2014. GNS Science Report, 2014/07, 45 p.
- Brasher, L.R. 2006. Monitoring of riverbed stability and morphology by regional councils in New Zealand: application to gravel extraction management. Landcare Research Contract Report: 0506/138.
- Brasington J, Langham J, Rumsby B. 2003. Methodological sensitivity of morphometric estimates of coarse fluvial sediment transport. Geomorphology, 53, 299–316.
- Brasington, J. 2010. From grain to floodplain: Hyperscale models of braided rivers, Journal of Hydraulic Research, 48, 52–53.
- Brasington, J. 2018. The Opportunities and Challenges of Modelling Watershed-Scale River Morphodynamics with SFM Photogrammetry. GSA Annual Meeting, Indianapolis, USA, 04-07, Vol. 50, 10.1130/abs/2018AM-323954.
- Coursey, S. and Mountjoy, J. 2022. Sediment coring and geophysical survey data report, Lake Wakatipu. NIWA Client Report No, 2022169WN, 26 pp.
- Davies, T.R., McSaveney, M.J. and Clarkson, P.J., 2003. Anthropogenic aggradation of the Waiho River, Westland, New Zealand: microscale modelling. Earth Surface Processes and Landforms, 28, 209–218.
- Dowling, L. et al., 2021. Local summer insolation and greenhouse gas forcing drove warming and glacier retreat in New Zealand during the Holocene, Quaternary Science Reviews, 266, 107068.
- Gorelick, N., Hancher, M., Dixon, M., Ilyushchenko, S., Thau, D., & Moore, R. 2017. Google Earth Engine: Planetary-scale geospatial analysis for everyone. Remote Sensing of Environment, 202, 18–27.
- Huete, A., Didan, K., Miura, T., Rodriguez, E. P., Gao, X., & Ferreira, L. G. 2002. Overview of the radiometric and biophysical performance of the MODIS vegetation indices. Remote Sensing of Environment, 83, 195–213.
- Hicks, D. M., Baynes, E. R. C., Measures, R., Stecca, G., Tunnicliffe, J., and Friedrich, H. 2021. Morphodynamic research challenges for braided river environments: Lessons from the iconic case of New Zealand. Earth Surface Processes and Landforms, 46: 188–204



- Lague, D., Brodu, N. and Leroux, J., 2013. Accurate 3D comparison of complex topography with terrestrial laser scanner: Application to the Rangitikei canyon (NZ). ISPRS Journal of Photogrammetry and Remote Sensing, 82, 10-26.
- Land River Sea (2022). Rees/Dart Rivers: Flood Hazard Modelling. Accessed at, [https://www.orc.govt.nz/media/12459/land-river-sea-ltd-2022-dart-rees-rivers-flood-hazard-modelling\\_final-report-issued-1-june-2022.pdf](https://www.orc.govt.nz/media/12459/land-river-sea-ltd-2022-dart-rees-rivers-flood-hazard-modelling_final-report-issued-1-june-2022.pdf)
- Lane, S.N., Westaway, R.M. and Murray Hicks, D. 2003. Estimation of erosion and deposition volumes in a large, gravel-bed, braided river using synoptic remote sensing. Earth Surface Processes and Landforms, 28, 249-271.
- Lindsay, J. B. and Ashmore, P. E., 2002. The effects of survey frequency on estimates of scour and fill in a braided river 494 model, Earth Surface Processes Landforms, 27, 27–43.
- McColl, S.T. and Davies, T.R., 2011. Evidence for a rock-avalanche origin for ‘The Hillocks’ “moraine”, Otago, New Zealand. Geomorphology, 127(3-4), pp.216-224.
- McColl, S.T., Cook, S.J., Stahl, T. and Davies, T.R.H. 2019. Origin and age of The Hillocks and implications for post-glacial landscape development in the upper Lake Wakatipu catchment, New Zealand. Journal of Quaternary Science, 34: 685-696.
- Mohssen, M. 2021. Analysis of Flood Hazards for Glenorchy. Unpublished report for the Otago Regional Council, pp. 18.
- NIWA, 2019. Climate change projections for the Otago Region. NIWA Client Report No: 2019281WN, pp. 138.
- Otago Regional Council, 1999. Queenstown Lakes District Floodplain Report, 35 pp.
- Otago Regional Council, 2003. Rees River Sedimentation Investigation. Unpublished note, pp. 24.
- Otago Regional Council. 2008: Channel morphology and sedimentation in the Rees River. ISBN 1-877265-64-0, New Zealand, pp. 27.
- Otago Regional Council, 2013. Channel Morphology of the Rees River, Otago. ISBN: 978-0-478-37665-4, pp. 36
- Payton, M.E., Greenstone, M.H. and Schenker, N., 2003. Overlapping confidence intervals or standard error intervals: what do they mean in terms of statistical significance? J. Insect Science, 3, 34, pp.6.
- Piégay, H., Arnaud, F., Belletti, B., Bertrand, M., Bizzi, S., Carbonneau, P., Slater, L. 2020. Remotely sensed rivers in the Anthropocene: State of the art and prospects. Earth Surface Processes and Landforms, 45, 157–188.
- Richards, K., Brasington, J. and Hughes, F., 2002. Geomorphic dynamics of floodplains: ecological implications and a potential modelling strategy. Freshwater Biology, 47, 559-579.
- Rouse, J. W., Haas, R. H., Schell, J. A., & Deering, D. W. 1973. Monitoring vegetation systems in the Great Plains with ERTS. NASA Special Publication, 351, 309–317).
- Sefercik, U.G., Alkan, M., Buyuksalih, G. and Jacobsen, K., 2013. Generation and Validation of High-Resolution DEMs from Worldview-2 Stereo Data. The Photogrammetric Record, 28, 362-374.
- Shean, D.E., Alexandrov, O., Moratto, Z.M., Smith, B.E., Joughin, I.R., Porter, C., Morin, P., 2016. An automated, open-source pipeline for mass production of digital elevation models (DEMs) from very-

- high-resolution commercial stereo satellite imagery. ISPRS Journal of Photogrammetry and Remote Sensing, 116, 101-117.
- Spada, D., Molinari, P., Bertoldi, W., Vitti, A., & Zolezzi, G. 2018. Multi-temporal image analysis for fluvial morphological characterization with application to Albanian Rivers. ISPRS International Journal of Geo-Information, 7, 314.
- Stout, J.C. and Brasington, J., 2022. Probabilistic Modelling of Bathymetric Retrievals with a New Class of Small Format Shortwave lidar. AGU Fall Meeting Abstracts, 2022, EP12C-1046.
- Sutherland, J.L., Carrivick, J.L., Shulmeister, J., Quincey, D.J. and James, W.H., 2019. Ice-contact proglacial lakes associated with the Last Glacial Maximum across the Southern Alps, New Zealand. Quaternary Science Reviews, 213, pp.67-92.
- Thomas, J.S. and Cox, S.C. 2009. 42 years of evolution of Slip Stream landslide and fan, Dart River, New Zealand. Lower Hutt: GNS Science. GNS Science Report 2009/43, 32 p.
- Tomsett, C. and Leyland, J., 2019. Remote sensing of river corridors: A review of current trends and future directions. River Research and Applications, 35, 779-803.
- Turnbull, I.M. 2000. Geology of the Wakatipu Area: scale 1:250,000. Institute of Geological and Nuclear Sciences Limited, Lower Hutt, New Zealand.
- Vericat, D., Wheaton, J.M. and Brasington, J., 2017. Revisiting the morphological approach: Opportunities and challenges with repeat high-resolution topography. Gravel-bed Rivers: Processes and Disasters, pp.121-158.
- Waugh, J., & Webby, M.G. 2006. Hydraulic Behaviour of the Outlet of Lake Wakatipu, Central Otago, New Zealand. Journal of Hydrology (New Zealand), 45, 29–40.
- Wang, S., Ren, Z., Wu, C., Lei, Q., Gong, W., Ou, Q., Zhang, H., Ren, G. and Li, C., 2019. DEM generation from Worldview-2 stereo imagery and vertical accuracy assessment for its application in active tectonics. Geomorphology, 336, pp.107-118.
- Wild, M. 2013. Growth Dynamics of Braided Gravel-Bed River Deltas in New Zealand. PhD thesis, University of Canterbury, NZ.
- Williams, R.D. 2014. Two-dimensional numerical modelling of natural braided river morphodynamics. PhD thesis, University of Aberystwyth, Wales, UK.
- Winiwarter, L., Anders, K., & Höfle, B. 2021. M3C2-EP: Pushing the limits of 3D topographic point cloud change detection by error propagation. ISPRS Journal of Photogrammetry and Remote Sensing, 178, 240-258.
- Wu, Q., 2020. geemap: A Python package for interactive mapping with Google Earth Engine. The Journal of Open-Source Software, 5, 2305.
- Xu, H. 2006. Modification of normalised difference water index (NDWI) to enhance open water features in remotely sensed imagery. International Journal of Remote Sensing, 27, 3025–3033.

## APPENDIX 1

Tabulated summaries of the DEM registration analysis. Descriptive statistics of the aggregated elevation differences for the stable, reference areas shown in Figure 11. The results are tabulated to show changes between surveys (years); for land cover classes; and for years and land cover classes individually.

YEAR-COMPARISON	MIN	MAX	MEDIAN	MEAN	MEAN	POOLED $\sigma$	CI 10%	CI 90%	AREA (m <sup>2</sup> )
2011 - 2019	-0.062	0.185	0.068	<b>0.051</b>	<b>0.071</b>	<b>0.092</b>	-0.036	0.112	69,576
2011 - 2021	-0.059	0.166	0.076	<b>0.078</b>	<b>0.095</b>	<b>0.073</b>	0.009	0.166	56,468
2011 - 2022	-0.108	0.141	0.058	<b>0.033</b>	<b>0.073</b>	<b>0.082</b>	-0.08	0.095	69,576
2019 - 2021	-0.03	0.254	0.034	<b>0.043</b>	<b>0.056</b>	<b>0.057</b>	-0.028	0.101	119,478
2019 - 2022	-0.227	0.133	0.016	<b>0.005</b>	<b>0.055</b>	<b>0.069</b>	-0.065	0.074	171,289
2021 - 2022	-0.176	0.04	-0.016	<b>-0.024</b>	<b>0.031</b>	<b>0.039</b>	-0.061	0.008	119,478
									<b>605,865</b>

LAND COVER	MIN	MAX	MEDIAN	MEAN	MEAN	POOLED $\sigma$	CI 10%	CI 90%	AREA (m <sup>2</sup> )
PASTURE	-0.227	0.149	0.018	<b>0.019</b>	<b>0.064</b>	<b>0.036</b>	-0.015	0.077	236,521
ROAD	-0.025	0.083	0.055	<b>0.042</b>	<b>0.050</b>	<b>0.038</b>	0.001	0.08	77,948
SCRUB	-0.176	0.254	-0.01	<b>0.051</b>	<b>0.084</b>	<b>0.075</b>	-0.044	0.158	81,921
TREES	-0.108	0.166	-0.024	<b>0.000</b>	<b>0.062</b>	<b>0.094</b>	-0.082	0.081	209,475

YEAR COMPARISON	LAND COVER	MIN	MAX	MEDIAN	MEAN	MEAN	POOLED $\sigma$	CI 10%	CI 90%	AREA (m <sup>2</sup> )
2011 - 2019	PASTURE	0.034	0.075	<b>0.058</b>	<b>0.058</b>	<b>0.032</b>	0.054	0.038	0.071	16,291
2011 - 2019	ROAD	0.007	0.007	<b>0.007</b>	<b>0.007</b>	<b>0.054</b>	0.007	0.007	0.007	12,253
2011 - 2019	SCRUB	0.068	0.185	<b>0.160</b>	<b>0.160</b>	<b>0.080</b>	0.084	0.071	0.165	12,936
2011 - 2019	TREES	-0.062	0.094	<b>0.021</b>	<b>0.063</b>	<b>0.127</b>	-0.03	-0.056	0.069	28,096
										<b>69,576</b>
2011 - 2021	PASTURE	0.076	0.076	<b>0.076</b>	<b>0.076</b>	<b>0.031</b>	0.076	0.076	0.076	6,881
2011 - 2021	ROAD	0.083	0.083	<b>0.083</b>	<b>0.083</b>	<b>0.044</b>	0.083	0.083	0.083	12,253
2011 - 2021	SCRUB	0.055	0.166	<b>0.140</b>	<b>0.140</b>	<b>0.083</b>	0.061	0.056	0.145	12,936
2011 - 2021	TREES	-0.059	0.166	<b>0.057</b>	<b>0.114</b>	<b>0.086</b>	0.054	-0.036	0.144	24,398
										<b>56,468</b>
2011 - 2022	PASTURE	0.061	0.083	<b>0.074</b>	<b>0.074</b>	<b>0.031</b>	0.072	0.063	0.081	16,291
2011 - 2022	ROAD	0.058	0.058	<b>0.058</b>	<b>0.058</b>	<b>0.043</b>	0.058	0.058	0.058	12,253
2011 - 2022	SCRUB	0.029	0.141	<b>0.115</b>	<b>0.115</b>	<b>0.093</b>	0.032	0.03	0.119	12,936
2011 - 2022	TREES	-0.108	0.076	<b>-0.021</b>	<b>0.089</b>	<b>0.106</b>	-0.073	-0.101	0.046	28,096
										<b>69,576</b>
2019 - 2021	PASTURE	-0.006	0.149	<b>0.066</b>	<b>0.067</b>	<b>0.025</b>	0.026	0	0.105	50,362
2019 - 2021	ROAD	0.053	0.08	<b>0.074</b>	<b>0.074</b>	<b>0.031</b>	0.075	0.057	0.079	13,016
2019 - 2021	SCRUB	-0.029	0.254	<b>-0.010</b>	<b>0.027</b>	<b>0.061</b>	-0.018	-0.029	0.15	14,371
2019 - 2021	TREES	-0.03	0.072	<b>0.033</b>	<b>0.051</b>	<b>0.083</b>	0.049	-0.014	0.067	41,729
										<b>119,478</b>
2019 - 2022	PASTURE	-0.227	0.133	<b>-0.016</b>	<b>0.086</b>	<b>0.048</b>	0.012	-0.138	0.07	96,334
2019 - 2022	ROAD	0.041	0.08	<b>0.053</b>	<b>0.053</b>	<b>0.031</b>	0.056	0.046	0.074	15,157
2019 - 2022	SCRUB	-0.052	0.078	<b>-0.040</b>	<b>0.045</b>	<b>0.070</b>	-0.043	-0.049	0.032	14,371
2019 - 2022	TREES	-0.078	0.032	<b>-0.014</b>	<b>0.039</b>	<b>0.105</b>	-0.015	-0.06	0.019	45,427
										<b>171,289</b>
2021 - 2022	PASTURE	-0.016	0.04	<b>0.000</b>	<b>0.017</b>	<b>0.015</b>	-0.005	-0.015	0.027	50,362
2021 - 2022	ROAD	-0.025	0.003	<b>-0.023</b>	<b>0.024</b>	<b>0.017</b>	0	-0.02	0.002	13,016
2021 - 2022	SCRUB	-0.176	-0.014	<b>-0.030</b>	<b>0.030</b>	<b>0.061</b>	-0.026	-0.118	-0.018	14,371
2021 - 2022	TREES	-0.091	-0.018	<b>-0.048</b>	<b>0.048</b>	<b>0.051</b>	-0.048	-0.082	-0.024	41,729
										<b>119,478</b>